RF MEMS CAPACITIVE SWITCHES FOR TUNABLE MICROSYSTEMS

Thesis

Submitted in partial fulfillment of the requirements for the degree of
DOCTOR OF PHILOSOPHY

by
Shajahan E. S.
Under the Guidance of
Dr. M. S. Bhat
Professor

DEPARTMENT OF ELECTRONICS AND COMMUNICATION ENGINEERING,
NATIONAL INSTITUTE OF TECHNOLOGY KARNATAKA,
SURATHKAL, MANGALORE - 575025

October, 2019

DECLARATION

I hereby ***declare*** that the Research Thesis entitled **RF MEMS CAPACITIVE SWITCHES FOR TUNABLE MICROSYSTEMS** which is being submitted to the ***National Institute of Technology Karnataka, Surathkal*** in partial fulfillment of the requirement for the award of the Degree of ***Doctor of Philosophy*** in **Department of Electronics and Communication Engineering** is a ***bonafide report of the research work carried out by me***. The material contained in this Research Thesis has not been submitted to any University or Institution for the award of any degree.

SHAJAHAN E. S.
Reg. No. EC10F01
Department of Electronics and Communication Engineering.

Place: NITK-Surathkal.
Date:

CERTIFICATE

This is to certify that the Research Thesis entitled **RF MEMS CAPACITIVE SWITCHES FOR TUNABLE MICROSYSTEMS** submitted by **SHAJAHAN E. S.** (Register Number: EC10F01) as the record of the research work carried out by him, is accepted as the *Research Thesis submission* in partial fulfillment of the requirements for the award of degree of **Doctor of Philosophy**.

Prof. M.S.Bhat
Research Supervisor
Professor
Dept. of Electronics and Communication Engg.
NITK, Surathkal

Chairman-DRPC
(Signature with Date and Seal)

Faith,
Its all about *Believing,*
YOU DON'T KNOW, HOW IT WILL HAPPEN. BUT YOU KNOW IT WILL

Dedicated to my wife Shiji
and sons, Neeraj and Saarang

Acknowledgements

Though mere words cannot, it is my pleasure to place on record my deep sense of sincere thanks and gratitude to my research supervisor Dr. M S Bhat, Professor, Department Electronics and Communication Engineering, NITK, Surathkal. His dedication, keen interest and above all constant support in times of crisis is the main reason for the completion of my research work. His timely directions and meticulous documentation helped me in the submission of thesis at the appropriate time. I would like to express my sincere thanks and appreciation to my RPAC members, Dr. T. Laxminidhi, Professor and Head, Department of E&C Engineering, Prof. Ananthanarayana V S, Professor, Department of IT, NITK, Surathkal and Prof M N Sathyanarayana, Professor, Department of Physics, NITK surathkal, Dr. Muralidhar Kulkarni, former Professor and Head of E&C Engineering, for their valuable comments and support. I express sincere thanks to Bharat Electronics Limited (BEL), Bangalore and Society for Integrated Technology and Applied Research (SITAR), Bangalore for fabricating our designs. I also thank Centre for Nano science and Engineering (CeNSE), IIsc. Bangalore for supporting us in the characterization of the fabricated devices. I owe a deep sense of gratitude to Dr. Sumam David, the then Professor and Head for giving me an opportunity to undergo research work in this department. I would like to thank former PG student of the department Mr. Chenna Reddy B and fellow research scholar Mr. Raghavendra for their help and support. I also thank the non teaching staffs of E&C Department, Mrs Pushpalatha, Mr. Sanjeev Poojary, Mr. Subramanya Karanth, Mrs Prabha, Mrs. Soumya, Mr Tilak and Mr Ratish. Last but not least, I must express my profound gratitude to my wife, Shiji, and sons Neeraj and Saarang, for their unfailing support throughout my years of study.

Abstract

This thesis deals with the design, simulation, fabrication and characterization of low voltage Radio Frequency Micro-electro-mechanical Systems (RF MEMS) capacitive shunt switches. Switch membrane geometry is modified to achieve low actuation voltage in the range of $10 - 18.5\,V$ and good RF performance in different bands. Commercial CAD tool CoventorWare is used for design and DC analysis while RF analysis is carried out using ANSYS HFSS and Agilent ADS.

Inductive tuning of switch membranes is employed to tune the RF characteristics to optimize X, Ku, K and Ka band performance. Inductance is added to the shunt membranes by modifying beam geometry. The fabrication of the switches is carried out as a five mask surface micromachining process on silicon substrate. DC and RF parameters are measured and are found to be very good. Further, the design, electromechanical and electromagnetic modeling of Single Pole Four Throw switch is carried-out as part of the thesis. The DC and RF simulation results show low actuation voltage of 13.75 V, insertion loss and isolation better than 0.7 dB and 52 dB respectively in X-band.

Additionally, wide-band and narrow-band tunable bandpass filters in X and Ku bands are designed on co-planar waveguides using cantilever series and capacitive shunt switches and realized as cascaded sections of highpass and lowpass filters. Tunability in center frequency from 11.76 GHz to 15.86 GHz is achieved by the controlled actuation of shunt switches and bandwidth tunability from 2.34 GHz to 5.4 GHz by series switches.

Further, distributed true time delay phase shifter is designed on slow wave co-planar waveguide employing five sets of metallic membranes as floating shield. The controlled actuation of the floating membranes result in variable capacitive loading and thereby achieving good phase tunability. The design provided a phase shift tunability in the range 18° to 28° at 10 GHz, 124° to 180° at 70 GHz and a liniar variation in the above range for the intermediate frequencies.

Keywords: RF MEMS, Series Switch, Shunt Switch, SP4T Switch, Inductive Tuning, Tunable Bandpass Filter, Phase Shifter.

Contents

List of Figures

List of Tables

ABBREVIATIONS

BST	Barrium Strontium Titanate
CPW	Co-Planar Waveguide
DMTL	Distributed MEMS Transmission Line
FET	Field Effect Transistor
HFSS	High Frequency Structure Simulation
IC	Integrated Circuit
LIGA	Lithographie, Galvanoformung, Abformung
MEMS	Micro Electro Mechanical System
MIM	Metal-Insulator-Metal
RF	Radio Frequency
RLC	Resistor Inductor Capacitor
S-CPW	Slow-wave Co-Planar Waveguide
SP4T	Single Pole Four Throw
SPDT	Single Pole Double Throw
SPDT	Single Pole Double Throw
SPMT	Single Pole Multi Throw
SPST	Single Pole Single Throw
TEM	Transverse Electro-Magnetic
TTD	True Time Delay
T-line	Transmission Line
YIG	Yttrium Iron Garnet

Chapter 1

INTRODUCTION

1.1 MEMS Technology

Micro Electro Mechanical Systems (MEMS) can be defined in a general form as the integration of miniaturized mechanical elements, microsensors and microactuators and are made employing microfabrication techniques. MEMS is an emerging interdisciplinary technology, which utilizes expertise from different fields including IC fabrication technology, material science, mechanical engineering, chemical engineering, biomedical engineering and others. In the last couple of decades, MEMS technology has spread to different application areas, such as telecommunication (filters, phase shifters), healthcare (blood pressure sensors), military, automotive (pressure sensors, micro accelerometers), consumer electronics (thermal, pressure and humidity sensors, gyroscopes, digital micro-mirror devices for projectors) and aerospace industries (accelerometers, gyroscopes). MEMS devices are small in dimensions, in the range of few micrometers to millimeters, and combine both electrical and mechanical components on the same substrate (Rebeiz (2004)). This enables them to perform various complex functions in different domains like electrical, mechanical, thermal, fluidic, magnetic and optics. The main advantages of MEMS technology are that the devices have small size, low cost, ultra low power consumption, superior performance and precision. As the technology is still booming, there is further scope for improvement in development of the devices with the implication that MEMS can only become more attractive.

MEMS technology was initiated in 1970's and most successful developments happened in this area with the emergence of accelerometers, gyroscopes, switches, pressure sensors, ink-jet print heads, to name a few. MEMS structures normally contain movable mechanical structures like membranes, beams and cantilevers which are fabricated using silicon micromachining techniques. In this technique mechanical and structural layers are fabricated using both surface micromachining and bulk micromachining techniques.The surface micromachining fabrication is done through different thin film deposition techniques whereas bulk micromachining mainly uses etching techniques. Sacrificial layers are used to create hanging or suspended structures.

1.2 RF MEMS Technology

MEMS devices working at the microwave frequencies are called Radio Frequency (RF) MEMS devices. The advent of RF MEMS technology has improved the high frequency devices' characteristics. RF MEMS devices are actuated by different mechanisms such as electrostatic, magnetostatic, thermal and piezoelectric. Among these mechanisms, electrostatic actuation is widely used because of low power consumption, simplicity and compactness.

The RF MEMS devices can be classified into three categories. The first class is RF extrinsic devices in which the device is placed outside the RF circuit but it controls the devices within the circuit (ex: RF transmission lines). The second one is RF intrinsic devices, where device is placed inside the circuit and performs decoupled RF functionalities and actuation (ex: RF MEMS switches and capacitors). The RF reactive devices are the third type which perform coupled actuation and RF functionalities (ex: RF resonators).

One of the promising application fields of MEMS technology is in RF signal switching. Switches are essential components in a variety of high frequency applications such as mobile phones, wireless local networks, radars and satellites. Some major advantages of RF MEMS switches over solid-state device technology are low insertion loss, high isolation, low power consumption and high linearity. The main disadvantages of this technology include low switching speed in the range of few μs and upwards, low power handling capability and, stiction, which is adhesion of microstructure to its neighboring surface. MEMS switch is first demonstrated by Peterson in 1979, (Petersen (1979)), using a cantilever formed using bulk micromachining technique. Initially, these switches were used for low frequency applications. The first MEMS switch fabricated for RF applications was reported in 1990 by Larson at the Hughes Research Lab in Malibu, California under the support of Defense Advanced Research

Projects Agency (DARPA) (Rebeiz (2004)). RF MEMS switches are now widely used in telecommunication systems.

1.2.1 MEMS Fabrication Techniques

The main material used in MEMS fabrication is silicon because of its mechanical stability, high melting point, semiconductivity and its abundance in nature. Some metals and their alloys, ceramics and polymers are also used for MEMS fabrication. Bulk micromachining and surface micromachining are the two major MEMS fabrication techniques.

Bulk micromachining technique comprises of selective removal of the substrate to form device layers through etching. It can be classified as wet or dry etching depending on the phase of etchants used. In dry etching, vapor etchants are used and in wet etching, etchants will be in liquid form. Isotropic etching is used to etch uniformly in all direction. In anisotropic etching, etchants will etch in different directions at different rates. Wet etching, in most case, is done from the backside while dry etching is done from the front side.

In surface micromachining, deposition and etching of structural and sacrificial thin layers are incorporated. The sacrificial layer is etched out to create a void. The devices made by surface micromachining techniques are smaller in size and have high compatibility with CMOS devices than that made with bulk micromachining techniques.

1.3 RF MEMS Switch

Switches are the most common and important components in all electronic circuits. Basic functionality of a switch is to either short circuit or open circuit a signal line. The main uses of RF or microwave switches are in signal routing and impedance matching. There are different kinds of switches available in market for RF applications. Solid state devices such as PIN diode, MOSFET, and GaAS (Gallium-Arsenide) FET (Field Effect Transistor) are commonly used as switches in RF circuits. However, the RF characteristics of these switches are not good enough above a few GHz. Coaxial and waveguide switches offer the benefits of very low insertion loss, high isolation and high linearity in high frequency applications (> 1 GHz). However, they are bulky, heavy, very sluggish and need high actuation voltages. On the other hand, RF MEMS switches offer high isolation and low insertion loss compared to the solid state switches. Low power consumption, negligible current and high levels of integration are other advantages of MEMS switches (Rebeiz (2004)). MEMS switch is essentially a passive device and it may be used to build low loss and low power digital phase shifters, re-configurable filters, impedance matching networks and switching networks. Various designs of MEMS series and shunt switches (generally referred to as ohmic and capacitive contact, respectively) made out of nickel (Pacheco *et al.* (2000)), aluminum (Balaraman *et al.* (2002)), gold (Chan *et al.* (2003)), and copper (Balaraman *et al.* (2002)) have been reported in literature with a variety of applications. MEMS switches can be easily integrated with coplanar waveguides, slotline and microstrips by means of surface micromachining fabrication process (Varadan *et al.* (2003)). In many cases, a single MEMS component can replace and outperform an entire solid-state circuit. E.g., Low loss, high isolation and with negligible dc power consumption RF MEMS switches can eliminate the need for an amplifier stage in Tx/Rx modules and thus result in considerable power saving and size reduction. In RF MEMS switches the switching action is achieved by the displacement of a beam or cantilever. However, presence of moving structure makes the MEMS switch fabrication more complex.

1.4 Comparison Between RF MEMS and Semiconductor Switches

Despite high voltage requirements of RF MEMS switches compared to solid-state switches (PIN and FET), they offer high isolation, lower power consumption and higher frequency of operation. The degradation of switching time over solid-state devices is often traded for better insertion loss. Table 1.1) shows the relative parameter values of the MEMS and solid-state switches.

1.4.1 Series and Shunt RF MEMS switches

Depending on the switch type (series or shunt), the MEMS switches can show very good RF performance from DC to several tens of Giga Hertz. However this performance of the RF MEMS switches comes with some trade-offs as well compared to their solid-state counterparts. These include dielectric charging (Peng *et al.* (2007)), high

Table 1.1: Comparison of RF MEMS and semiconductor switches (Rebeiz (2004)).

Parameters	RF MEMS	PIN	FET
Voltage (V)	5-80	± 3-5	3-5
Current (mA)	≈ 0	3-20	0
Power consumption (mW)	0.05-0.1	5-100	0.05-.1
Switching time	1-300 μs	1-100 ns	1-100 ns
Cup (fF)	1-6	40-80	70-140
Capacitance ratio	40-500	10	N/A
Cut-off frequency (THz)	20-80	1-4	0.5-2
Isolation (1-10 GHz)	Very High	High	Medium
Isolation (60-100 GHz)	High	Medium	N/A
Insertion Loss (1-100 GHz) (dB)	0.05-0.5	0.3-1.2	0.4-2.5
Power Handling (W)	< 1	< 10	< 10

pull-down voltage and slow switching speed. The pull-down voltage is very decisive for commercial portable device applications. Several methods have been used to improve the specification of RF MEMS switches with primary focus on lowering actuation or pull-down voltage. There exists great challenges to lower the actuation voltage and having a robust and reliable operation. Some of the common methods used to lower the actuation voltage are, modifications of membrane geometry, choice of membrane material, varying gap height, and also using electromagnetic and thermal actuation (Mao *et al.* (2010)). Although currently there is tremendous amount of research in RF MEMS devices, reliability and packaging of the switches continue to be problematic. The switches are limited in their power handling capability as well.

In series switches (membrane is in series with the transmission line), two metal electrodes are brought into contact to create a low-resistance connection. Generally, a cantilever beam structure is used in these switches. In capacitive switches (membrane is in shunt with the transmission line), a metal membrane is pulled down onto a dielectric layer, usually by electrostatic means, to form a capacitive sandwich. At high frequencies, this capacitive sandwich acts like a shunt capacitor with a 100:1 capacitance ratio (actuated:unactuated). The deformation of the metal membrane causes the switch to efficiently change from a high impedance to a low impedance.

In metal to metal contact switches depicted in figure 1.1a, ohmic contact is made by pulling down the metal beam using a DC voltage. In this type, the up-state position induces high impedance and hence it acts as an open circuit. When the beam is pulled down, the impedance decreases and results in a short circuit.

In capacitive switches depicted in figure 1.1b, a metal-insulator-metal contact is established. In this configuration, a shunt membrane is placed in shunt with the transmission line. When the switch is in off-state, the transmission line is undisturbed and the RF signal passes through the switch. Insertion loss is zero for an ideal shunt switch in off-state. Whereas in the on-state, the transmission line is capacitively coupled to the ground and the signal is bypassed to the ground. The ratio of down-state capacitance to up-state capacitance ($C_r = C_{off}/C_{on}$) is a very important parameter that determines the RF performance. These switches are being used in many high frequency (5-100 GHz) applications such as phase shifters, tunable filters and reconfigurable antennas (Rebeiz (2004)).

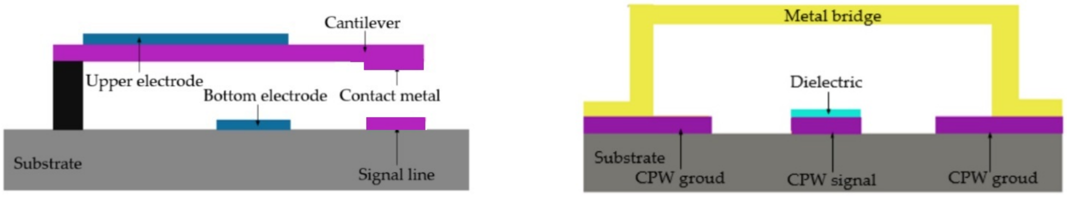

(a)

(b)

Figure 1.1: Schematics of typical MEMS switches: (a) Cantilever type series switch; (b) Bridge type shunt switch. (CPW = coplanar waveguide).

1.5 RF MEMS Switching Mechanisms

In RF MEMS switches, the on-off mechanism is based on the movement of beams or cantilevers. MEMS switches are micro scaled mechanical devices with two stable states. The device allows the propagation of an RF signal from the input to the output in one state and blocks the signal in the other state. Switching between the states is achieved through the mechanical movement of a hanging structure essentially a cantilever or bridge anchored at the one or both ends respectively. The movement can be induced through different types of actuation mechanisms, e.g., electrostatic, piezoelectric, thermal or magnetic.

Most switches reported in the literature use electrostatic actuation due to its advantages such as low power consumption, thin layers of material, small electrode size, low switching time and very large C_{off}/C_{on} capacitance ratio. Table 1.2 shows various actuation methods along with the with relative switch parameters.

Table 1.2: Comparison of types of actuations of RF MEMS switches (Rebeiz (2004)).

Actuation type	Piezo electric	Electro thermal	Electro magnetic	Electro static
Size	Medium	Medium	Large	Small
Process complexity	High	Medium	High	Low
Actuation voltage (V)	3-20	3-5	3-5	5-80
Power consumption	0-100	0-200	0-100	0
Switching time (μs)	50-1000	300-10000	300-1000	1-200
Reliability	Medium	Low	Medium	High

1.6 RF MEMS Switch Specifications

MEMS switches are characterized by their DC, transient, and frequency responses. Some of the major parameters used for characterization are listed below.

1.6.1 Pull-in Voltage

Pull-in voltage (actuation voltage) is one of the important parameters of an electrostaticaly operated RF MEMS switch. Switching action in these type of switches is due to the mechanical movement of the beams under an applied voltage. Pull-in voltage is the voltage at which the electrostatic force becomes greater than the restoring force of the beam, resulting in the beam position becoming unstable. This makes the beam to bend downwards, resulting in the closing of the switch (switch-on in series switch) or shunting the signal line to the ground (switch-off in a shunt switch). The pull-in voltage of MEMS switches is normally high compared to that of semiconductor switches.

1.6.2 Isolation

Isolation, expressed in dB, is defined as the ratio of the output signal power to the input signal power when the switch is OFF (or unactuated) in case of a series switch, and ON (or actuated) in case of a shunt switch. Isolation is the magnitude of a signal that gets coupled across an open circuit. RF MEMS switches typically offer better isolation at high frequencies unlike semiconductor switches.

1.6.3 Insertion Loss

Insertion loss, expressed in dB, is the loss of signal power when the signal passes through the switch. It describes the efficiency of the switch in signal transmission. Insertion loss is represented as the ratio of input RF signal to output signal in the ON state of the switch. Insertion loss must be as minimum as possible.

1.6.4 Return Loss

Return loss is a measure of voltage standing wave ratio (VSWR), expressed in dB. Return loss is the loss of power in the signal returned/reflected by a discontinuity in a transmission line. Main reason for this is impedance mismatch between the switch and the signal line. At high frequencies, the material properties as well as the dimensions of the switch and the signal line determine the impedance mismatch. Return loss must be as minimum as possible.

1.6.5 Operating Frequency Range

Operating frequency range of a switch is the range of frequencies over which the switch has acceptable limits of maximum insertion loss and minimum isolation values. It is also known as the operating bandwidth of RF MEMS switch. The lower bound of the frequency (f_L) is limited by the minimum isolation, whereas upper bound (f_U) is limited either by maximum insertion loss or minimum isolation.

1.6.6 Switching Speed

Switching time of RF MEMS switch is the time the switch takes to move from the off-state to on-state or vice versa. It depends on the pull-in time and release time. The switching time is high (in the order of a few μS) for MEMS switches compared to solid-state switches.

Pull-in Time: It is defined as the time taken by the movable part of the switch (cantilever or bridge) to make contact with the underlying plate when the applied voltage is above the pull-in voltage.

Release Time: The time taken by a movable structure such as cantilever beam or metal bridge (acceleration limited system) to regain its original position when the applied voltage is zero.

1.7 Motivation and Objectives

A switch being the most basic and essential component of any communication system and RF MEMS switches have the potential to replace solid state and waveguide switches because of their advantages, this research focuses on the design, fabrication, characterization of RF MEMS shunt switches and its applications in different RF frequency bands.

It is a known fact that the design and development of efficient RF MEMS switches for integrating with the current day silicon MOS technology is a challenge due to their high actuation voltage. Further, the RF response of the switches needs to be tuned to get improved performance compared to their solid-state counterparts. Thus achieving low actuation voltage and tuning for specific frequency bands is one of the major objectives of this thesis. Since shunt switches have a wider bandwidth, provide improved characteristics at higher frequencies and amenable to finer tuning compared to series switches, this work focuses on the design, fabrication and characterization of low voltage tunable shunt switches. In case of multi port switches, performance optimization is more complex and challenging, and very few researchers have attempted this. Thus, the investigation of the design of single pole multi-throw switches will add new knowledge to the RF MEMS field with applications requiring band switching. With this in the background, the following research objectives are drawn.

- Design, fabricate and characterize low voltage (< 20 V), low loss (< 1 dB) RF MEMS shunt switches with low switching delay ($< 10\ \mu s$) and high isolation ($>$ 20 dB) in X, Ku, K and Ka frequency bands.

- Design inductively tuned switches to provide improved isolation.

- Design low voltage SP4T switches for X-band applications.

- Design reconfigurable bandpass filter with MEMS switches as varactors for X-band applications.

- Design a slow-wave distributed true-time-delay tunable phase shifter using RF MEMS switches for X-band applications.

1.8 Structure of the thesis

This thesis is divided into seven chapters.

Chapter 1 presents an introduction and overview of RF MEMS technology and RF MEMS switches, followed by the objectives and motivation for this work.

Chapter 2 gives a brief overview of the mechanical and electromagnetic models of RF MEMS switches followed by a review of recent literature and background of RF MEMS switches.

Chapter 3 presents the design, fabrication and characterization details of RF MEMS shunt switches. It also presents inductive tuning of the switches for improved isolation in select frequency bands.

Chapter 4 presents the design and simulation results of a low loss single pole four throw switch.

Chapter 5 presents the use of shunt switches as varactors in the design of reconfigurable bandpass filters in X-band.

Chapter 6 presents the design and simulation of slow-wave distributed true-time-delay tunable RF MEMS phase shifter.

Chapter 7 concludes the work by highlighting the contribution made and discusses scope for future work.

In this research work several recent technologies for enhancing the DC and RF characteristics of RF MEMS switches have been reviewed. The main focus of this work is to optimize the switch dimensions to reduce the actuation voltage and enhance the RF characteristics of the RF MEMS electrostatically actuated shunt switch. FEM based Commercial CAD software CoventorWare is used for design while DC and RF analyses are carried out by ANSYS HFSS and Agilent ADS.

The switches are fabricated at two foundries, viz., Society for Integrated Circuit Technology and Applied Research (SITAR) Bangalore and Bharat Electronics Limited (BEL) Bangalore. DC and RF characterization of the switches is done at the Centre for Nano Science and Engineering (CeNSE) Laboratory at Indian Institute of Science (IISc), Bangalore.

Chapter 2

DESIGN AND MODELING OF RF MEMS SWITCHES

2.1 Design Aspects of RF MEMS Switches

There are two aspects in the design of an RF MEMS Switch, namely, electro-mechanical design and electro-magnetic design. In this work, electro-mechanical design and simulation are done using CoventorWare software while electro-magnetic design (RF characteristics) and simulation are done using ANSYS HFSS software. Under electro-mechanical design, spring constant, pull-in voltage and dynamic response (switching time) are studied. In electro-magnetic design, RF behavior of the switch is analyzed with the help of S-parameters.

2.2 Electro-mechanical Design

This section deals with the electro-mechanical design of electrostatically actuated MEMS switches. RF MEMS switch beams are fixed either at one end (series switch) or at both the ends (shunt switch) as shown in figure 2.1. The electrostatic actuation is used to deflect the structure in the direction perpendicular to the beam plane. Pull-in voltage and dynamic response are the two parameters which decide the suitability of the switches for any given application.

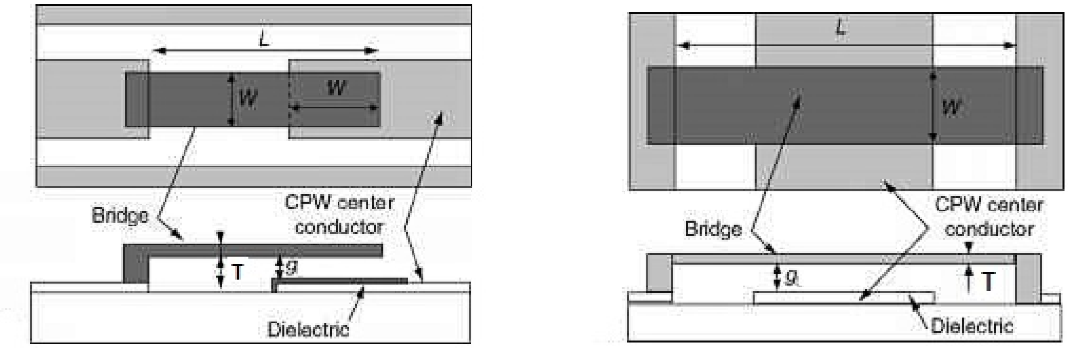

(a)

(b)

Figure 2.1: MEMS switch schematic with dimensions (a) series (b) shunt

2.2.1 Electrostatic Actuation and Pull-in Voltage

In electrostatic actuation, movement of the beam is produced by the electrostatic force which exists between the beam and the ground plane, like the one existing between the two plates of a parallel plate capacitor. The equivalent capacitance is a function of the overlap capacitance and the fringe field capacitance. To model electrostatic actuation and to determine the actuation voltage of a MEMS switch, generally the parallel plate capacitance model is used (Rebeiz (2004)).

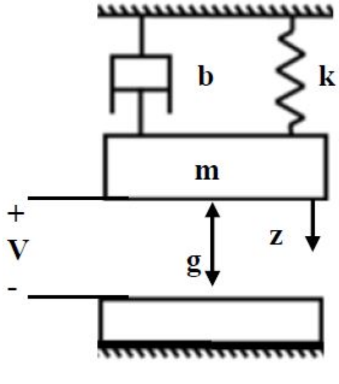

Figure 2.2: Schematic of the electro-mechanical equivalent of MEMS switch: mass-spring parallel-plate capacitor.

The capacitance of a parallel plate capacitor is given by the relation,

$$C = \frac{A\varepsilon_0}{g} \tag{2.1}$$

With the change in the gap, capacitance is given by,

$$C = \frac{A\varepsilon_0}{(g - z)} \tag{2.2}$$

where z is the reduction in the separation between the two parallel plates. With the application of electrostatic force, the energy stored in the parallel plate capacitor is given by,

$$E = 0.5CV^2 = 0.5\frac{A\varepsilon_0}{(g - z)}V^2 \tag{2.3}$$

The electrostatic force between the plates can be determined by differentiating the energy function with respect to the direction of the force.

$$F = \frac{dE}{dz} = 0.5\frac{A\varepsilon_0}{(g - z)^2}V^2 \tag{2.4}$$

If the moving parallel plate is attached to a spring, having spring constant k, then under equilibrium condition

$$kz = \frac{dE}{dz} = 0.5\frac{A\varepsilon_0}{(g - z)^2}V^2 \tag{2.5}$$

$$V = \sqrt{\frac{2kz(g - z)^2}{\varepsilon_0 A}} \tag{2.6}$$

If the electrostatic force is increased by increasing the applied voltage, the charge in the plates increases and the beam height (gap between the beams) decreases. This in turn increases the capacitance and thus the electric field. At an applied voltage known as the pull-in voltage, the increase in the electrostatic force is greater than that of the restoring force due to the spring action of the beam, the beam collapses to the down-state position. By taking the derivative of (2.6) with respect to the beam height and set it as zero, the height at which the collapse occurs is found to be exactly two-thirds of the zero-bias beam height. Substituting these values back into (2.6), the "pull-in" voltage is given by,

$$V_p = \sqrt{\frac{8kg^3}{27\varepsilon_0 A}} \tag{2.7}$$

where,

k = Spring constant of beam.

g = Air gap between the beam bottom edge and dielectric top.
A = Area of intersection.
ε_0 = Permittivity of free space.

From (2.7) it can be seen that the actuation voltage can be decreased in three different ways: first, by decreasing the height of the beam, second, by increasing the contact area of the bridge and third, by selecting the shape of a bridge with low spring constant. Each of these have their own pros and cons. In the mechanical design, most important parameter to consider is the spring constant k of the structure. The beam is modeled as cantilever with two guided ends. The spring constant for a guided end cantilever is given by the equation (Rebeiz (2004)),

$$k = \frac{EwT^3}{L^3} \tag{2.8}$$

where L, w and T are the length, width and thickness of the bridge, and E is the Young's modulus of the membrane material.

For a shunt (fixed-fixed) membrane, the spring constant, k is given by

$$k = \frac{32\ EwT^3}{L^3} + \frac{8\ \sigma\ (\ 1 - \nu\ )Tw}{L} \tag{2.9}$$

where ν is the Poisson's ratio of the membrane material and σ is the residual stress (in MPa) in the membrane.

2.2.2 Effect of Residual Stress on Pull-in Voltage

Thin film structures undergo deformation due to the build-up of residual stress during fabrication (Fang and Wickert (1996)). The stress in thin films can be categorized into two types, namely, extrinsic and intrinsic. The extrinsic stress arises due to the mismatch in thermal expansion coefficients, whereas the intrinsic stress is due to the nucleation and the growth of film deposition. In the first order approximation, the general uniaxial residual stress in a thin film is given by the equation

$$\sigma_{Total} = \sigma_0 + \sigma_1 \left(\frac{z}{T/2} \right) \tag{2.10}$$

where z is the coordinate across the thickness (t) with origin chosen at the film's mid plane, σ_1 is the gradient stress, σ_0 is the mean stress and σ_{Total} is the superposition of gradient and mean stress.

When a beam or a cantilever is released by the removal of the sacrificial layer, the hanging structure becomes free to move out-of-plane in the form of bending down or up. But after the release, gradient stress remains intact in the thin film. The mean stress also causes the deformation in the form of rotation or tilt of the structure. These stresses cause problems in the beam structures. These deformations due to gradient and mean stress need to be minimized for robust performance. From literature, mean stress is found to vary between 0 MPa to 150 MPa, whereas stress gradient is in the order of 40 MPa/μm (Fang and Wickert (1996)) for electroplated gold. The bending and tilt of the beam structure affects the pull-in voltage of the switch. Pull-in voltage increase with increase in gradient stress.

2.2.3 Pull-in Time and Release Time

Switching speed of MEMS switches depend on pull-in time and release time of the switch. Pull-in time is defined as the time taken by the movable structure to make contact with the underlying plate. Release time is the time taken by a movable structure (acceleration limited system) to regain its original position. Switching time can be modeled using the force balance equations involving mass, spring and damper equivalent model of parallel plate capacitor given in (2.11).

$$m\frac{d^2z}{dt^2} + b\frac{dz}{dt} + kz = \frac{0.5\varepsilon_0 AV^2}{(g-z)^2} \tag{2.11}$$

where m is the mass of the movable plate, A is the area of the plates, g is the gap between the plates, V is the applied voltage and b is the damping coefficient, given by,

$$b = \frac{3}{2\pi}\frac{\mu}{g^3}A^2 \tag{2.12}$$

A closed form expression for the pull-in time can be obtained for the acceleration limited system (b = 0) by assuming the electrostatic force to be constant and equal to the initial applied value. Under the above approximations, the equation of motion becomes:

$$m\frac{d^2z}{dt^2} + kz = \frac{0.5\varepsilon_0 AV^2}{(g-z)^2} \tag{2.13}$$

The closed form solution for the switching time (pull-in time) of an acceleration limited system (with low damping coefficient, $b \approx 0$, and a quality factor $Q > 2$ of the resonant beam) is given by (Rebeiz (2004)),

$$Pull - in\ time,\ t_p \approx \frac{3.67 V_p}{\omega_0 V} \tag{2.14}$$

where ω_0 is the mechanical angular resonant frequency of the movable structure, V_p is the pull-in voltage and V $(> \ V_p)$ is the applied voltage.

When the switch is in the actuated position, if the applied voltage is made zero, the movable structure (cantilever beam / metal bridge) returns to its original position. The time taken by the movable structure to regain its original position under zero damping is given by (Shekhar *et al.* (2011)),

$$Release\ Time,\ t_r = \frac{1}{4\sqrt{k/m}} \tag{2.15}$$

where m is the effective mass and k is the spring constant of the beam.

2.3 Electro-magnetic Design

This section deals with the electro-magnetic modeling of the MEMS switches. The electro-magnetic model of RF MEMS switch is used to accurately determine the electrical parameters (resistance, inductance and capacitance of MEMS switch) from S-parameter measurements. Different beam and anchoring structures exhibit different RF characteristics and it is possible to tune the switches to operate in any given RF band by modifying the switch geometry.

2.3.1 Lumped Electrical Model of Series and Shunt Switch

2.3.2 In-line Series switch

Figure 2.3a shows the lumped circuit model of the inline series (metal to metal / resistive contact) switch of figure 2.1a in the OFF and ON states. In the electrical model, MEMS series switch is a series capacitance C_s in the up state (OFF) and a small resistance R_s in the down state (ON). Here, cantilever beam is represented by a transmission line with characteristic impedance Z_h and electrical length βl. Characteristic impedance of the CPW lines at the two ports is represented by Z_0. Capacitive coupling between the two CPW lines introduces C_p. Thus, in series with Z_h, there is a resistance R_s in ON state or a capacitance C_s in OFF state due to the contact resistance and coupling capacitance respectively. Further there is a parallel capacitance C_p which is the signal line coupling capacitance in both the states due to the gap between the broken signal lines. The contact resistance R_s is mainly affected by surface roughness of contact area as well as contact force. If the contact surface is smooth and applied force is large, then R_s will be relatively small.

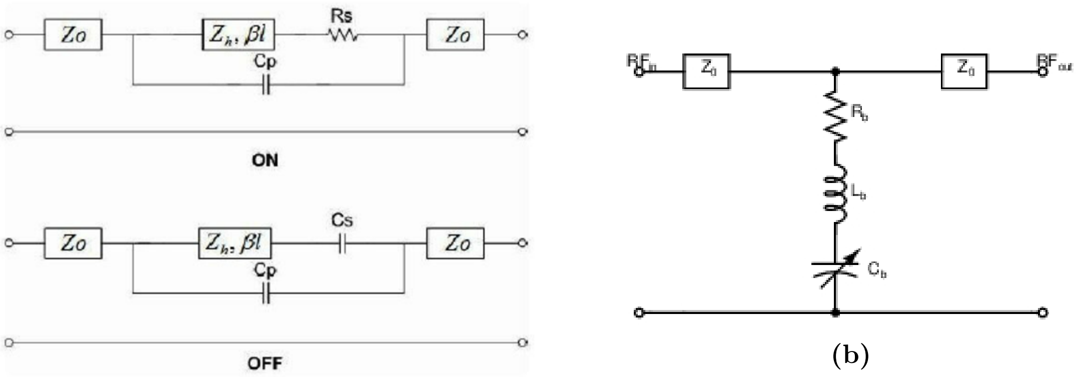

(a)

(b)

Figure 2.3: Lumped circuit model of (a) series switch in ON and OFF state (b) shunt switch

2.3.3 Capacitive coupled shunt switch

Figure 2.3b shows the equivalent electrical model of the capacitive coupled shunt switch shown in figure 2.1b. The RF capacitive switch can be modeled by a transmission line with characteristic impedance Z_0 and a lumped shunt CLR branch for the beam. R_b, L_b and C_b represents the resistance, inductance and capacitance of the shunt metallic beam. The variable bridge capacitance C_b changes according to the actuation state of the switch. When the beam is unactuated C_b is of the order of a few tens of femto Farads. On actuation of the beam, C_b increases to a few pico Farads. The impedance of the bridge, Z_b, as seen by the centre conductor of the CPW line, is therefore given by,

$$Z_b = R_b + j(\omega L_b - \frac{1}{\omega C_b}) \tag{2.16}$$

where $C_b = C_u$ or C_d depending on the actuation state of the RF capacitive switch. C_u is the up state capacitance and C_d is the down-state capacitance. The up state capacitance C_u is given by,

$$C_u = \frac{A\varepsilon_0}{g + \dfrac{t}{\varepsilon_r}} + \ C_f \tag{2.17}$$

where A is the overlap area, g is the air gap height, t is the dielectric thickness, ε_0 is the free space permittivity, ε_r is the relative permittivity of the dielectric material and C_f represents the fringing field capacitance.

The down state capacitance, C_d is given by,

$$C_d = \frac{\epsilon_0 \epsilon_r A}{t} \tag{2.18}$$

With proper switch geometry and material selection, the ratio C_d/C_u can be made larger for efficient switching at microwave frequencies. The total impedance Z_b of the switch will change with frequency because the impedance of each reactive component changes with frequency. When $\omega L_b = 1/\omega C_b$, the LC series circuit resonates. The resonant frequency, f_0, is given by,

$$f_0 = \frac{1}{2\pi\sqrt{L_b C_b}} \tag{2.19}$$

and the impedance of the bridge can be approximated by,

$$Z_b = \begin{cases} \dfrac{1}{j\omega C_b} & \text{for} \quad f \ll f_0 \\ R_s & \text{for} \quad f = f_0 \\ j\omega L_b & \text{for} \quad f \gg f_0 \end{cases} \tag{2.20}$$

The RLC model behaves as a capacitor below the LC series resonant frequency and as an inductor above this frequency. At resonance, RLC model reduces to the series resonance of the MEMS bridge. Inductance of the bridge plays absolutely no role in the up state, but plays an important role in the down state. A common measure of performance of electronic switches is the cut off frequency, the theoretical frequency where the ratio of OFF-impedance to ON-impedance degrades to unity. This frequency is given by,

$$f_c = \frac{1}{2\pi R_b C_u} \tag{2.21}$$

where R_b is the effective down state beam resistance, and C_u effective up state capacitance of the switch. The cut off frequency does not represent a frequency where the switch is operated, but merely a theoretical basis for comparison. While this figure-of-merit has been extensively used with with p-i-n diodes, it is not appropriate for MEMS switches. The reason is that the switch inductance limits the down state performance at a much lower frequency than f_c. A better value to use as f_c is $2f_0$ (given in (2.19)) since MEMS shunt switch results in acceptable isolation up to twice the resonant frequency in the down state.

Table 2.1: Comparison of Microwave Switch Device Performance

Device Type	R_b(ohms)	C_u(fF)	FOM- Cutoff Freq(GHz)
GaAs MESFET	2.3	249	280
GaAs p-i-n	4.7	80	420
RF MEMS Capacitive	0.4	35	> 9000

The bandwidth of a switch is specified considering the isolation performance. The isolation of the switch is limited by the down state capacitance for frequencies lower than the LC resonant frequency f_0, and by the bridge inductance for frequencies higher than the resonant frequency. Thus, in order to achieve high isolation, the bridge capacitance or bridge inductance should be increased. However the bridge capacitance is limited due to reasons such as area miniaturization considerations, surface roughness and fabrication difficulties of suspended structures with large areas. The bridge inductance can be increased by properly modifying the geometry, which is referred as inductive tuning (Muldavin and Rebeiz (2000*b*)).

2.3.4 RF characteristics

The RF performance of the switch is quantified by its insertion loss, return loss and isolation. It is desirable to have low insertion loss and high isolation. In order to improve the RF performance, it is necessary to modify the beam geometry. When the switch is unactuated, up state capacitance, C_u, will be very small, in the order of few hundreds of femto farads, and bridge inductance and resistance can be neglected. Therefore, neglecting L_bR_b, theoretical Return Loss, S_{11} in the up state is given by (Rebeiz (2004)),

$$S_{11} = \frac{-j\omega C_u Z_0}{2 + j\omega C_u Z_0} \tag{2.22}$$

and Insertion Loss, S_{21} in the up state can be expressed as,

$$S_{21}|_{f \ll f_0} = 20log\left|\frac{2}{2 + j\omega C_u Z_0}\right| \tag{2.23}$$

Insertion loss includes substrate loss, conductor loss due to skin effect and reflection due to impedance mismatch. To minimize substrate leakage loss, use of high resistivity silicon is a solution. By depositing a thin layer ($\sim 1\ \mu m$) of low dielectric constant (such as SiO_2) over the substrate, the dielectric will act as a buffer isolating the flow of leakage current between the CPW signal and ground conductors. However, when single crystal silicon is used as the substrate material of RF MEMS switches, the resistivity of silicon has an effect on the RF characteristics of the switches. The total loss tangent, tan δ_t, of a lossy dielectric medium is given by

$$tan\ \delta_t = tan\ \delta_l + tan\ \delta_d \tag{2.24}$$

where tan δ_l is the intrinsic loss resulting from the polarization loss of the intrinsic silicon substrate and tan δ_d is the extrinsic loss resulting from the finite conductivity of silicon substrate. Therefore, total loss is increased as conductivity of the silicon substrate is increased.

Isolation of the switch is determined by down state capacitance C_d and inductance L_b of the beam. Since C_d is dependent on the surface roughness, it cannot be easily modeled. Thus it is important to measure the S-parameter around the resonant frequency. At resonance, the transmission line is loaded with bridge resistance R_b alone and the isolation of switch S_{21} in down state, is given by (Rebeiz (2004)),

$$S_{21}|_{f=f_0} \approx 20log\frac{2R_b}{Z_0 + 2R_b} \tag{2.25}$$

Thus the series resonance is very beneficial in determining the isolation performance of the shunt switch. However this high isolation can be achieved only around the LC resonant frequency of the switch. When $f \gg f_0$, the isolation is expressed as,

$$S_{21}|_{f \gg f_0} = 20log\left|\frac{2j\omega L_b}{Z_0 + 2j\omega L_b}\right| \tag{2.26}$$

Hence the electrical parameters of the bridge can be extracted using the above equations from the simulated S-parameters.

2.4 Literature Review on RF MEMS Switches

RF MEMS switches are used mainly in applications requiring high RF performance. Various approaches have been discussed in the literature to optimize the performance, such as lower pull-in voltage, improved isolation etc. based on the requirements. Following section presents a brief overview of different kinds of switches used in the literature.

2.4.1 MEMS Switch with Low Actuation Voltage

Pull-in voltage is the most important parameter in electro-mechanical design of the switch. As can be seen from (2.7), factors that affect pull-in voltage are, spring constant, beam height and contact area. This section presents a brief literature review of low actuation voltage switches.

2.4.2 Improvements in micromechanical aspect

2.4.2.1 Actuation voltage

The use of low spring constant designs like meandering springs to achieve lower actuation voltage (Pacheco *et al.* (2000)) has been a standard practice. But such designs often compromises with the reliability of the device and the switching speed. Feasibility of low height bridges is also been investigated (Muldavin and Rebeiz (2001)) to lower actuation voltage but the price paid is a reduction in capacitance ratio and hence the RF performance. Also, use of new materials like Aluminium silicon alloy($AlSi_{0.04}$) or platinum as membrane (Ekkels *et al.* (2009)) has been reported. Al$Si_{0.04}$ membrane has a higher spring constant for the same dimensions but the transmission loss is two times more than gold. Multiple actuation mechanism in the same switch has also been explored (Cho *et al.* (2005)) but this has a very complicated fabrication procedure.

In 1998, Peroulis *et al.* (2003) published an electrostatically actuated switch with a pull-in voltage of 14-16 V. To reduce the spring constant, meander structures are used at the either end of the bridge. A 2 μm thick, electroplated gold membrane was embedded between bottom and top electrodes of the switch. Once the switch is pulled down, the capacitive coupling increases and the center conductor provides a virtual short to ground plane. Aluminum was used as CPW material, and 50 nm of parylene was coated on the metal structure for isolation and anti stiction purpose. The RF performance of the switch was found to be good (ON-state: S_{21}= - 0.2 dB at 20 GHz, OFF-state: $S_{21} < -40\ dB$ for frequencies up to 40 GHz).

In 2003, a novel low spring constant switch was developed by (Pacheco *et al.* (1998)). In this switch, the inductance of the signal path in the down-state is determined by the special geometry of the beams supporting the membrane, providing improved isolation because of resonance behavior in the target frequency range. Around 80% reduction in the actuation voltage was obtained by increasing the number of meanders from 1 to 5 in folded configuration. The theoretical spring constant and actuation voltage of the switch for 5 meanders reported are 1.1 N/m and 6 V respectively. The actuation voltage was different from the designed value due to the intrinsic axial stress resulted in the nickel armature during fabrication.

Efforts were also made to reduce the mechanical spring constant with the use of different materials. MEMS switch with Al and $Al_{0.96}Si_{.0.04}$ alloy (Guo *et al.* (2003)) were used as the armature material for reducing the actuation voltage. The switch structure is optimized by calculating pull-in voltages which depends on geometrical sizes, membrane materials and Youngś modulus of the material. Experimental results showed that this alloy has a reduced pull-in voltage of 5 V compared to the gold beam which had an actuation voltage of 45V. But, the transmission loss of the alloy beam was twice in comparison to the gold beam. In 2006, (Dai and Chen (2006)) used Al as bridge material and the switch had a pull-in voltage of 7 V, but with poor RF response (isolation and insertion loss of the switch were 15 dB and 3.1 dB at 40 GHz). The study showed an improvement in the pull-in voltage at the expense of the RF performance.

2.4.2.2 Switching speed

Achieving a high switching speed remains a major limitation and little work has been done to improve the speed of RF MEMS switches except what was proposed by Mercier *et al.* (2005) by the miniaturization of the switches. Mercier *et al.* (2004) demonstrated microsecond switching times using dielectric membrane switches. Lacroix *et al.* (2007) proposed miniaturized modified beams that enhances the spring constant causing a further increase in mechanical resonance frequency leading to sub microsecond switching time. But any increase in stiffness of the membrane enhances actuation voltage requirement. Some research groups demonstrated the possibility of actuation voltage reduction without complex mechanical spring (Hafez *et al.* (2005)). In order to demonstrate the spring-less RF switch concept, a scaled up RF MEMS switch design in the range of millimeters coupled with relatively large electrostatic actuation gaps was realized (Shekhar *et al.* (2011)).

2.4.2.3 Dielectric layer

The contact area between metal bridge and dielectric surface governs the up-state and down-state capacitance of the device (Yu *et al.* (2006)). The charging process occurring in the dielectric layer is the limiting factor for the reliability of capacitive RF MEMS switches and models have also been reported to predict the same (Spengen *et al.* (2004)). Modeling of dielectric charging has been demonstrated for better understanding (Sumant *et al.* (2007)). Many high-k materials have been suggested as potential replacements for Si_3N_4 as dielectric material. These include Al_2O_3, Lead zirconate titanate (PZT), Hafnium oxide (HfO_2), Strontium titanate oxide ($SrTiO_3$), Barium strontium titanate (BST), Tantalum pentoxide ($\mathrm{Ta_2O_5}$) etc. Dielectric constants of different materials are shown in table 2.2.

Table 2.2: High-k dielectric materials

Material	Dielectric Constant
Silicon Oxide (SiO_2)	3.9
Silicon Nitrate (Si_3N_4)	7.5
Strontium Titanate Oxide ($SrTiO_3$)	30-120
Hafnium Oxide (HfO_2)	17
Barium Strontium Titanate (BST)	72-201
Tantalum Pentoxide (Ta_2O_5)	27.9

High-*k* dielectrics are good candidate materials for capacitive MEMS switches. However, there have not been many experimental studies related to the reliability issues of these materials when used in MEMS devices. The key characteristics for selecting an alternative dielectric are (a) dielectric constant, (b) dielectric strength, (c) resistivity, (d) leakage current, (e) surface roughness and (f) charge trapping density. Many dielectrics appear favorable in some of these areas but very few materials satisfy all these requirements. $Ba_{0.5}Sr_{0.5}TiO_3$ is the most commonly investigated material, since it has the highest dielectric constant at room temperature. By adjusting the Ba/Sr ratio and other film growth parameters, precise control can be exercised over the dielectric constant. The dielectric constant of BST thin film is much smaller than bulk BST. The dielectric constant of the BST films grown by aerosol deposition method were 100, 201, and 72 in $Ba_xSr_{1-x}TiO_3$ at x = 1.0, 0.6, and 0.4, respectively. Further probing is required to find a material that can replace Si_3N_4 as dielectric as process integration compatibility is a major issue (Persano *et al.* (2012)).

2.4.2.4 Power handling capability

Power handling capability is limited by (a) Joule heating due to high power which may result in melting of contacts and (b) Self biasing and RF latching. Jensen *et al.* (2003) reported models to predict the power handling capability of the RF MEMS switches.

2.4.2.5 RF performance

Analysis indicates that CMOS grade low resistivity silicon substrate is not suitable for high frequency applications due to attenuation of RF signals. For high resistivity substrates, a frequency of 10 GHz is large enough to drive the silicon substrate into its dissipative dielectric mode. Thus the role of substrates and the use of suitable passivation play an important role in the RF performance of the device (Cusmai *et al.* (2005)). Authors have also reported that with passivation layers of the order of tens of micron thickness on the low resistivity silicon substrate, the insertion loss could be reduced to acceptable levels. Although there are many advantages in using high-k dielectrics such as large breakdown voltage, low defect density, resistance to dielectric charging, low deposition temperature, the ability to generate patterns, and low surface roughness at the interface etc., many high-k dielectric materials are thermodynamically unstable on silicon.

2.4.3 MEMS Switch with High Isolation and Low Insertion Loss

High isolation is one of the major desirable properties of RF MEMS switch. A High Isolation Series Shunt RF MEMS Switch is reported by (Yu *et al.* (2009)). To achieve high isolation, they use a combination of series and shunt switches. When series switch is closed and shunt switch is open, the composite switch is in ON condition, whereas when the series is off and shunt switch is on, the composite switch is in OFF condition. The shunt switch helps to improve isolation of the switch in off condition. The paper reported an outstanding isolation of more than 40dB and a low insertion loss of 0.35 dB from DC to 12 GHz.

Goldsmith *et al.* (1998) developed a low loss, low-cost RF MEMS capacitive shunt switch which employs electrostatic actuation for actuating the beam. In this work the authors use a shorter transmission line which helps in the reduction of insertion loss and the switch area. Further, high isolation was obtained by removing the imperfections in the design of the switch membrane.

The first MEMS switch was demonstrated by Petersen (1979) using bulk micromachined cantilever. Since then, variety of MEMS switches have been designed and developed with different dimensions, parameters and materials to achieve better performance characteristics. The first MEMS switch for microwave applications was developed by Larson *et al.* (1991) at the Hughes Research Labs. However, this switch had poor yield and reliability. Yet, it showed excellent RF performance upto 50 GHz. In 1995, Raytheoneveloped the first practical capacitive shunt switch. The bridge structure is composed of 0.3 μm thick aluminum bridge suspended 4 μm over the transmission line. Si_3N_4 with a thickness of 100 nm was used as a dielectric layer. At 10 GHz, it is reported that the isolation and insertion loss of the switch are approximately 0.5 dB and 15 dB respectively. An improved version of the MEMS switch is reported by Goldsmith *et al.* (1998) and Yao *et al.* (1999) with an reduced insertion loss of 0.14 dB and enhanced isolation of 24 dB at a frequency of 20 GHz, having an actuation voltage in the range 35 V - 50 V and a switching time of 5 μs. An interesting design variation was introduced in 2001 by Robert Bosch GmbH, Germany. The membrane of their longitudinal capacitive shunt switch is part of the signal line and, when lowered by applying approximately 25 V, it capacitively short circuited to ground. The design is optimized for 24 GHz (S_{21} (ON) $>$ -0.3 dB, S_{21} (OFF) $<$ -33 dB) (Ulm *et al.* (2001)).

Muldavin and Rebeiz (2000*b*) reports the design and an electromagnetic model of tuned two and four bridge cross switch from 10 to 40GHz. A pull down voltage of 15-25V is measured. An insertion loss of less than 0.3–0.6 dB, a return loss below 20 dB from 22 to 38 GHz in the up state, and a down-state isolation of 45 to 50 dB is attained for the cross switch. Also, an X-band switch with an insertion loss of less than 0.2 dB and an isolation of 35 dB is reported. This is achieved by performing the inductive tuning of switch. Muldavin and Rebeiz (2001) reports the developments in RF MEMS switches and high isolation switch circuits. It provides an overall picture on MEMS series and capacitive shunt switches. The reliability of MEMS switches for long term applications and packaging issues are also discussed.

Peroulis *et al.* (2003) reports the design, fabrication, and testing of a low-actuation voltage MEMS switch for high-frequency applications. Although it has a very low actuation voltage of 6 V, its response time is relatively high ($> 50\ \mu S$). Dussopt and Rebeiz (2003) reports a theoretical and experimental study of the nonlinear effects in RF MEMS varactors and capacitive switches. MEMS capacitive components generate very low intermodulation products compared to semiconductor devices. The noise generated due to thermal effects on the beam is also modeled. Simion (2003) reports a general formula for the spring constant by considering real distribution of electrostatic force along the MEMS bridge. A numerical analysis of a switch consisting of an array of MEMS switches is also presented. It was studied that a large width of CPW central line makes a faster switch but operating frequency decreases due to increased switch capacitance. Milosavljevic (2004) reports an overview on MEMS technology, applications and RF MEMS switches. A technique for modeling and design of inductively-tuned MEMS shunt switch is done in this work.

Sharma *et al.* (2007) reports the effect of various geometric dimensional parameters of switch on electromagnetic and mechanical behaviour of a shunt capacitive MEMS switch with simulations using ANSYS HFSS software. Demirel *et al.* (2016) reports the design and fabrication of a new RF MEMS switch structure at Ka band to achieve minimum permanent deformation of bridge structure for a thermal treatment upto $270°C$. The actuation voltages are found to be 22V and 25V before and after the thermal treatment. Shekhar *et al.* (2017) reports the fabrication and dynamic characterization of a low-actuation-voltage capacitive RF MEMS switches with improved electromechanical performance. The switching time is found to be 33-37 μs. An insertion loss less than 0.7 dB and isolation better than 30 dB is reported.

Chapter 3

HIGH ISOLATION RF MEMS SHUNT SWITCHES FOR X, Ku, K AND Ka BANDS

3.1 Introduction

It has been reported extensively that series resistive switches have a limited RF range from 1 to 10 GHz and prone to stiction. Goldsmith *et al.* (1998), Yao *et al.* (1999) and Peng *et al.* (2007) have reported that shunt capacitive switches have better performance at higher frequencies than series switches. Thus, shunt capacitive switches have been considered in this study keeping in view of wide frequency range of operation, reliability and better RF characteristics. For tuning the shunt switches to meet the desired RF performance in the frequency band of interest, inductive tuning concept was proposed by Muldavin and Rebeiz (2000*b*). However, such tuning improves frequency selectivity but increases the fabrication complexity.

The current work is divided into three parts. First, a set of shunt switches are designed for low actuation voltage and high isolation in the X, Ku, K and Ka bands. These designs are simulated, fabricated and characterized. At the simulation stage, parametric analysis of the switches for different physical parameters is carried out to assess the RF and DC performance. Further, inductive tuning is used to achieve improved RF response in the X, Ku, K and Ka bands. Characterization of the fabricated switches is done to ascertain the correctness of the design. A few switches are then packaged for use in the reconfigurable antenna applications.

3.2 Performance Analysis

In this section, the parametric analysis of the reference design of a shunt switch is discussed. For this analysis, one of the shunt switches is considered among the set of switches designed for fabrication in a coplanar waveguide (CPW) configuration. The geometrical parameters of the switch are listed in table 3.1. These parameters are chosen considering mechanical and electrostatic constraints and the ease of fabrication. The CPW transmission line dimensions used are G/W/G = 60/100/60 (μm). These dimensions correspond to a characteristic impedance (Z_0) of 50 Ω. A CPW line consists of a center conductor with semi-infinite ground planes on either side. Principal advantage of CPW at millimeter wave frequencies is that the signal ground as well as signal line are on the on the same plane. This simplifies the fabrication process and allows easy integration of shunt and series circuit elements. The substrate used is high resistivity silicon (4000 Ω-cm) of 500 μm thick and relative dielectric constant of 11.7. The beam length (L) shunting the transmission line, beam width (w), beam thickness (T) and the air gap between the beam and transmission line (g) are shown in figure 3.1a and 3.1b. A control voltage actuates the membrane for switching action. During unactuated state, the RF signal travels down the transmission line unaffected from input port to output port in the OFF state of the shunt switch. The typical parameters used in this work are shown in table 3.1. These parameters are chosen taking into account the ease of fabrication along with mechanical and electrostatic constraints. When a control voltage is applied between the beam and the transmission line, the electrostatic field forces the membrane to deform downwards. The elastic force due to the membrane stiffness balances the electrostatic force until the threshold

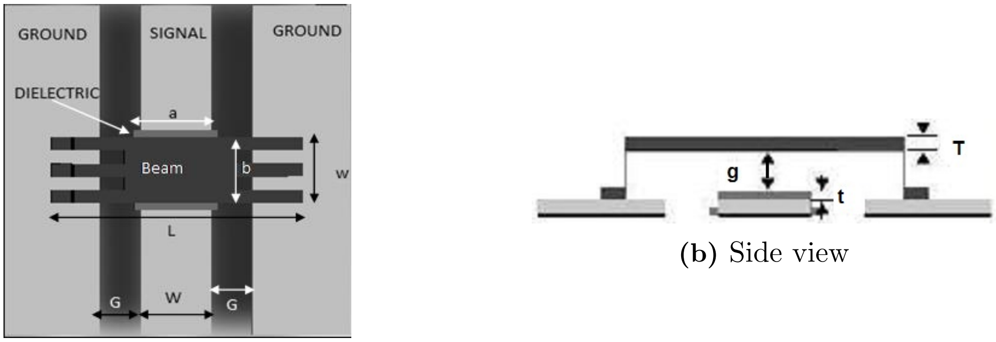

(a) Top view.

(b) Side view

Figure 3.1: RF MEMS Shunt Switch

voltage (also called actuation voltage or pull-in voltage) is reached. When the control voltage exceeds the threshold voltage, the field overcomes the elastic force and pulls the membrane down on to the transmission line, presenting an RF short. This is ON state. On removal of control voltage, the elastic force brings the membrane back to the original position.

Table 3.1: Geometrical Parameters of RF MEMS Capacitive Shunt Switches

Parameter	Dimension in μm
Si Substrate Dimension ($\epsilon_r = 11.7$)	1200*1000*500
CPW configuration (G/W/G)	60/100/60
Length of the membrane (L)	300
Width of the membrane (w)	100
Thickness of the membrane (T)	1
Gap between electrode and membrane (g)	3
Dimension of the Dielectric (Si_3N_4, $\epsilon_r = 7.4$) above the electrode	120*120*0.1
Width of the each anchor leg	20

For a given beam geometry, material properties like Young's modulus and Poisson's ratio determines the stiffness constant and thus pull-in voltage. Also, from the S-parameter perspective, the beam material should have high conductivity. So material having lower Young's modulus and high conductivity is preferred as membrane. With miniaturization, there is quest for thin film structures for enhanced performance and thus there arises the need for reliable assessment of stress build up. Depending on the nature of stress build up in the membrane, pull-in voltage may increase or decrease. In this work airgap (g) beneath the released membrane is measured and variations from designed values are observed. It is known that pull in varies directly as $g^{3/2}$. Compressive stress in the fabricated film may cause slight reduction in airgap. Compressive stress reduces membrane stiffness as well. Both the effects results in reduction of pull-in voltage. In our experiments, it is observed that the pull-in voltage varies at the rate of around 1 volt for airgap variation of 0.1 m. Pull-in voltage variation is due to the cumulative effect of airgap variation, membrane stiffness and stress build up in the membrane. By the measurement of membrane geometry, airgap (both by profilometry) and pull-in voltage, a reliable assessment of nature of stress can be arrived at. Table 3.2 lists the properties of commonly used materials.

Table 3.2: Membrane material properties Birleanu *et al.* (2016)

Material	Young's Modulus (E) (Giga Pascal)	Poisson's Ratio	Conductivity (Siemens/meter)
Gold (Au)	78	0.44	$4.5 * 10^7$
Aluminum(Al)	70	0.345	$3.8 * 10^7$
Copper (Cu)	110	0.355	$5.8 * 10^7$

For MEMS switches to become appropriate for hand-held communication systems, low actuation voltage is desired. In order to lower the pull-in voltage of the switch, the possible alternatives (as seen from (2.7)) and the associated drawbacks, are,

1. Increasing the area of actuation: Since miniaturization is the prevailing issue, increasing the size is not generally recommended.
2. Reducing the gap between transmission line and membrane: Reduced beam height is associated with stiction problems due to close proximity and related reliability issues.
3. Reducing the spring constant: This is the most desirable option for low pull-in voltage. This generally will not impact size or RF performance, but suffers from low switching speed. The disadvantages like low switching speed (2-10 μs) and high actuation voltages (20-40 V) may be tolerated in application such as low-loss high isolation telecommunication switches and radars with low scanning rates.

3.2.1 DC Analysis

Design and detailed DC analysis of RF MEMS switches with respect to beam geometry is carried out in FEM based commercial software CoventorWare. Following subsections lists the results.

3.2.1.1 Pull-in Voltage Analysis

Figure 3.2a shows displacement Vs Voltage plot for Al, Au, Cu and Pt as membrane materials. The plot illustrates the dependence of pull-in voltage on the membrane material properties. Young's modulus and Poisson's ratio are two important mechanical properties of thin film materials and are significant design parameters for micro electrical mechanical systems (MEMS). Spread in membrane displacement with applied field for various materials can be considered as displacement spread for material parameters. Displacement depends on membrane stiffness which for the same geometry varies with Young's modulus and Poisson's ratio. It has been observed from simulation that, for the same beam geometry, switch with aluminum membrane has the lowest pull-in since aluminum has the lowest Young's modulus (70x10^9 N/m^2). The flipside is that high conductivity metals such as gold and aluminum have low melting point and thus low thermal stability resulting in plastic deformation of the membranes at relatively low temperature ($< 200^0 C$). High melting point metals such as platinum show plastic deformation only at high temperatures which makes them attractive for use as membrane material in RF MEM switches (Ekkels *et al.* (2009)). The mechanical properties of thin films are dependent on the microstructure of the films, which is determined by the specific deposition conditions, such as the heat cycle of the chamber. It is difficult to evaluate the mechanical properties of thin films using simulation methods based on the film deposition conditions. It is challenging to obtain accurate mechanical properties of thin films due to technical difficulties (for example, Young's modulus of gold varies with temperature, membrane thickness and geometry). Visual Image tracing methods can be used for the real time measurement of strain up to a resolution of 50 nm. Figures 3.2b - 3.2e shows the impact of beam geometry on pull-in voltage. As shown by (2.9) beam length exhibits strong inverse relation where as beam thickness shows strong direct relation. Pull-in voltage (V_p) is directly proportional to $g^{\frac{3}{2}}$ and is shown figure 3.2e.

3.2.2 S-Parameter Analysis

RF analysis of the switch with respect to variations in beam dimensions is carried out using High Frequency Simulation Software (ANSYS HFSS). Figures 3.3a - 3.3c shows the insertion loss variations with respect to beam geometry. Lower beam width and higher dielectric thickness implies lower insertion loss. This is due to lowered up state capacitance, C_u, as per (2.17). In the case of fabricated switches, at very high frequencies, beyond 30 GHz, where skin depth is smaller than the conductor surface roughness, current follows through contours of the surface of the conductor, effectively increasing the distance over which current must flow and hence the resistance of the conductor. In such instances, increase in insertion loss is observed at high frequencies. At low frequencies, conductor loss due to surface roughness variations is insignificant.

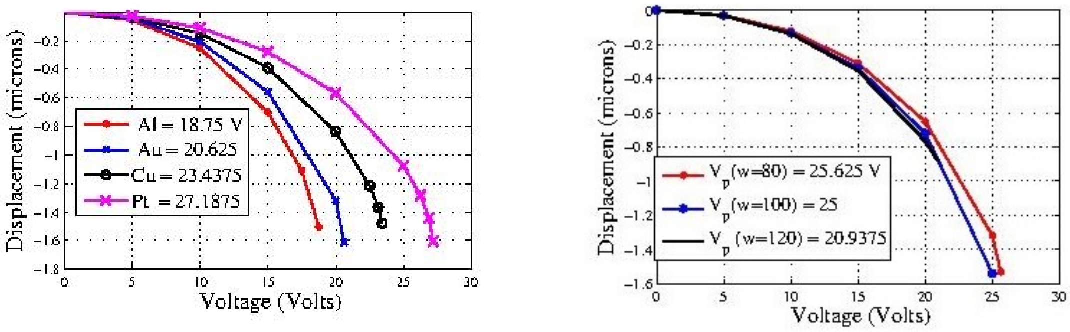

(a) Pull-in voltage for various materials

(b) Pull-in voltage for varying beam widths

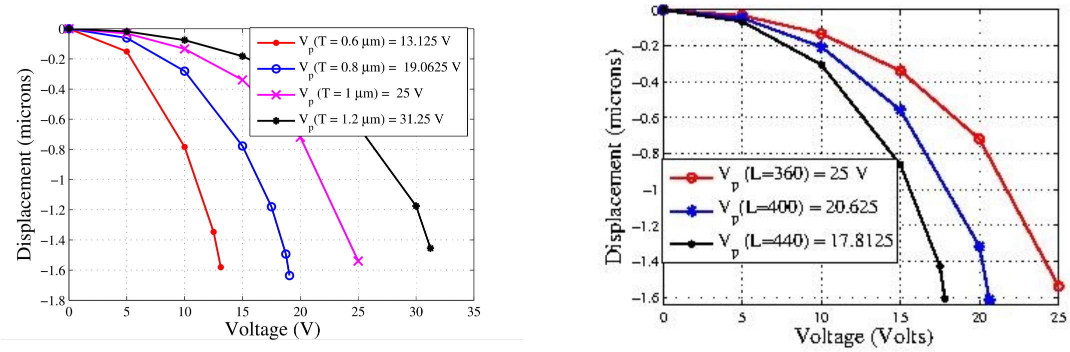

(c) Pull-in for varying beam thickness

(d) Pull-in for varying beam lengths

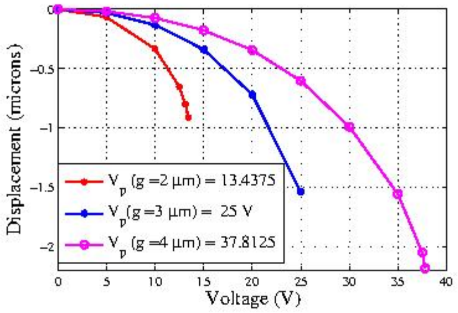

(e) Pull-in voltage for varying airgap

Figure 3.2: Pull-in voltage versus Beam Geometry

Up state or OFF state Return Loss (S_{11}) characteristics is seen to be better with reduced beam width. At 20 GHz, S_{11} is -20 dB for a beam width of 60 μm where as it is -16 dB with a beam width of 120 μm. Other beam dimensions do not seem to have big impact on the characteristics. This is shown in figures 3.4a - 3.4c. As already stated, isolation in a shunt configuration is determined primarily by the down state capacitance C_d. With increase in beam width, C_d increases and beam resistance

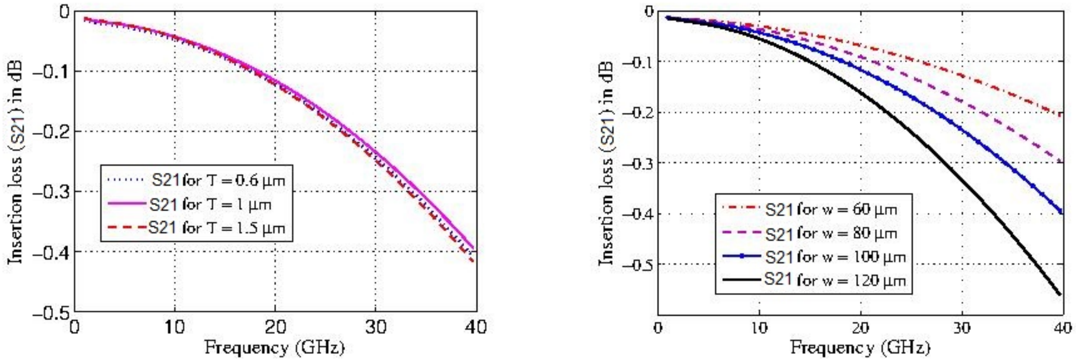

(a) Insertion loss Vs beam thickness **(b)** Insertion loss Vs beam width

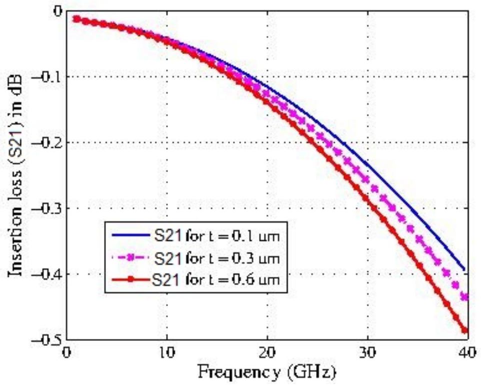

(c) Insertion loss Vs dielectric thickness

Figure 3.3: Insertion Loss (IL) Vs Beam Geometry

decreases. As shown in figure 3.5a, the isolation curve becomes steeper and deeper with increase in beam width. As dielectric thickness t increases, C_d decreases, isolation characteristic becomes worse. The frequency at which resonance occurs also gets shifted. This is shown in figure 3.5b. Figure 3.5c indicates that beam thickness has hardly any impact on isolation. Down state reflection characteristics is not influenced by the beam geometry. Figure 3.6 shows that the down state Return loss is almost 0 dB beyond 10 GHz implying total reflection in down state (ON) position of beam.

3.2.3 Extraction of model parameters R, L, C from simulated S-Parameters

The series inductance L and bridge resistance R are evaluated using the curve fitting techniques on the simulated (ANSYS HFSS) S-parameters. The series resistance of the bridge can be best extracted from S_{21} at the LC resonant frequency, since the shunt

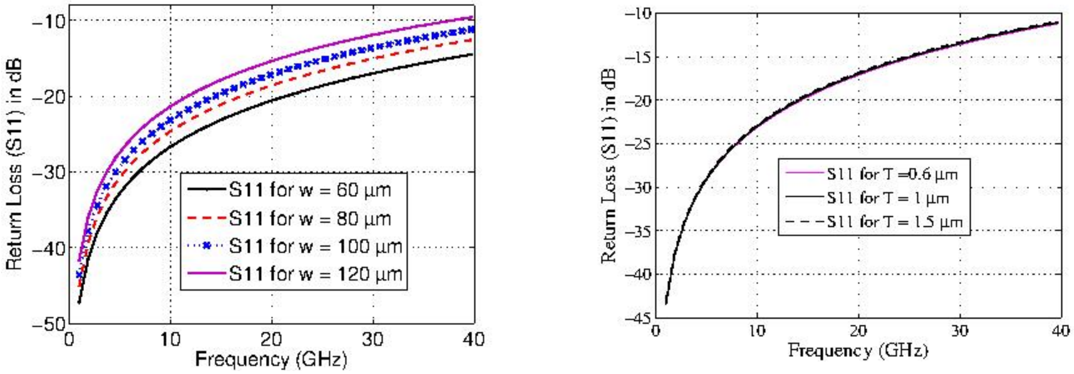

(a) Up state Return Loss Vs beam width **(b)** Up state Return Loss Vs beam thickness

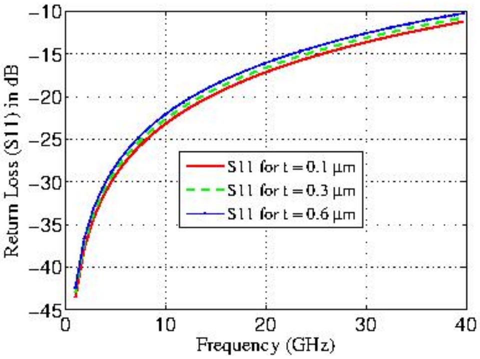

(c) Up state Return Loss Vs dielectric thickness

Figure 3.4: Up state Return Loss (S_{11}) Vs Beam Geometry

branch (in figure 2.3b) reduces to a simple resistance at resonance in the downstate. The bridge inductance models the voltage induced on the bridge due to the current flowing to the ground planes. The inductance is determined by the portion of the beam over the separation of the signal and ground lines of the CPW since the fields are concentrated at the separations, and there is a canceling effect for the portions of the bridge over the CPW center conductor and ground planes (Muldavin and Rebeiz (2000*a*)).

Equation (2.24) indicates that substrate resistivity depends on the polarization loss (tan δ_l) of the intrinsic silicon substrate and the extrinsic loss (tan δ_d) resulting from the finite conductivity of silicon substrate. Therefore, total loss is increased as conductivity of the silicon substrate is increased. It can be seen from the simulation results from figure 3.8 that substrate resistivity influences S-parameters (S_{11} and S_{12}) in up state, while they remain unaffected in the down state.

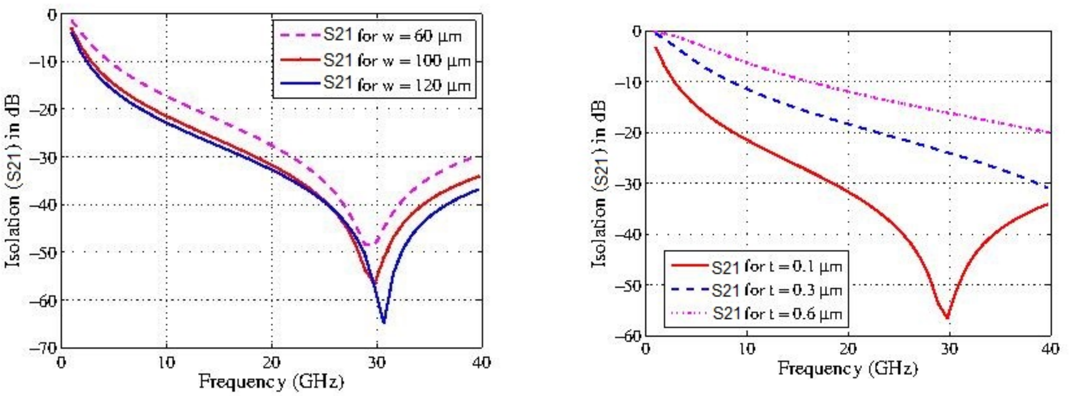

(a) Isolation Vs beam width

(b) Isolation Vs dielectric thickness

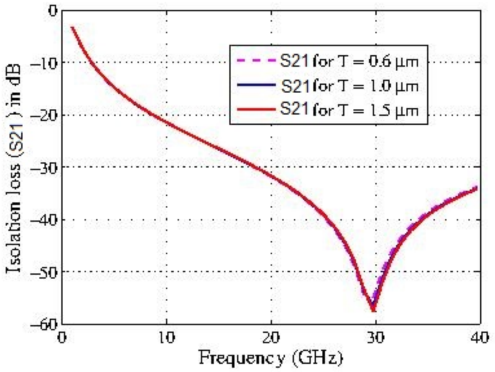

(c) Isolation Vs beam thickness

Figure 3.5: Isolation Vs Beam Geometry

3.3 Inductive Tuning

As reported in Muldavin and Rebeiz (2000*b*) and Topalli *et al.* (2009), RF performance of shunt switches can be improved either by inductively or capacitively tuning the switches. For a switch with series resonance frequency f_0 given by (2.19), the slope of the isolation characteristics is determined by capacitance for f $< f_0$, and by beam inductance for f $> f_0$. Simulations show that increase in capacitance results in the isolation characteristics to go steeper and deeper and vice versa. Further, the capacitance is dependent on the surface roughness of the fabricated switch. Since switch miniaturization is one of the prevailing requirements in system integration, increasing switch capacitance is not recommended.

In this work, the beam inductance of the MEMs switch is increased by creating notches in the CPW ground plane. The RF electric field between the central conduct-

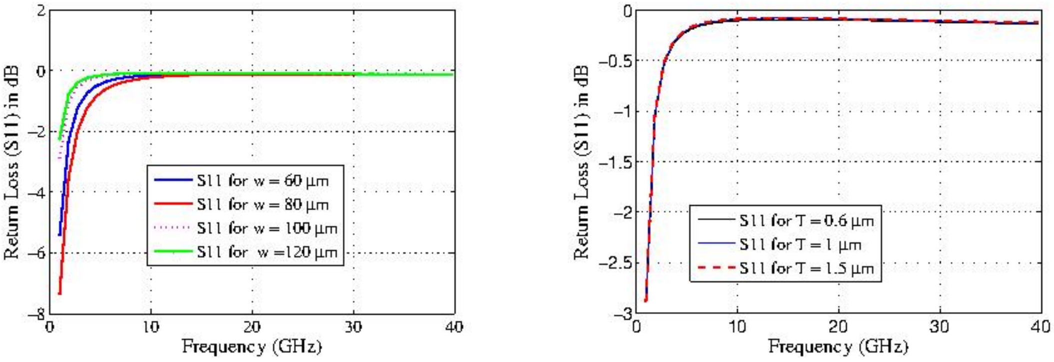

(a) Return Loss Vs beam width **(b)** Return Loss Vs beam thickness

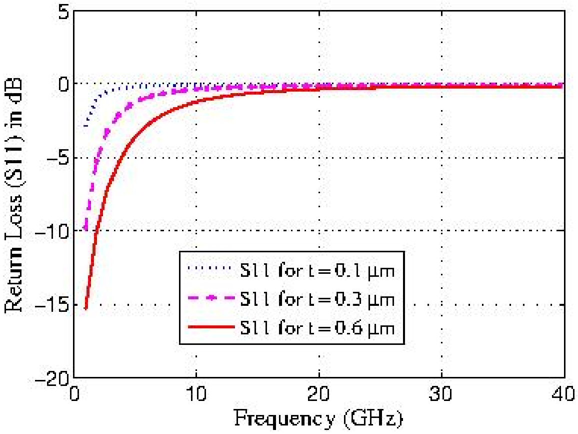

(c) Return Loss Vs dielectric thickness

Figure 3.6: Down state Return Loss Vs Beam Geometry

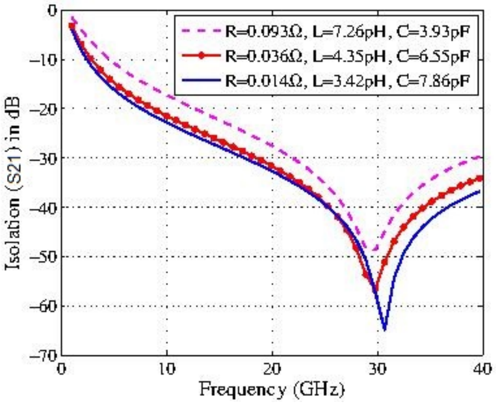

Figure 3.7: Extraction of model parameters from Isolation characteristics

ing strip and ground planes concentrate at the CPW gaps and the resulting current

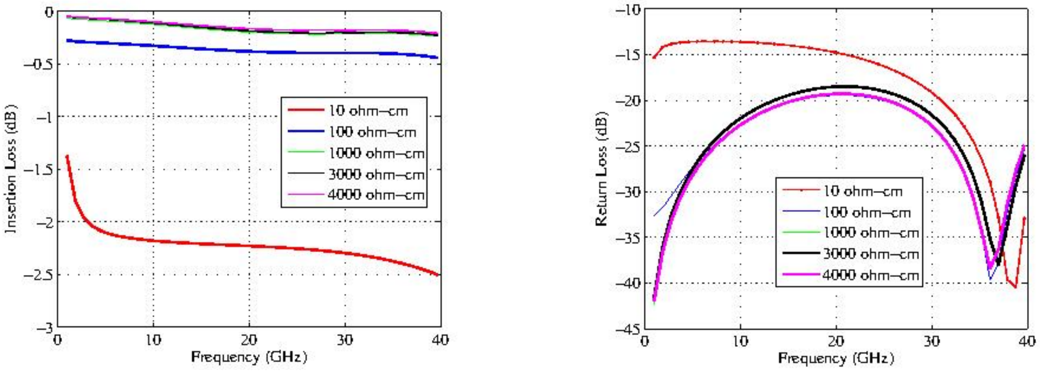

(a) Insertion Loss (S_{21})

(b) Up state Return Loss (S_{11})

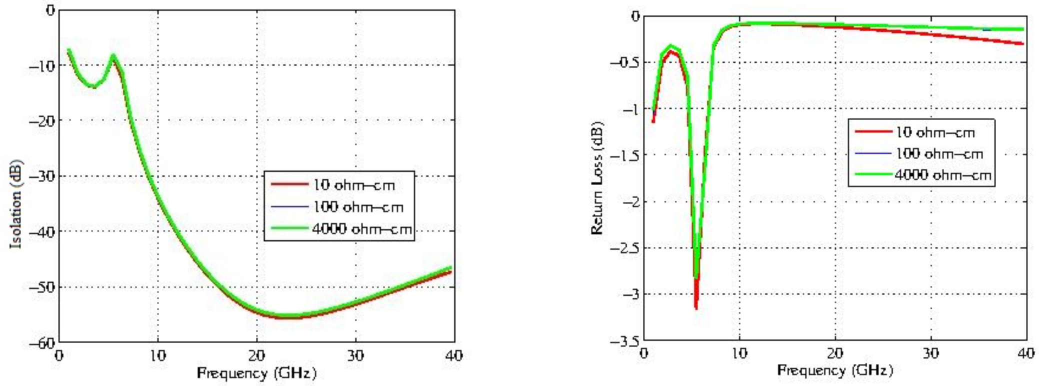

(c) Isolation (S_{21})

(d) Down state Return Loss (S_{11})

Figure 3.8: S-Parameters Vs Substrate resistivity

concentrate on the edges of the CPW signal and ground. Thus the beam inductance is dominated by the part of the beam over the CPW gap. Also the mutual inductance between current carrying parallel conductors of the beam and CPW contribute to the beam inductance. This results in isolation band of the switch getting tuned to the X, Ku and K bands. Inductance can also be enhanced by employing folded suspension beams because, the self inductance of a conductor is the sum of the mutual inductances of all pairs of filaments of which it is composed (Greenhouse (1974)).

The previous work on inductive tuning did not apply isolation band tuning to design switches for various bands. In addition to inductive tuning, the proposed structure, shown in figure 3.9, uses two shunt switches along the coplanar waveguide on a 0.4 mm thick silicon substrate ($\epsilon_r = 11.9$) to have improved isolation in the down state. CPW dimensions used are G/W/G equal to 60/100/60 μm to have 50 Ω impedance at the ports. However, the two switches will introduce reflection in the up state. To reduce this effect, the distance between the two switches is adjusted such that the RF signals reflected from these two switches cancel each other and will have minimum effect on the source at the input port. To improve the reliability of the structure, it is preferable to have the two switches close to each other. Thus, the separation (electrical length) between the switches is reduced by increasing the CPW line impedance from 50 Ω to 66 Ω by changing the CPW dimensions from 60/100/60 to 85/50/85 μm. The two switch configuration results in the cancellation of reflection from the switches at the input port at a particular frequency ω_r (determined by electrical length between the two switches), leading to OFF state return loss null at that frequency. Thus the electrical length between the switches can be adjusted to vary the frequency at which cancellation of reflection to occur at the input port. When switch is in OFF state (membrane up), signal travels down the transmission line from input to output. Neglecting beam resistance and inductance, the relation between electrical length of the high impedance line and frequency of null return loss is given by (Muldavin and Rebeiz (2000*b*)),

$$tan\ \beta l = \frac{2\ C_u\ \omega_r\ Z_1\ Z_0^2}{Z_1^2 - Z_0^2 + (C_u\ \omega_r Z_1 Z_0)^2} \tag{3.1}$$

where βl is the electrical length of the line of impedance Z_1, C_u is the up capacitance and Z_0 is the characteristic impedance at the ports. Thus the OFF state return loss null, S_{11}, can be made to occur at the same frequency but with a reduced transmission line length between the membranes provided $Z_1 > Z_0$.

3.3.1 Design and Modeling of RF MEMS Switches for X Band

Figure 3.9 shows the inductive tuned RF MEMS shunt switch for X-band frequencies. Inductive tuning of the beam is achieved by creating notches in the CPW ground plane (Topalli *et al.* (2009)) as shown in figure 3.9. The beams are made of gold and the dimensions of the beam are chosen to be 300 μm x 100 μm x 2μm ($L \times w \times T$), mounted 2 μm above the central conductor. Notches are created near the anchors of the two beams. The length of the notch is fixed to 170 μm and the width Z is variable from 36 to 39 μm with X is varied from 0 to 3 μm as shown in figure 3.9. In this design, a planar rectangular coil connects the membrane to the anchor.

Membrane inductance gets enhanced by this meander like suspension (Xiaofeng *et al.* (2004)) and the notch created in the CPW ground plane. HFSS simulation shows better isolation for this design in the 8-12 GHz band as shown in figure 3.10b. RF MEMS shunt switch isolation characteristics (S_{21} in down state) resembles series RLC resonance. RLC model values are extracted from isolation characteristics by curve fitting techniques. Table 3.3 shows the extracted inductance values. For the same beam dimensions, the rectangular coil suspension introduces an additional inductance of 3.2 pH compared to fixed-fixed non-meandered beam. With 170 μm x 37 μm notch, the switch gives maximum isolation of 71 dB at 10 GHz. Table 3.3 shows the enhancement of inductance due to notch and the meandered beam in comparison with fixed-fixed non meandered suspension. Figure 3.11 shows the displacement or deflection of the membrane in the Z direction with applied voltage. The pull-in and lift-off voltages can be seen in the hysteresis curve. The pull-in occurs at 7.8125 V.

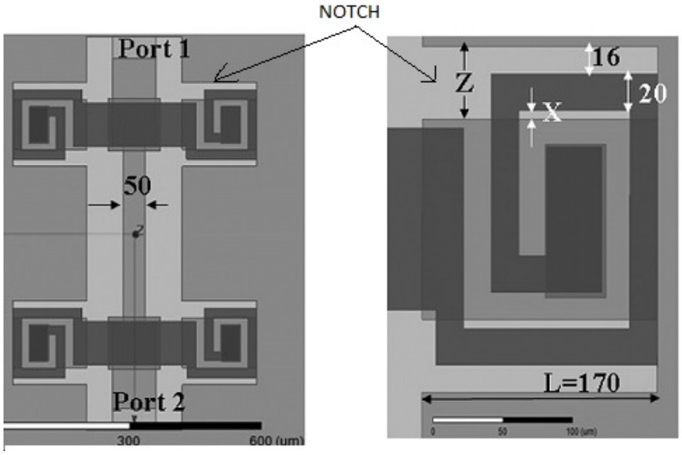

Figure 3.9: Diagram of inductive tuned switch for X-band

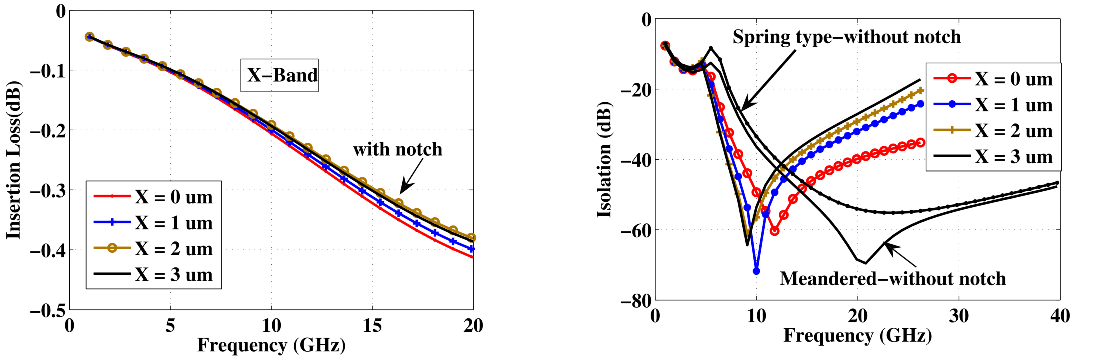

(a) Insertion Loss **(b)** Isolation

Figure 3.10: Isolation and Insertion Loss of X-Band switch

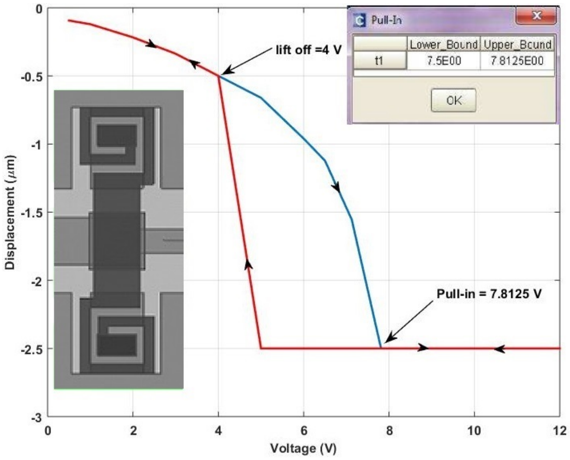

Figure 3.11: X band switch: DC Characteristics (Hysteresis Curve)

Table 3.3: Summary : RF MEMS X-band Shunt Switch

Width of Notch (Z μm) L=170μm, Z = (36+X)μm	f_r † (GHz)	Inductance (pH) ($L_T = L_b + L_N$)	L_N (pH)	Isolation at f_r(dB)
36 μm	11.8	46.3	31.4	-60.38
36 + (X = 1) μm	10	64.5	49.6	-71.8
36 + (X = 2) μm	9.1	77.91	63	-61.13
36 + (X = 3) μm	9.1	77.91	63	-64.40
Meandered beam, without notch	20.8	L_b = 14.9	-	-69.57
Spring beam, without notch	23.5	L_b = 11.68	-	-55.2

† f_r is the resonant frequency. See (3.2)

3.3.2 Electrical model of the Inductively Tuned Switch

The electrical model of the inductively tuned switch is shown in figure 3.12. L_N is the equivalent membrane series inductance added by the ground plane notch, L_n is the transmission line series inductance due to the notch and L_b is the inductance of the meandered suspension over the CPW gaps. L_n can be extracted from ON state S_{11} where as L_N and L_b from OFF state S_{21}. HFSS simulation shows that resonant frequency of the switch is found to be lowered to 10 GHz from 20.8 GHz by the notch of dimension 170 μm x 37 μm. Increased Q factor explains the improved isolation and tuning of the isolation band to 8-12 GHz. The notch introduces an inductance of 49.6 pH at 10 GHz. The down state resonant frequency of the membrane is given by

$$f_r = \frac{1}{2\pi\sqrt{(L_b + L_N)C_d}} \tag{3.2}$$

where the down capacitance, C_d, is given by (2.18). For the designs discussed in this work, C_d is found to be 3.93pF.

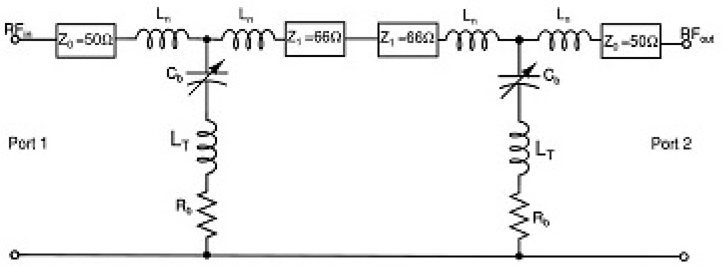

Figure 3.12: Equivalent Circuit of X-band switch.

3.3.3 Calculation of Inductance for Meander beams

Consider the planar rectangular coil represented schematically in figure 3.13. The total inductance of this coil is equal to the the sum of the self inductances of each of the straight segments (L_1 + L_2 + L_3 + L_4+ L_5 + L_6 +L_7 + L_8) plus all the mutual inductances between the segments. The mutual inductance between segments 1 and 5 has a component $M_{1,5}$ caused by the current flowing in segment 1 and a component $M_{5,1}$ caused by the current flowing in segment 5. Since the frequency and phase in both segments are identical, the total mutual inductance linking them equals

$M_{1,5} + M_{5,1}$. Analogous relationship exists between segment pairs 2-6,3-7 and 4-8. In each of these pairs, current flow is in the same direction in both sgements and all the mutual inductances are positive. The mutual inductnace between segments 1 and 7, on the other hand, has a component $M_{1,7}$ caused by the current in segment 1 and a component $M_{7,1}$ caused by current in segment 7. The total mutual inductance linking these two segements equal $M_{1,7} + M_{7,1}$ but is negative because current flow in segment 1 is opposite in direction to current flow in segment 7. Analogous relationship exists between segment pairs 1-3,5-7,5-3,2-8,2-4,6-8 and 6-4. Current magnitude is identical in all segments, with the result that $M_{a,b} = M_{b,a}$. The total inductance L_T for the given coil is given by, (Varadan *et al.* (2003)),

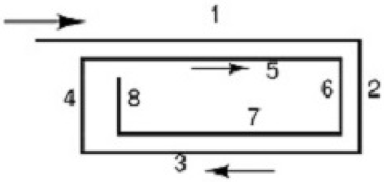

Figure 3.13: Two Turn Rectangular Coil

$$L_T = \sum_{s=1}^{8} L_s + 2(M_{1,5} + M_{2,6} + M_{3,7} + M_{4,8}) - 2(M_{1,7} + M_{1,3} + M_{5,7} + M_{5,3} + M_{2,8} + M_{2,4} + M_{6,8} + M_{6,4}) \tag{3.3}$$

The general equation can be written as,

$$L_T = L_0 + M_+ - M_- \tag{3.4}$$

where L_T is the total inductance, L_0 is the sum of the self inductances of all the straight segments, M_+ is the sum of the positive mutual inductances and M_- is the sum of the negative mutual inductances. For rectangular cross sections, self inductance is given by

$$L = 0.002 * l \left(ln\left[\frac{2l}{a+b}\right] + 0.50049 + \left[\frac{a+b}{3l}\right]\right)$$

where l is the length, a and b are rectangular dimensions. The mutual inductance(M) between two parallel conductors is a function of the length of conductors and of the geometric mean distance (GMD) between them. M is given by

$$M = 2 * l * Q \tag{3.5}$$

where M is in nanohenries and l is in centimetres and Q is the mutual inductance parameter given by

$$Q = \; ln\left(\frac{l}{GMD} + \sqrt{1+\frac{l^2}{GMD^2}}\;\right) - \sqrt{1+\frac{GMD^2}{l^2}} + \frac{GMD}{l} \tag{3.6}$$

In this equation, l is the length corresponding to the subscript of Q and GMD is the geometric mean distance between the two conductors, which is approximately equal to the distance d between the track centers. The exact value of GMD may be calculated from (3.7).

$$ln(GMD) = ln(d) - \left(\frac{1}{12(\frac{d}{w})^2} + \frac{1}{60(\frac{d}{w})^4} + \frac{1}{168(\frac{d}{w})^6} + \frac{1}{360(\frac{d}{w})^8} + ...\right) \tag{3.7}$$

Now consider the two conductor geometry represented schematically in Fig.3.14. Two conductors of length j and m are separated by a geometric mean distance, GMD. In this case,

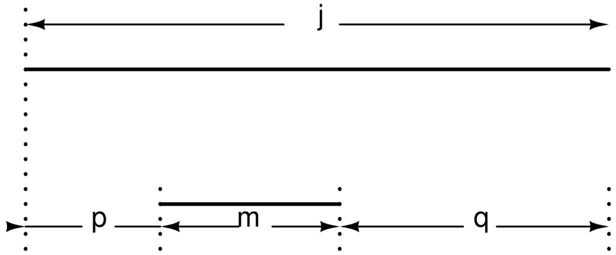

Figure 3.14: Two Parallel conductor geometry

$$2M_{j,m} = +(M_{m+p} + M_{m+q}) - (M_p + M_q) \tag{3.8}$$

and individual M terms are calculated using (3.5) and the length corresponding to the subscripts can be represented as,

$$M_{m+p} = 2 \; l_{m+p} \; Q_{m+p} = 2 \; (m+p) \; Q_{m+p} \tag{3.9}$$

where Q_{m+p} is the mutual inductance parameter for $\frac{GMD}{m+p}$.

For $p = q$, $\quad M_{j,m} = M_{m+p}$ - M_p

For $p = 0$, $\quad 2 \; M_{j,m} = (\; M_j + M_m)$ - M_q

3.3.4 Shunt Switch for Ku Band

Figure 3.15 shows switch schematic tuned for Ku band operation. Beam geometry is modified to increase the membrane inductance through anchor notches (denoted by X+Y+Z in figure 3.15) and to have resonant frequency in the range 12-18 GHz. Isolation characteristics shown in Fig. 3.16 of the Ku band switch is found to be 59 dB at its resonant frequency of 17.2 GHz. The switch down capacitance remains the same at 3.93 pF as in previous design and the extracted inductance from the curve is 21.8 pH. With notch dimension of 90 μm x 37 μm, the isolation band gets lowered to the middle of Ku band with improved isolation of 75 dB at the resonant frequency of 14.5 GHz. The presence of notch enhances the series inductance by 8.8 pH to 30.68 pH. Table 3.4 shows the summary of the results of simulation for this design. The hysteresis curve given in Fig. 3.17 shows the actuation voltage and the displacement of the membrane. The membrane is displaced by 2.5 μm and snaps down to the dielectric at 15.625 V.

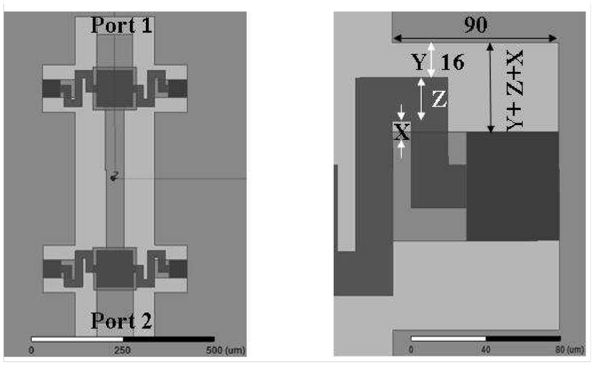

Figure 3.15: RF MEMS Shunt Switch for Ku band

Table 3.4: Summary : RF MEMS Shunt Switch - Ku Band

Width of Notch (W μm) L = 90μm, W = (36+X)μm	f_r (GHz)	Inductance (pH) ($L_T = L_b + L_N$)	L_N (pH)	Isolation at f_r(dB)
36 + (X = 1)μm	14.5	30.68	8.88	-75.12
36 + (X = 2) μm	14.5	30.68	8.88	-68.37
36 + (X = 3) μm	14.5	30.68	8.88	-62.16
36 + (X = 4) μm	15.4	27.2	5.4	-46.89
Meandered beam, without notch	17.2	$L_b = 21.8$	-	-59.21
Spring beam, without notch	23.5	$L_b = 11.68$	-	-55.2

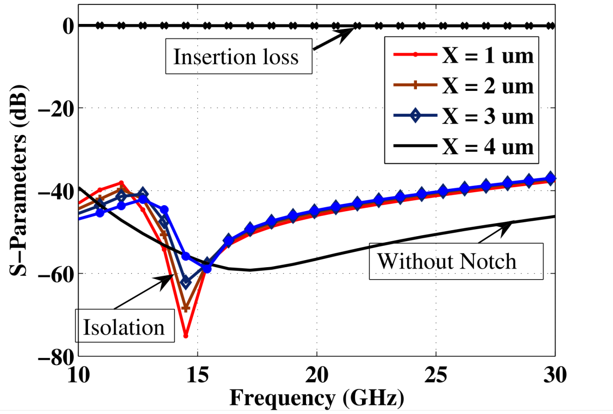

Figure 3.16: S-Parameters : Ku band Switch

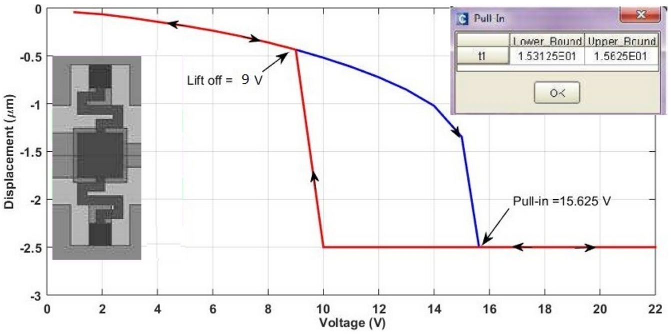

	Lower_Bound	Upper_Bound
t1	1.53125E01	1.5625E01

Figure 3.17: Ku band switch: DC Characteristics (Hysteresis Curve)

3.3.5 RF MEMS switch for K Band

For tuning RF MEMS shunt switch to the K band (18-26 GHz), fixed-fixed flexure geometry is used for the beam. This geometry gives an isolation of 55 dB at the resonant frequency of 23.5 GHz. To lower the resonant frequency by a few GHz to suit the K-band operation, notches (denoted by X in figure 3.18) are created in the ground plane. It has been observed from HFSS simulation that the resonant frequency is lowered to 19.9 GHz for a notch dimension of 100 μm x 5 μm. Table 3.5 gives the tuned inductance values and corresponding isolation. The displacement Vs voltage plot gives the pull-in voltage as 11.875 V.

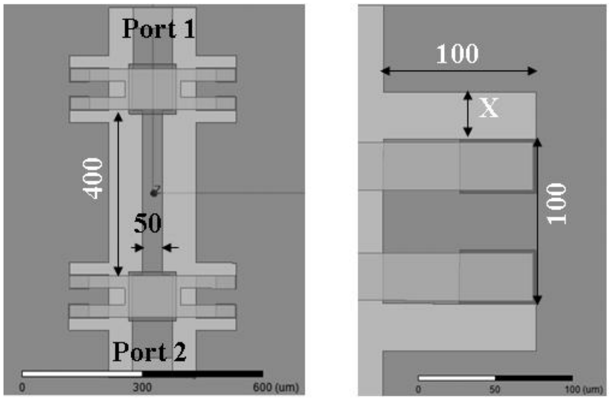

Figure 3.18: RF MEMS shunt switch for K-band

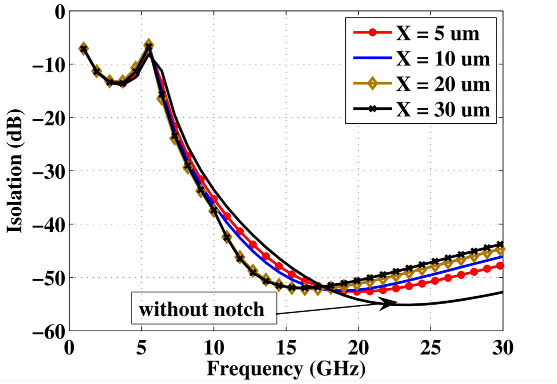

Figure 3.19: Isolation characteristics : K band

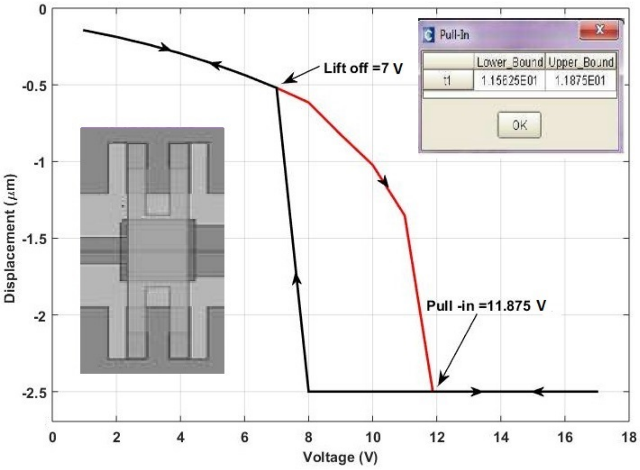

	Lower_Bound	Upper_Bound
1	1.15625E01	1.1875E01

Figure 3.20: K band switch: DC Characteristics (Hysteresis Curve)

Table 3.5: Summary : RF MEMS Shunt Switch - K Band

Width of Notch (X μm) L = 100μm	f_r (GHz)	Inductance ($L_T = L_b + L_N$)(pH)	L_N (pH)	Isolation at f_r (dB)
X = 5 μm	19.9	16.28	4.6	-52.67
X = 10 μm	19	17.8	6.12	-52.50
X = 20 μm	16.3	24.28	12.6	-52.17
X = 30 μm	16.3	24.28	12.6	-51.96
Without Notch	23.5	L_b = 11.68	-	-55.16
Spring beam	23.5	L_b = 11.68	-	-55.2

3.3.6 RF MEMS switch for Ka Band

For tuning RF MEMS shunt switch to the Ka band (27-40 GHz), fixed-fixed flexure geometry shown in figure 3.21a is used for the beam. This geometry gives an isolation in excess of 60 dB at the resonant frequency of 31.5 GHz. With no meandered membranes and notches in the ground plane, the series inductance is less in the signal path during actuation of the switch. Therefore, the resonant frequency of the switch is higher than the previous structures, making it suitable for applications in Ka band. MEMS switches with S-parameters tuned for Ka band find use in reconfigurable antennas. Such reconfigurable antennas offer great potential in wireless communication systems because they can provide diversity features in operating frequency, polarization and radiation pattern.

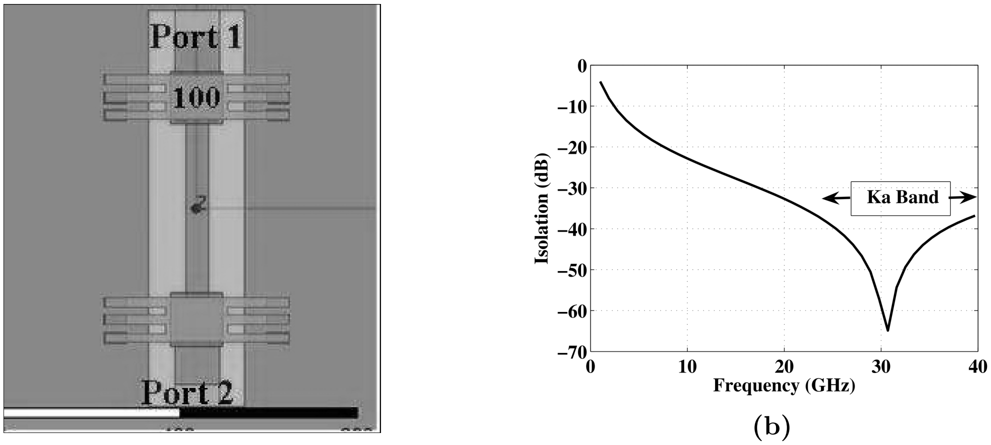

(a)

(b)

Figure 3.21: Ka band RF MEMS shunt switch (a) Schematic (b) Isolation.

The displacement of the membrane with applied DC voltage is shown in figure 3.22. DC simulation in CoventorWare shows that the switch is actuated at 18.125 V. High voltage is required only at the point of actuation and once the membrane is pulled down the electrostatic forces are strong enough to maintain the latch at a lower voltage. The restoring forces bring back the membrane when the applied voltage goes below the lift-off value. The hysteresis is partly due to strong electrostatic forces and partly due to dielectric charging. High pull-in voltage results in a strong electric field in the order of few MV/cm across the dielectric layer causing the charges to tunnel into the dielectric. These trapped charges in the dilectric have fairly a large recombination time lasting up to several hours. This affects reliability and lifetime of the device.

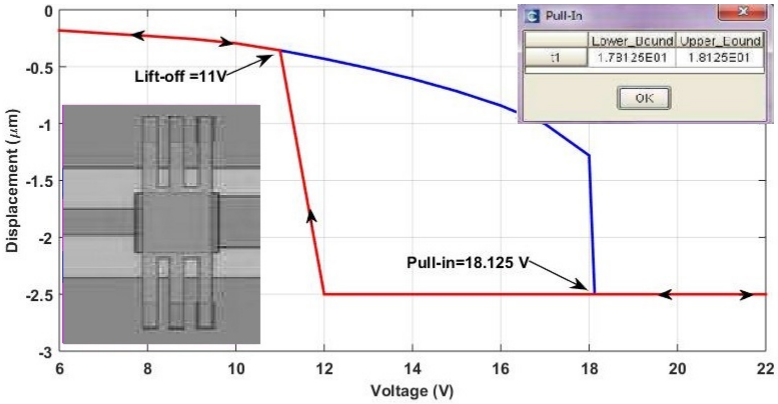

	Lower_Bound	Upper_Bound
t1	1.78125E01	1.8125E01

Figure 3.22: DC Characteristics Ka Band: Hysteresis Curve

3.4 Fabrication and Characterization

3.4.1 Fabrication

Figure 3.24 outlines the procedures followed in this work to fabricate the switches. Table 3.6 lists the material parameters and switch dimensions. The RF MEMS capacitive switches are fabricated on 4-inch wafer having 400μm thick high resistive silicon (HR) substrate by a five mask surface micromachining process. Wet chemical cleaning prepares the silicon surface for fabrication. SiO_2 ($1\mu m$) is deposited on the substrate surface by high temperature furnace exposure while passing O_2 along with steam. To generate CPW transmission line, 1.5 μm thick layer of gold is deposited by E-beam sputtering. CPW pattern is created by photolithography (Mask I exposure) as shown

Table 3.6: Geometric dimensions and material properties

Parameters and Properties	Dimensions and Values
CPW dimensions (G/W/G)	60/100/60 (μm)
Membrane Dimension (l*b*t) μm	(320*100*1.5) μm
Capacitor overlap area	100 μm * 100 μm
Dielectric area	120 μm * 120μm
Membrane material	Gold
Membrane Height	2.5 μm
Young's modulus of Gold	78 GPa
Poisson's Ratio of Gold	0.42-0.44
Relative permittivity of Silicon	11.9

in step (a) of figure 3.24 and plasma asher strips off photoresist to reveal a clear CPW pattern. Though the simulated design shown in figure 3.9 had notches created on the CPW ground lines on either side of the beam anchors, these notches were not included in the CPW pattern during fabrication, for the stability of the anchors.

Low thermal oxide (LTO) of thickness 0.2 μm is deposited over actuation pad (CPW signal line) to form a dielectric cover and the layer is patterned using photolithography (Mask II exposure) and wet oxide etching as shown in step (b) of figure 3.24. Mask III exposure using mask aligner is performed for creating planarization pattern and the surface planarization is verified by 2D/3D profiler. The planarization process is done to prevent sagging of the switch membrane over the CPW gaps and thus to produce a flat profile. This is shown in step (c) of figure 3.24.

Mask IV exposure with a mask aligner transfers the anchor pattern over 2.5 μm thick negative photoresist (PR) layer and a wet chemical etch is carried out to reveal the anchor pattern as given in step (d) and (e) of figure 3.24 . Plasma asher processing step is done to clear anchor holes. Metallization process involves depositing 1.5 μm thick layer of gold by DC plasma sputtering for the formation of anchor and switch beam. Fifth stage photolithography involves mask V exposure which transfers switch beam pattern over 1 μm positive photoresist and metal etching by wet chemical etch reveals the switch membrane of desired pattern. Subsequent plasma asher processing removes 2.5 μm thick photoresist from underneath the patterned beam and thus releasing the switch membrane as shown in step (f) and (g) of figure 3.24. Superimposed mask layers with alignment marks are shown in figure 3.23.

The membrane after release is shown in figure 3.25a. Carbon dioxide critical point drying is performed at 1200 Psi and 30 ^{o}C to prevent possible stiction of the floating

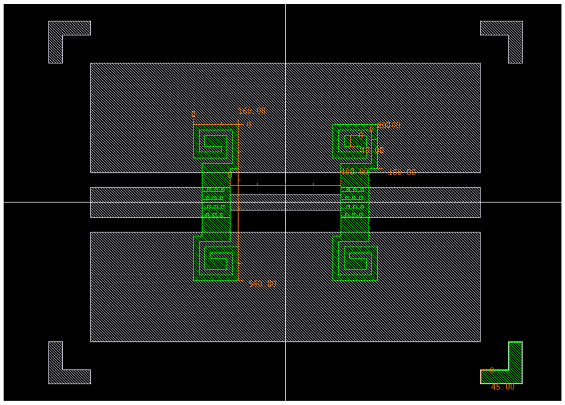

Figure 3.23: Superimposed mask layers of X band RF MEMS Switch

membrane. The switches are later examined using scanning electron microscope.

The fabrication process followed in this work produced an average yield of nearly 10-15 %. On testing, it is observed that the yield is better on devices fabricated close to the centre of the wafer as the process non-uniformities are much lower in this region. Many devices on the wafer were precisely inspected for possible defects and the selected few were tested. Many devices were rendered unusable due to minute cracks developed in the serpentine legs holding the membrane. Scanning electron microscope (SEM) and optical profiler were employed for inspection and measurements. Measurements were also carried out during intermediate fabrication steps to verify the dimensions such as dielectric thickness, beam thickness and capacitor air gap.

3.4.2 Characterization Results

On-wafer RF probing is performed to study the DC and RF performance of the fabricated devices and to identify and select the better devices for packaging. In electrical DC characterization, capacitance versus voltage characteristics of the fabricated RF MEMS switch are obtained using Agilent DC probe station. In RF characterization, scattering parameters (S-Paramaters) of the fabricated switches are measured using Agilent Power Network Analyzer and Cascade probe station equipped with ground-signal-ground (GSG) RF and DC probes of 200 μm pitch. Measurement has been performed under ambient environmental conditions. Prior to measurement, short-open-load-thru (SOLT) calibration is performed from DC to 40 GHz. SEM images are generated for plan and elevation of the fabricated devices for accurate measurement of actual dimensions after fabrication. Figures 3.25a and 3.25b present SEM images

(a) CPW mask

(b) Dielectric oxide mask

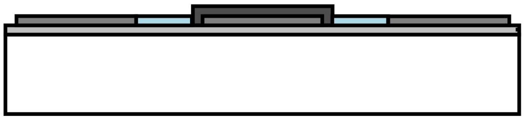

(c) Planarization mask

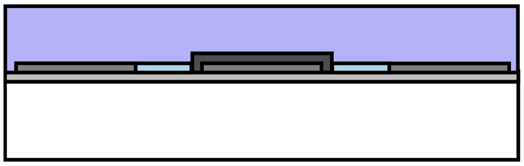

(d) Negative photoresist mask

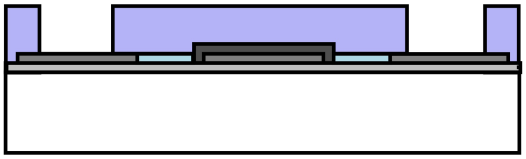

(e) Wet chemical etch

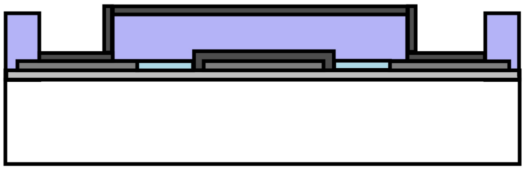

(f) Anchor and beam mask

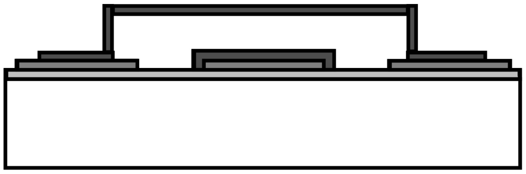

(g) Release

Figure 3.24: Fabrication Steps

showing lateral dimensions of airgap, anchor and standing membrane. Mechanical characterization of switches are performed in Laser Doppler Vibrometer (LDV) to study the proper release of the metallic membrane. This non contact technique extracts the amplitude and mechanical resonant frequency of the vibrating membrane from the Doppler shift of scattered laser from moving surface.

Figure 3.26a presents the SEM image of the proposed RF MEMS shunt switch tuned for X band (8-12 GHz) performance. Figure 3.26b shows the capacitance Vs voltage characteristics of the RF MEMS switch given in figure 3.26a. Capacitance - voltage characteristics shows that the metallic switch membrane actuates at 10 volts, thus increasing the shunt capacitance from 90 fF in the un-actuated state (up state) to 1.88 pF at pull-in (down state). This large C_d/C_u ratio of 20.9 offers the switch acceptable isolation in the off state. S-parameters of the fabricated RF MEMS shunt capacitive switches are obtained for signals from 1 to 40 GHz. The RF performance of X band switches is given in figure 3.27. It is seen that insertion loss (S_{21}- switch OFF) is better than -0.4 dB and isolation (S_{21}-switch OFF) is better than -35 dB in the designed band of 8-12 GHz as given in figure 3.27a and figure 3.27b respectively.

The SEM photograph of RF MEMS switch for Ku band (12-18 GHz) and etch

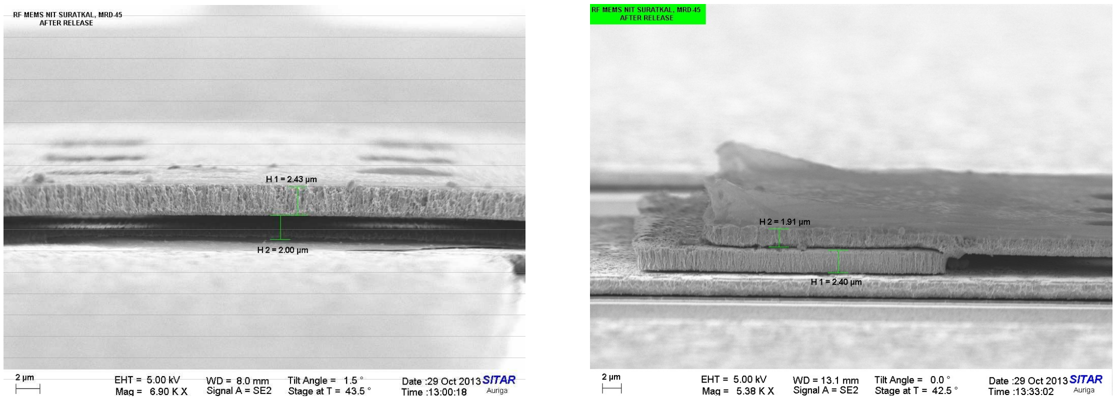

(a) Released switch membrane - elevation **(b)** Shunt membrane on anchor - side view

Figure 3.25: Vertical dimension of airgap, anchor and membrane

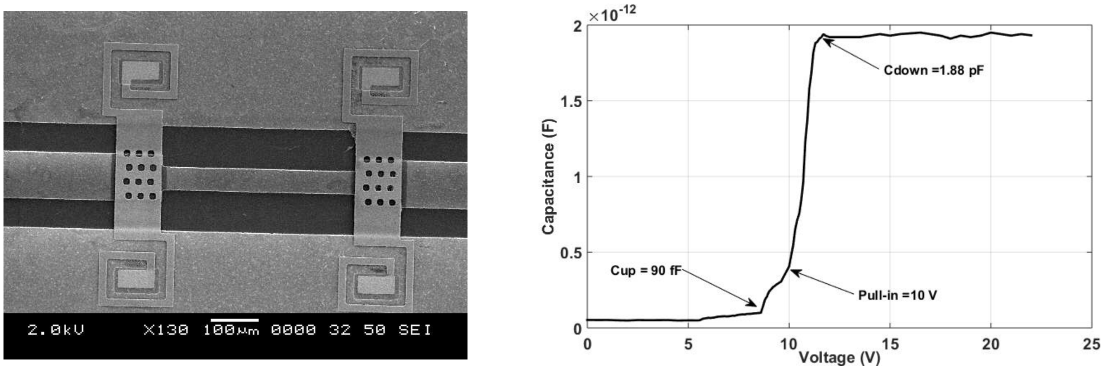

(a) SEM image of X band switch **(b)** C-V Characteristics

Figure 3.26: SEM Photograph and corresponding C-V characteristics

masks for the various layers of fabrication are shown in figures 3.28a and 3.28b respectively. DC characteristics of the above switch given in figure 3.29a shows that the actuation occurs at 18.5 volts and the OFF and ON capacitances are 53 fF and 1.7 pF respectively. From the S-parameter plot of the Ku band in figure 3.29b, it can be seen that the measured value of insertion Loss (OFF state S_{21}) is better than -0.46 dB and isolation (ON state S_{21}) is better than -30 dB in the 12-18 GHz frequency band. The measured ON state return loss S_{11} of the switch is shown in figure 3.30 and is better than -25 dB in the desired frequency range. The mid-section transmission line impedance ($Z_1 = 66\Omega$) and its electrical length (βl) are optimized to cause the cancellation of the reflected waves from the two switch membranes at the input port. From these measured S-Parameter values, it can be inferred that this switch has acceptable RF performance suitable for multiband applications in X (8-12 GHz) and

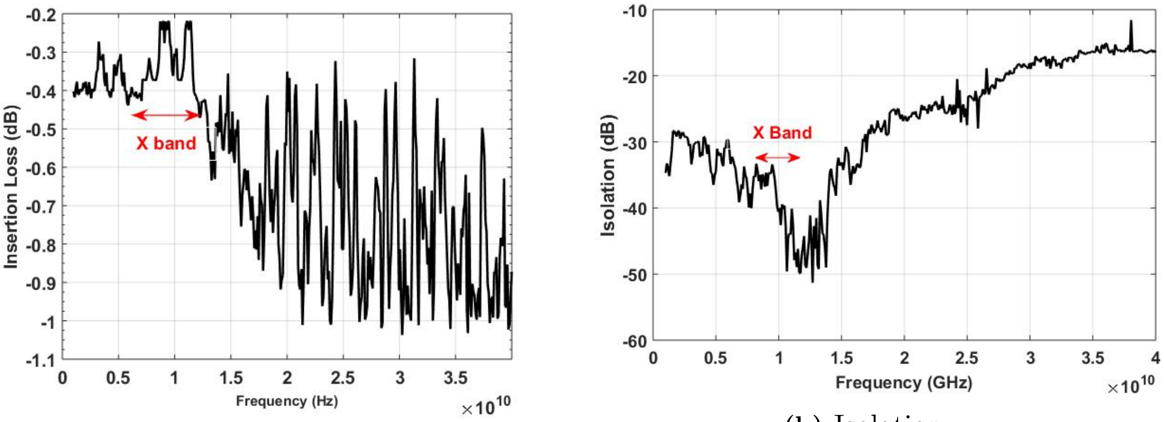

(a) Insertion Loss (S_{21})

(b) Isolation

Figure 3.27: RF Characteristics of X Band MEMS shunt switch

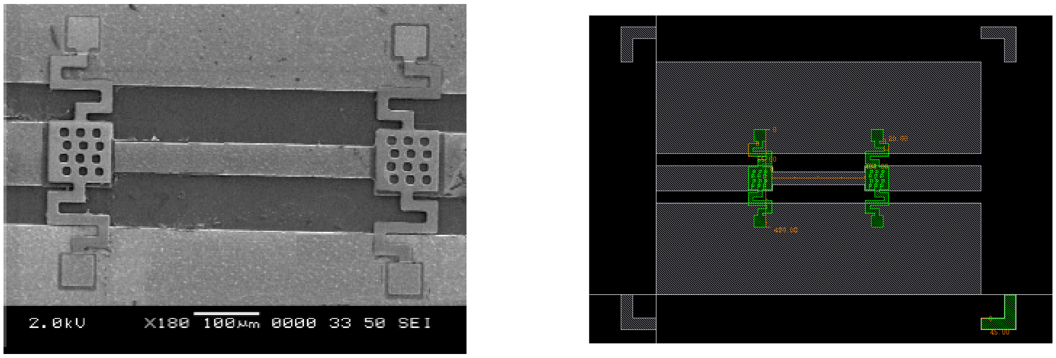

(a) SEM image of Ku band switch

(b) Mask layers showing alignment marks

Figure 3.28: SEM image and mask layers of Ku band MEMS switch

Ku (12-18 GHz) bands.

The SEM images of MEMS switches designed for K band (18-27 GHz) performance is shown in figure 3.31a. Etch holes of 8 μm in diameter, as seen in the SEM image shown in figure 3.31b, are made on the actuating membrane with a spacing of 20 μm and 25 μm respectively along the width and length of the membrane. These holes aid in the faster removal of sacrificial layer resulting in proper release of the membrane. During actuation, these holes takes care of squeeze film damping and effect faster switching. Loss characteristics and isolation of the K band switch are given in figure 3.32a. The insertion loss in the band of 18-27 GHz is found to be better than -0.3 dB and isolation characteristics is observed to peak at 23.5 GHz and is better than -35 dB in the desired band. Characterization of the fabricated

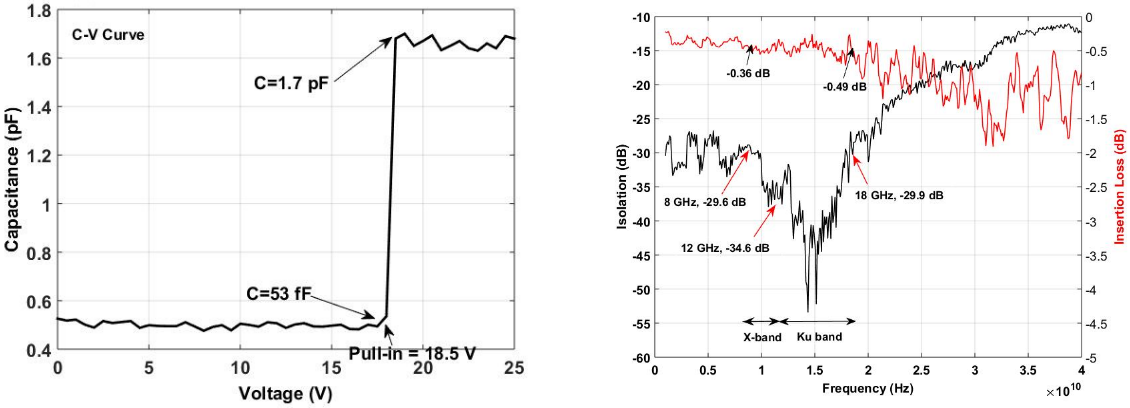

(a) CV characteristics of Ku band switch

(b) RF characteristics

Figure 3.29: Ku Band RF MEMS switch - Measured DC and RF characteristics

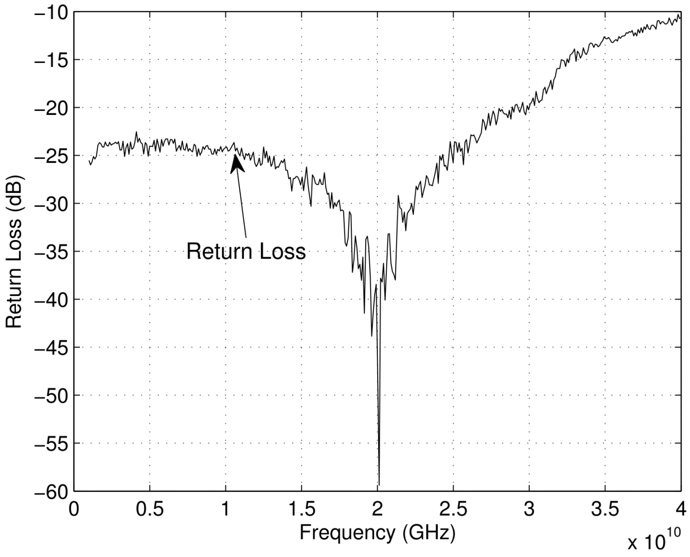

Figure 3.30: ON state Return Loss

devices is also done in Laser Doppler Vibrometer (LDV) to study the mechanical resonant frequency of the switching membrane. The Doppler shift of the laser beam reflected from the vibrating membrane is used to estimate the frequency of mechanical resonance.

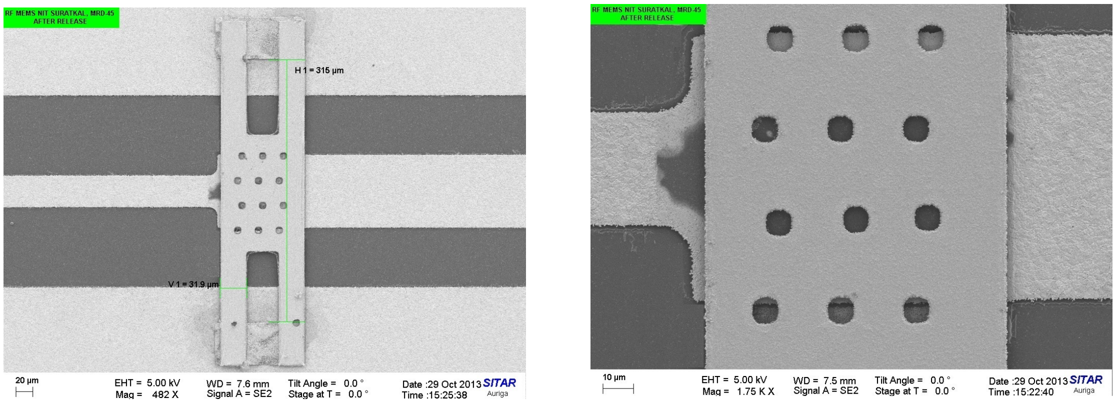

(a) SEM photograph of K band switch **(b)** SEM Image of etch holes

Figure 3.31: SEM images of K band switch

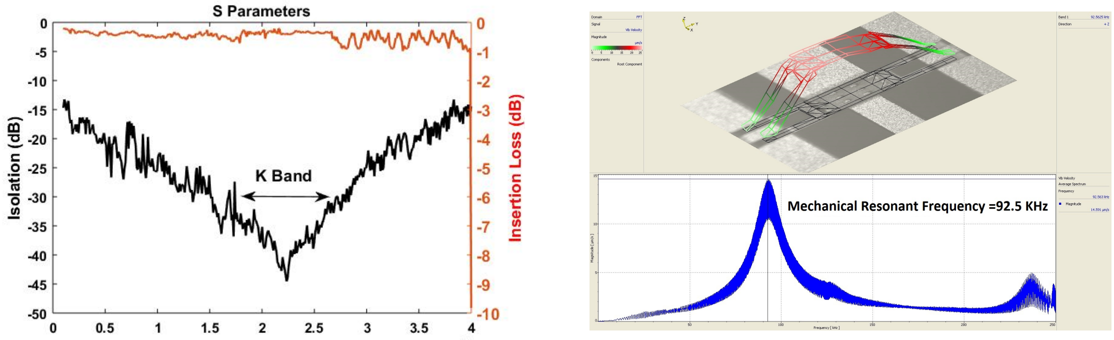

(b) Frequency of mechanical resonance of switch membrane from LDV

(a) Loss and isolation characteristics

Figure 3.32: Measured electrical and mechanical characterization results

3.5 Comparison with published results

As discussed in the previous sections, the RF shunt switches designed in this work have been inductively tuned for X, Ku, K and Ka bands and it is seen that they exhibit excellent RF characteristics in these bands. These switches also have relatively lower pull-in voltage. Table 3.7 shows the comparison of this work with previously published work. As can be seen from the table, except for the switching time, the designed switches are superior in all other aspects.

Table 3.7: **Performance Comparison of Capacitive Shunt Switches**

Capacitive shunt Switches	Blondy et.al. 2004	Fernandez et. al. 2008	K. Topalli 2009	Persano et.al. 2011	This work
Suspended Beam	0.35 μm Al-Au	0.9 μm Ni	1.2 μm Au	1.5 μm Au	2.0 μm Au
Dielectric Material & Thickness	Dielectric Less	AlN 300 nm	Si_3N_4 300 nm	$T_{a2}O_5$ 350 nm	Si_3N_4 200 nm
Airgap	0.3 μm	2.5 μm	3.0 μm	3.0μm	2.0 μm
Spring Constant	15-20 N/m	9-12 N/m	15-20 N/m	–	10 -20 N/m
Insertion loss	1.5 dB	0.2 dB	0.3 dB	0.8 dB	0.2 - 0.4 dB
Isolation	20 dB	38.5 dB	40 dB	40 dB	54 dB
C_{up}	224 fF	40 fF	60-90 fF	–	50-90 fF
C_{down}	2.2 pF	1.55 pF	1.8 pF	–	1.7-1.9 pF
Capacitance ratio	10	39	20	–	21-34
Actuation Voltage	30 V	12 V	–	15-20 V	10-18.5 V
Switching time	–	–	10-15 μS	–	40-80 μS
Life time	–	$2x10^9$ cycles	–	–	–

Chapter 4

DESIGN AND SIMULATION OF THE SP4T RF MEMS SWITCH

4.1 Single Pole Multi Throw (SPMT) Switch

Single Pole Multi Throw (SPMT) switches have shown wide range of applications in different areas such as base stations, satellite communication, antenna switching systems, filter banks and multiband selectors. Traditionally, most of these applications use PIN diodes or FET switches due to good RF performance at lower frequencies. But, as the operating frequency of the system increases, the RF performance of semiconductor switches degrades.

Hence, in the last few years, more and more SPMT RF MEMS switches have been designed and are replacing the solid-state switches. Most of these are ohmic metal contact switches, which have the disadvantage of a limited power handling capability under hot-switching conditions compared to their counterparts, the capacitive switches.

In SPMT switches, ports are placed very close to each other to achieve low response time. But this can affect isolation between the input and different output ports and hence is a major challenge in designing such switches.

4.2 Proposed Model

As seen from the literature (Tan *et al.* (2003), Roy and Rangra (2010), Zareie and Rebeiz (2014), Yang *et al.* (2014), Dey and Koul (2015)), over the years, many improvements have been done in achieving low insertion loss, high isolation and reduced pull-in voltage without affecting RF performance and reliability. Achieving good RF characteristics and optimizing them is a difficult objective in SPMT switches compared to SPST switches. Many approaches used in the literature for low loss and better isolation in SPST switches may not be suitable in the case of SPMT switches. In the present work, a number of modifications have been done while designing SPMT switches for achieving good RF performance, as listed below.

A cascade combination of series and shunt SPST switches are placed in each of the arms of SPMT model, to improve RF characteristics. Use of a spring structure with four cantilever flexure supports to achieve low spring constant and reduced area. Combination of series shunt switches also helps to avoid complex structures like MEMS motors which are normally used in multi port switches. The bridge structure used to implement the shunt switch structure is anchored across the signal lines and attached to the ground planes on both sides, while series switch is directly attached to the substrate instead of ground planes. In both the switches, separate actuating electrode is placed on both sides of the signal line for electrostatic actuation of the switch. Separate actuating electrodes are necessary in multi port switches for ease of switch control.

4.3 Design and Simulation of the SP4T RF MEMS Switch for X Band

This section focuses on the design and simulation of a SP4T switch for X band application for improved RF parameters such as insertion loss, isolation and return loss.

4.3.1 General Fabrication Process

Using CoventorWare tool, the first step in electro-mechanical design is the generation of the process file, which is followed by layout design. Using this process file and layout, 3D structural model is generated. This is followed by assigning the mesh to the structure to perform simulation and analyses.

The selection of materials and fabrication process is based on the compatibility with standard IC fabrication processes of the fab used. Most RF MEMS switch fabrication follows standard processing steps. In this switch, Silicon (Si <100>) substrate of thickness 500 μm is used. SiO_2 coating is provided above the Si substrate to isolate it from the upcoming layers stack. Normally next stage is the fabrication of the signal line and ground planes. However, in this design, separate actuation electrode based approach is used. Hence, first, electrodes are fabricated, followed by signal line and ground planes. The RF MEMS switches are generally implemented as two terminal devices, where the dc control voltage is also applied to the signal line along with the RF signal. In the present work, a separate DC electrode is provided for electrostatic actuation.

The signal line, ground planes and electrodes are fabricated using gold (Au). Si_3N_4 is preferred as dielectic material. A thin dielectric layer of 0.1 μm is deposited and patterned for shunt switch. The next step is to deposit and pattern the sacrificial (spacer) layer. The thickness of the spacer layer is decided by the air gap required between the CPW and suspended structure. The air gap in this switch is 2.5 μm. SU8 photoresist is selected as the material for spacer layer. The hanging structure is defined by depositing and patterning around 1.5 μm thick gold layer over the sacrificial layer. This is followed by the removal of sacrificial layer using an isotropic dry etch in oxygen plasma to avoid the sticition. Process file in CoventorWare is given in figure 4.1.

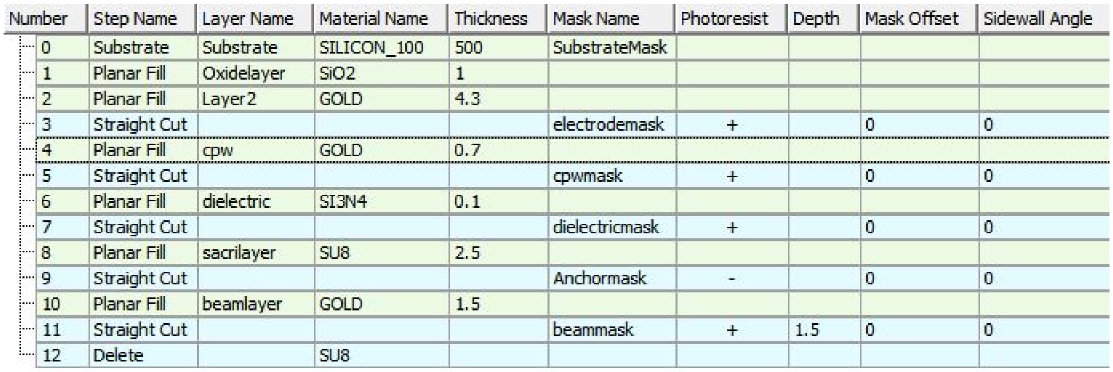

Number	Step Name	Layer Name	Material Name	Thickness	Mask Name	Photoresist	Depth	Mask Offset	Sidewall Angle
0	Substrate	Substrate	SILICON_100	500	SubstrateMask				
1	Planar Fill	Oxidelayer	SiO2	1					
2	Planar Fill	Layer2	GOLD	4.3					
3	Straight Cut				electrodemask	+		0	0
4	Planar Fill	cpw	GOLD	0.7					
5	Straight Cut				cpwmask	+		0	0
6	Planar Fill	dielectric	SI3N4	0.1					
7	Straight Cut				dielectricmask	+		0	0
8	Planar Fill	sacrilayer	SU8	2.5					
9	Straight Cut				Anchormask	-		0	0
10	Planar Fill	beamlayer	GOLD	1.5					
11	Straight Cut				beammask	+	1.5	0	0
12	Delete		SU8						

Figure 4.1: Process file in CoventorWare.

4.3.2 Layout Design of the switch

The process file defines thee vertical details of the structure, while layout design defines the mask positions. For getting correct structure, masks must be properly arranged. The layout design of the series-shunt switch is given in figures 4.2a and 4.2b.

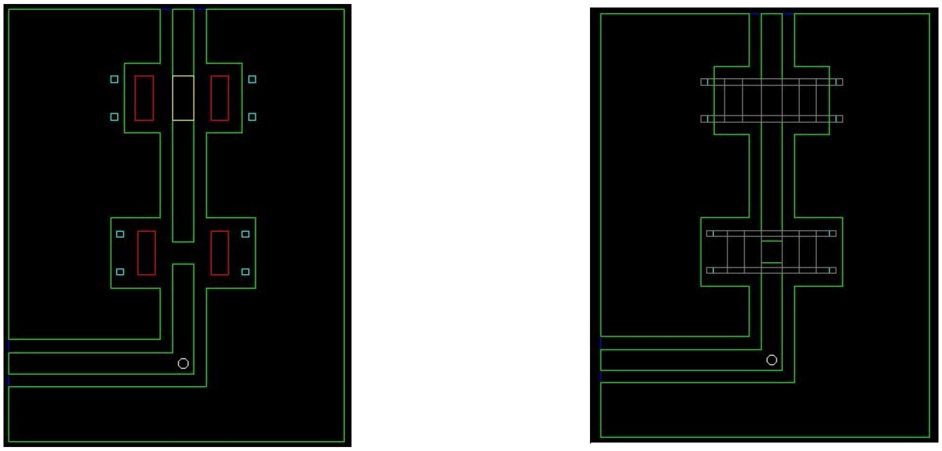

(a) Layout without beam. **(b)** Final layout.

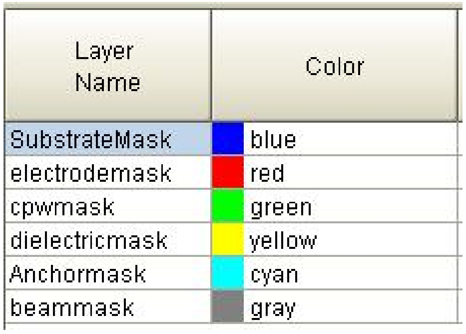

Layer Name	Color
SubstrateMask	🟦 blue
electrodemask	🟥 red
cpwmask	🟩 green
dielectricmask	🟨 yellow
Anchormask	🟦 cyan
beammask	⬛ gray

(c) Legend.

Figure 4.2: Layout of the series shunt switch.

CoventorWare generates 3D model of the switch using process file and its layout. Using this model, different analyses such as *MemElectro, MemMech* and *CoSolve* are performed. In *MemElectro*, the tool has provision to apply any potential to the switch and allows the measurement of the capacitance between the plates. Measurement and analysis of displacement due to different forces applied on the switch membrane can be done using *MemMech*. It can also be used to study dynamic characteristics and resonant frequency of the switch. *CoSolve* combines both *MemElectro* and *MemMech*, and it can be used to measure pull-in and lift-off voltage of the switch. The model of the SP4T switch and the dimensions of the series-shunt combination between input and output port are shown in figures 4.3a and 4.3b respectively.

The cascaded series-shunt switch combination shown in figure 4.3b is designed to operate in X band (8-12 GHz) frequency. The series and shunt switches can be operated independently. When the series switch is in down state and shunt switch in up state, the combination is said to be in the ON state and when the combination

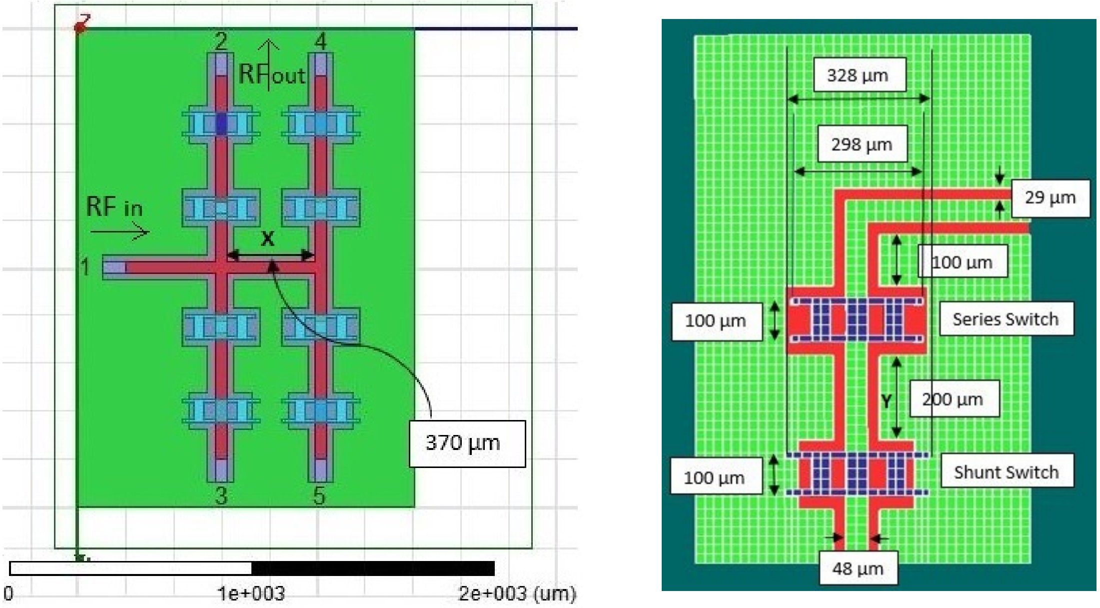

(a) SP4T switch model in HFSS

(b) Switch geometry dimensions

Figure 4.3: SP4T switch geometry build with performance optimized dimensions

is in OFF state, both switches reverse their positions. Dimensions of the designed switch are given in table 4.1.

Table 4.1: Parameters of the designed switch.

Parameter Name	Parameter Value (Series switch)	Parameter Value (Shunt switch)
Width of flexure (W)	15 μm	15 μm
Thickness of flexure (T)	1.5 μm	1.5 μm
Length of flexure (L)	125 μm	140 μm
Overlap area between beam and transmission line (A)	100 x 48 μm^2	100 x 48 μm^2
Gap between transmission line and bridge (g)	2.5 μm	2.5 μm
Thickness of dielectric (t)	-	0.1 μm
Spring Constant (k)	7.79 N/m	5.75 N/m

Parameter values are chosen based on the X band requirements. In literature, meander connections are used between the anchors and bridges to reduce the pull-in voltage. However in this work, meander springs are not used because they reduce the spring constant to very low value and when the switch is deactivated, the bridge does not return to its original position due to low spring constant and hence the reliability of the switch reduces.

4.3.3 Electromechanical simulation using CoventorWare

The actuation voltage and the dynamic response of the SPST MEMS switches, used in the design of SP4T, are extracted from electro-mechanical simulation in CoventorWare. The input RF signal gets connected to any of the four output ports, depending on the ON/OFF status of the pair of SPST switches in each of the signal paths. All the SPST switches in the design are actuated independently. The pull-in and lift off characteristics of the switches obtained from CoventorWare are studied and accordingly the dimensions of the 3-D model are optimized.

When the SP4T switch is turned ON, depending upon the actuation of the series and shunt switch combination, one or more output ports get the signal from the input port. As shown in figure 4.4a, to connect the signal from input to one of the the output ports, the series switch is electrostatically actuated and shunt switch remains unactuated in the signal path from input to output. Alternatively, if the series switch is unactuated and shunt switch is actuated, the input signal is blocked from reaching that output port as shown in figure 4.4b. Separate actuation pads are provided beneath the beam, on either side of the CPW signal line. It is to be noted that the series switch is ohmic (metal-metal) with anchors on the substrate whereas shunt switch is capacitive with anchors on CPW ground.

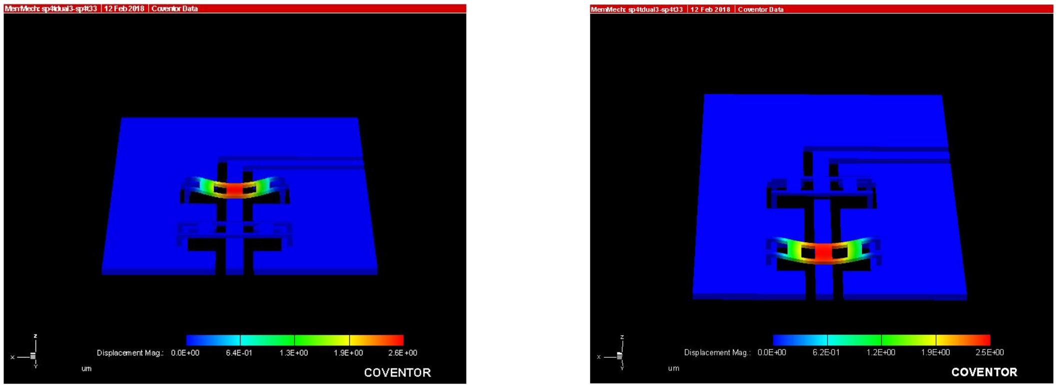

(a) Actuated membrane of the series switch -

(b) Actuated membrane of shunt switch

Figure 4.4: Actuated switch membranes in MEMS solver CoventorWare

FEM simulation also gives the mechanical resonant frequency of the switch membranes. The first natural resonant frequency of series switch membrane is 188.87 kHz and that of shunt membrane is 150.87 kHz. Pull-in and lift-off voltages of series and shunt switches are shown in the displacement versus voltage curve of figures 4.5a and

4.5b.

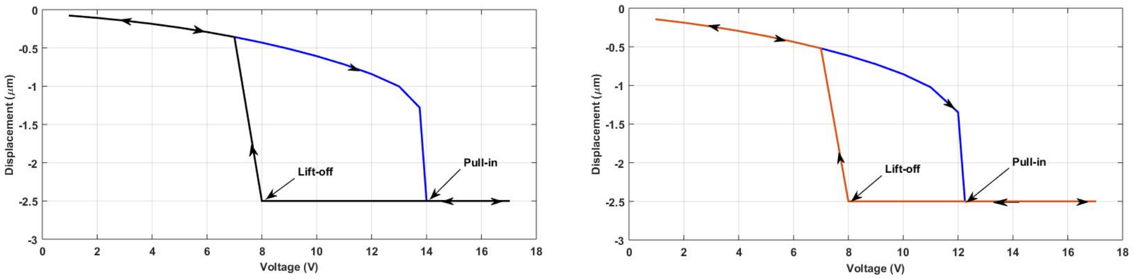

(a) Displacement Vs Voltage of shunt switch **(b)** Dispalcement Vs Voltage of series switch

Figure 4.5: Pull-in and lift-off voltage of SPST switches used in SP4T design.

Simulation results show that the actuating membrane of the series switch is pulled down at 13.75 V and that of shunt switch at 12 V. The design geometry is similar for both series and shunt switches except that the series switch membrane is slightly more stiff due to its shorter length compared to shunt switch membrane. Capacitive switches show hysteresis when switched ON and OFF. The switch requires peak voltage to pull the membrane down and then the resulting electric field is sufficient to maintain the down position. The applied voltage can then be brought down to reduce power consumption and when the voltage drops below the lift off voltage, the metal beam pulls up due to its elastic restoring force. Lift-off voltage of the designed series and shunt switches is found to be same and is 8 V. The voltage displacement curves for shunt and series switches of SP4T are shown in figures 4.5a and 4.5b respectively.

In dynamic response analysis, the pull-in time of the switching membrane is measured. Since MEMS switches operate by the mechanical actuation of membranes, the switching speed is in the range of a few tens to few hundreds of micro seconds where as FET/PIN devices switch in nanoseconds. It is known that the stiffer the membrane, the better will be the switching time. Simulation results presented in figure 4.6 and 4.7 show that the switching time of series and shunt switches are 7.59 μs and 7.68 μs respectively.

The build up of residual stress on the membrane is inherent during microfabrication and this affects stiffness of the membrane and thus pull-in. The fixed-fixed membrane geometry undergoes buckling under compressive stress and certain fabrication processes can be employed to prevent the occurrence of compressive stress (Yao *et al.* (1999)). This section discuss the effect of tensile stress on the actuating membrane. Tensile stress from 0 to 40 MPa was applied to the membrane and the effect

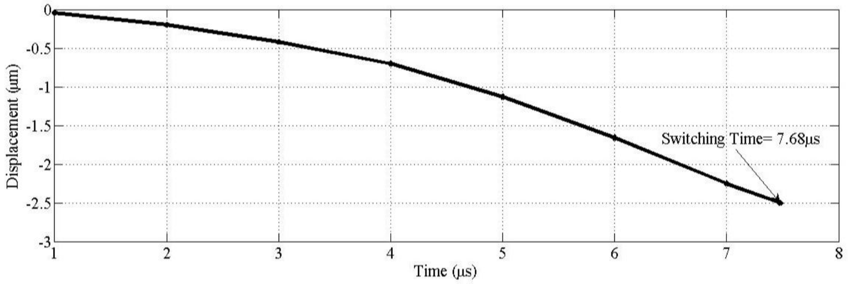

Figure 4.6: Switching time of shunt switch

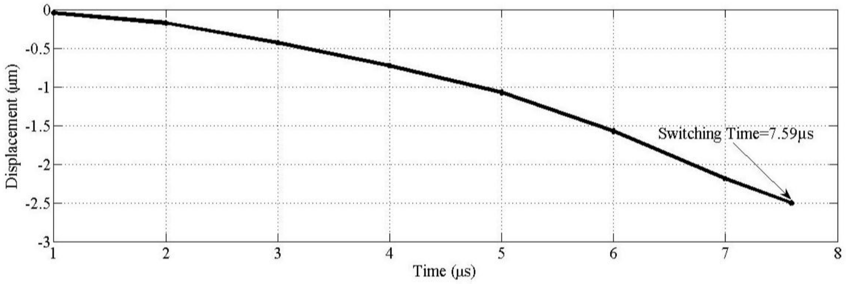

Figure 4.7: Switching time of series switch

is analyzed in CoventorWare. A plot of pull-in voltage variations with tensile stress is shown in Figure 4.8. It can be seen that the pull-in increases from 12 to 75 V as the tensile stress increases from 0 MPa/μm to 40 MPa/μm. The simulated parameters of the switches are presented in table 4.2.

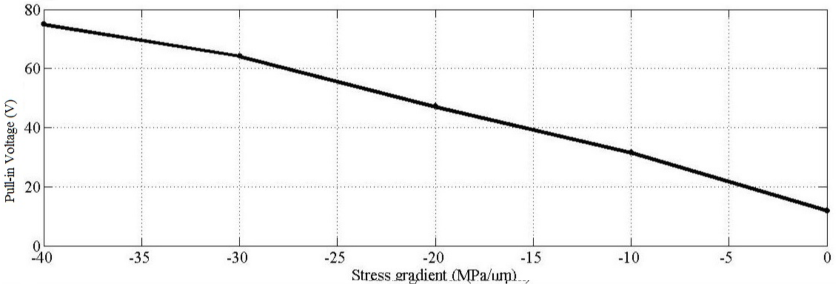

Figure 4.8: Pull-in voltage variation with residual stress.

4.4 Electromagnetic Design

RF MEMS SP4T switch 3-D model is built and simulated in ANSYS HFSS for X band performance. The shunt capacitive switch, positioned close to the output ports,

Table 4.2: Simulated parameters of the designed switch.

Parameter Name	Parameter Value (Series switch)	Parameter Value (Shunt switch)
Resonant Frequency	188.87 kHz	150.87 kHz
Capacitance-Down state (C_d)	-	3.186 pF
Capacitance-Up state (C_u)	-	16.90 fF
Capacitance ratio (C_d/C_u)	-	188.5
Pull-in Voltage	13.75 V	12 V
Lift-off Voltage	8 V	8 V
Pull-in Time	7.59 μs	7.68 μs

presents an up-state (unactuated) capacitance (C_u) of 16.90 fF and down-state (actuated) capacitance (C_d) of 3.186 pF. This large value of C_d/C_u shows high isolation in the actuated state.

4.4.1 RF Performance

RF characteristics of SP4T switch depends on the switching performance of the series and shunt SPST switches in the signal path leading to the output port and the length of high impedance lines, marked X and Y in figure 4.3a and figure 4.3b respectively. The proposed SP4T switch geometry given in figure 4.3a is chosen symmetric with respect to input port, (port 1). This is reflected in the S-parameter response given in figure 4.9. S_{n1} represents insertion loss at the n^{th} port when the SP4T switch is in ON state. Similarly, S_{n1} represents the isolation between n^{th} output port and input port when the SP4T switch is in OFF state. The insertion loss at output ports 2 & 3 is found to be -0.70 dB and that at ports 4 & 5 is -0.32 dB at 10 GHz. When the input RF signal is connected to only port 2, S_{21} represents insertion loss and S_{31}, S_{41} and S_{51} represents isolation. Isolation of -52 dB and -62 dB is observed for near and far ports in SP4T switches at 10 GHz. This is presented in figure 4.9. Figure 4.10 shows the S-parameters when input port is connected to port 4, and ports 2,3 and 5 are isolated from the input.

In multiport switch design, the electrical length of transmission line from input to output is optimized such that the reflections from output ports and discontinuities cancel each other resulting in reflection null or minimum return loss. Parametric analysis is performed to optimize the spacing between transmission lines (length X in figure 4.3a), position of the switches and spacing between them A mid-section

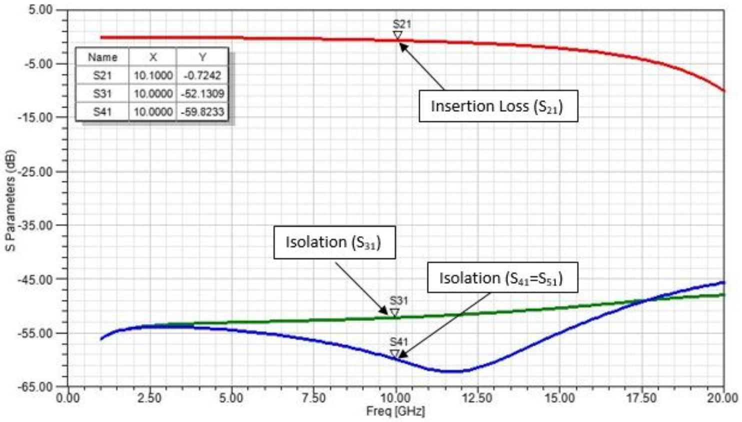

Name	X	Y
S21	10.1000	-0.7242
S31	10.0000	-52.1309
S41	10.0000	-59.8233

Figure 4.9: S parameters of SP4T with port 2 connected to input port 1

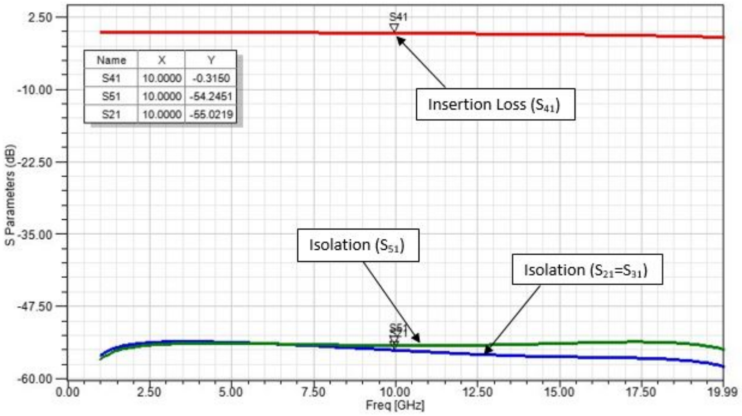

Name	X	Y
S41	10.0000	-0.3150
S51	10.0000	-54.2451
S21	10.0000	-55.0219

Figure 4.10: S parameters of SP4T with port 4 connected to input port 1

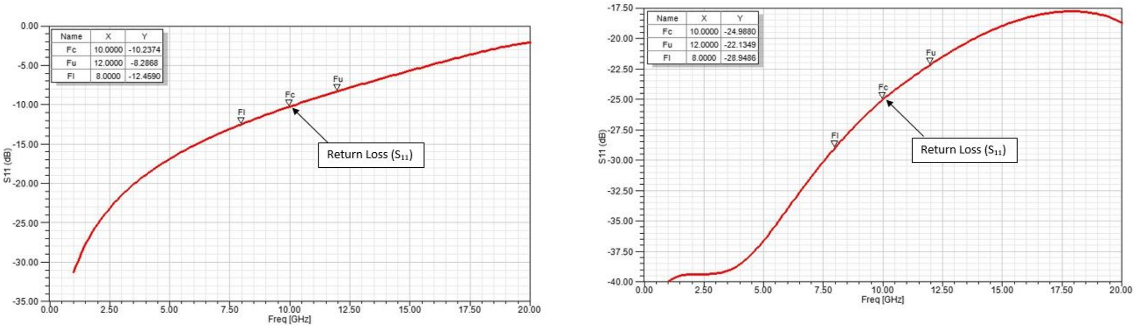

Name	X	Y
Fc	10.0000	-10.2374
Fu	12.0000	-8.2868
Fl	8.0000	-12.4590

Name	X	Y
Fc	10.0000	-24.9880
Fu	12.0000	-22.1349
Fl	8.0000	-28.9486

(a) S_{11} with 50 Ω mid-section line X

(b) S_{11} with spacing between the switches (Y) optimized

Figure 4.11: Return loss S_{11} with optimized X and Y lengths in fig. 4.3

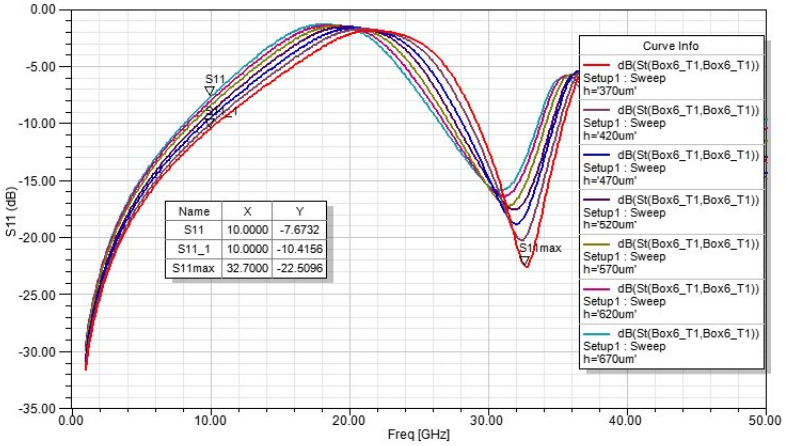

Name	X	Y
S11	10.0000	-7.6732
S11_1	10.0000	-10.4156
S11max	32.7000	-22.5096

Figure 4.12: Return loss S_{11} - Parametric analysis on X in fig. 4.3a

high impedance transmission line, 370 μm long, as shown in figure 4.3 connects the parallel signal lines to adjacent ports and this reduces the required electrical length for reflection null and minimum return loss. With 50 Ω midsection CPW transmission line of 700 μ, the return loss of -10 dB is observed at 10 GHz as is shown in Figure 4.11a. Simulation with high impedance line of 86 Ω shows that the same return loss of -10 dB at 10 GHz can be achieved with a line length of 370 μm. However, the best return loss of -23 dB is observed at 33 GHz for the same switch as shown in figure 4.12. S_{11} in the X band is further improved by optimizing the length (Y in figure 4.3b) of the high impedance line between the series and shunt switches and the results are shown in figure 4.13. It is seen from the results that the introduction of 258 μm long transmission line of impedance 86 Ω between the series and shunt switches improves the return loss (S_{11}) to -27.9 dB at 10 GHz. Figure 4.11b shows the return loss characteristics of SP4T. If the length of the high impedance line between the switch membranes alone is optimized for return loss, it is found that the return loss reduces to -24.9 dB.

4.5 Comparison with published results

Table 4.3 gives a comparison of the switch results presented in this work with the published results. All devices discussed in this table have low insertion loss but high pull-in voltage. Also, switches by Zareie and Rebeiz (2014), Lin (2016), Dey *et al.* (2016) have lower isolation. It can be seen from the table that the device designed in

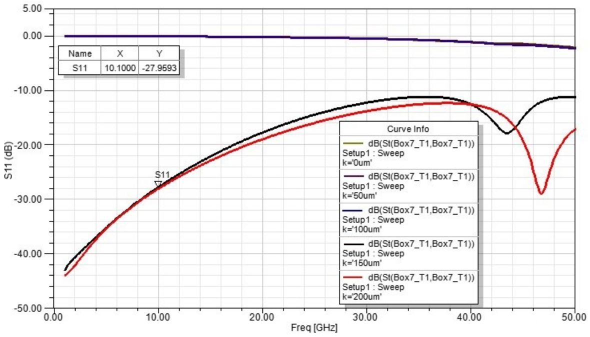

Figure 4.13: Return loss S_{11} - Parametric analysis on Y in fig 4.3b

this work have low insertion loss, high isolation and low pull-in voltage.

Table 4.3: Comparison of published SP4T RF-MEMS Switches with this work

	Frequency	Insertion (dB)	Isolation (dB)	Pull-in Voltage	Type of SPST switch used
Roy et. al., 2010	DC to 8 GHz	0.23 dB	53 dB	-	CPW shunt switch
Zareie et.al., 2014	X band	0.8 dB	20 dB	50 V	Metal contact switch
Yang et. al., 2014	DC to 50 GHz	1-2 dB at 8-50 GHz	60 dB at 32 GHz	90 V	Radial series and shunt SP4T switch
J. Lin, 2016	DC to 5 GHz	0.8 dB	24 dB	35-45 V	Shunt configured resistive switch
Dey et. al., 2016	X band	0.4 dB	20 dB	-	Radial series and shunt SP4T switch
This work	X band	0.72 dB	52.13 dB	13.75 V	Series shunt switch

4.6 Conclusion

This work presents a single pole four throw switch, where low loss value has been tuned to X band. A bridge structure anchored across the signal lines and attached to the ground planes on both sides has been used to implement the shunt switch structure. Series switches are anchored to the substrate instead of ground planes. In both the switches separate actuating electrode is placed on both sides of the signal line for electrostatic actuation. The designed switch shows an insertion loss of -0.70 dB for port 2 & 3 and -0.32 dB for port 4 & 5 at 10 GHz. Isolation of -52 dB and -62 dB is observed for near and far ports in SP4T switches at 10 GHz. The bridge structure shows a pull-in voltage of 13.75 V and switching time of 7.59 μs for series switch, and a pull-in voltage of 12 V and switching time of 7.68 μs for shunt switch. This SP4T switch has an area of about 1600 μm x 1106 μm = 1.76 mm^2. Further, these switches will be suitable in applications such as tunable MEMS filters and phase shifters.

Chapter 5

DISTRIBUTED TRUE-TIME-DELAY TUNABLE RF MEMS BASED PHASE SHIFTER

5.1 Introduction

Phase shifters play a vital role in the communication industry, mainly in radar and phased array antennae. Based on the operation phase shifters can be classified as analog or. In analog type the phase will be varied between 0° and 360°. In digital phase shifters discrete phase shifts can be achieved by using switches. Phase shifters can also be categorized as constant phase versus frequency and linear phase versus frequency. Constant phase designs are used in signal processing applications like radar and communication systems, and the latter is used as true time delay networks in phased array applications. Phase shifters can have reciprocal or non reciprocal characteristics. Reciprocal phase shifters have the same phase at the input and output ports. Whereas in nonreciprocal systems the phase will be different.Another categorization is based on tuning: mechanical and electronic. Before the advent of electronic phase shifters, mechanical phase shifters were being used for fixed and variable phase shifts. Mechanical phase shifters were generally constructed using metallic waveguides or coaxial line and were also using DC motors for phase shift control. They exhibited robust construction, large space consumption, and subject to mechanical wear and tear. Eventually mechanical methods were replaced by electronic components such as PIN diodes, FET switches, and Ferrite components. Electronic phase shifters have notable advantages over mechanical phase shifters in terms of volume requirements and phase shift accuracy.

5.2 Overview on Electronic Phase Shifters

5.2.1 PIN Diode Based Phase Shifter

PIN diodes are used as electronic switches in phase shifters, for switching bias current from forward to reverse bias mode (Chakraborty and Gupta (2017)). The ON-OFF state of diode will be controlled by the intrinsic region. High impedance will be offered under reverse bias and lower impedance in forward bias. Therefor phase shift is the result of switching between transmission line of two different path lengths based on the bias state of the PIN diode. Phase shift is a function of path length and β, the propagation constant.

PIN diode based switches are commercially available at low cost. These have a switching time of $200 - 800$ ns with a DC power consumption of $5 - 100$ mW and operates from L- to Q-band (Chakraborty and Gupta (2017)).

5.2.2 FET Based Phase Shifters

Similar to PIN diode based phase shifters, Field Effect Transistor (FET) phase shifters are popular because of their fast switching time and low power consumption (Maruhashi *et al.* (2000)). Ferrite phase shifters offer low DC power consumption and higher switching speed (μs) but they have some limitations such as higher cost, fabrication complexity and frequency limitations. These are faster than PIN diodes with $1-100$ ns switching speeds and a lower power consumption (Chakraborty and Gupta (2017)).

5.2.3 MMIC Based Phase Shifters

Monolithic microwave integrated circuits uses MOS, an excellent switching device at low frequencies. MOS switches do not require a negative control voltage and can be implemented with digital controllers in a chip. A silicon MOS switch still exhibits a high insertion loss at high-frequency ranges due to its high on resistance and substrate conductance (Kang *et al.* (2006)). This technology reduces loss incurred by wire bound interconnections since both active and passive components are fabricated on the same substrate (Chakraborty and Gupta (2017)). However fabrication complexity, higher expenses, and frequency limitations limits its application in the telecommunication field.

5.2.4 Ferroelectric Phase Shifters

Ferroelectric phase shifters uses materials with ferroelectric properties. Barium-strontium-titanate (BST) is a ferroelectric material that has an intrinsic tunable dielectric constant that can be controlled by a DC bias. These devices can be continuously tuned with low loss and high power handling capacity, and also exhibit high tuning speed. BST tunable devices have problems such as high loss, poor crystalline quality, expensive fabrication techniques, and requirement of high DC bias (Zhao *et al.* (2007)).

5.2.5 MEMS Phase Shifters

Solid state phase shifters such as PIN diodes and FET switches are inexpensive and are compact but they have poor power handling capability and significant insertion loss at high frequency. RF MEMS based devices exhibit lossless performance up to terahertz range. MEMS technology shows high linearity with wide band performance and high power handling capacity. MEMS have enhanced isolation and low parasitic effects, due to capacitive contacts. 100 Billion cycles is the life span of MEMS capacitive switches. RF MEMS phase shifters are two port devices in which phase shift is obtained by using MEMS based switches, switched capacitors or varactors.

5.3 MEMS Phase Shifters

5.3.1 Phase Shifter Topologies

Several approaches are available for implementing phase shifters : Switched Line phase shifters, Loaded line phase shifters, Reflection type phase shifters and Distributed line phase shifters (Rebeiz (2004)). Most commonly used phase shifter is DMTL (Distributed MEMS Transmission Line) topology.

5.3.1.1 Switched Line Phase Shifters

Switched line type phase shifter is one of the simplest to implement. Desired phase shift is achieved by switching between two transmission lines of different lengths. This can be achieved by using either series or shunt MEMS switch. Figure 5.1 shows the layout of an RF MEMS switched-line phase shifter using MEMS series switches. The phase shifter shown in the layout is a 3-bit phase shifter, with three separate transmission lines connected through series switches. Each section provides a phase shift of 45°, 90° or 180°. It is possible to switch between delay lines and reference lines, so proper switching gives desired phase shift.

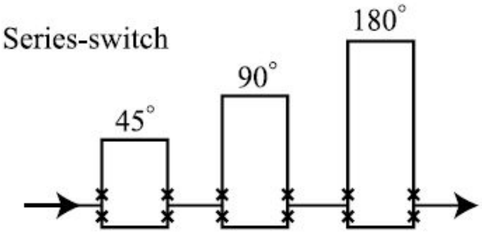

Figure 5.1: Switched-line phase shifter configuration employing series switch.

Figure 5.2 shows the layout of an RF MEMS switched-line phase shifter using MEMS shunt switches. Similar to the previous structure, this too is a 3-bit phase shifter and the desired phase shift is achieved by shunt switches. Switched-line phase shifters employing SPDT switches require larger substrate area. This drawback can be reduced to a certain extent by using SP4T switches, due to the reduction in substrate area.

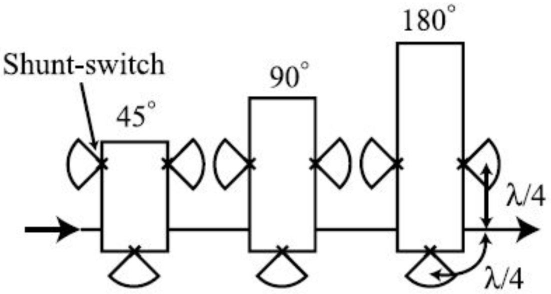

Figure 5.2: Switched-line phase shifter configuration employing shunt switch.

5.3.1.2 Loaded Line Phase Shifters

In this type of phase shifter the phase shift is achieved by loading the transmission line with different reactive loads, capacitive or inductive. To retain the input and output impedance 50 Ω, the central t-line acts as a matching network. Figure 5.3 shows the schematic of a loaded line phase shifter, where Z_c is the characteristic impedance, and θ is the electrical length of the transmission line. Z_1 and Z_2 represent the loaded-line impedances.

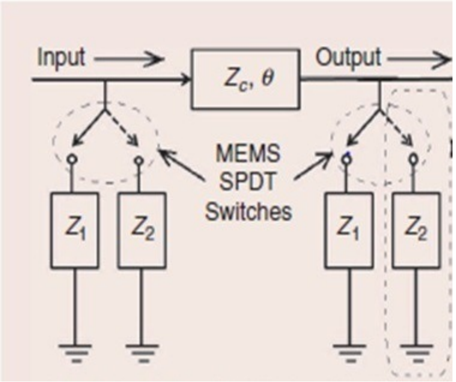

Figure 5.3: Basic schematic of the loaded-line phase shifter (Chakraborty and Gupta (2017))

In this phase shifter the impedances are selected by employing series or shunt MEMS switches. The phase shift is controlled by varying the value of load impedance. Phase lag can be obtained by using capacitive impedance and phase lead by using inductive impedance. Open t-line stubs results in capacitive impedance, whereas shorted t-line stubs create inductive impedance. Varying the length of shorted stub results in phase shift, open ended stubs results in constant phase shift. Considering a loss-less transmission line matched with the loads, the phase shift ϕ can be calculated from the following equations:

$$B_1 = Y_0 \left[\frac{cos\theta}{cos\Delta\phi/2} - tan\Delta\phi/2 \right] \tag{5.1}$$

$$B_2 = Y_0 \left[\frac{cos\theta}{cos\Delta\phi/2} + tan\Delta\phi/2 \right] \tag{5.2}$$

$$Z_c = Z_0 \frac{cos(\Delta\phi/2)}{sin\theta} \tag{5.3}$$

where Y_0 denotes the admittance of the input/output ports, B_1 and B_2 are the switched susceptances, Z_c is the characteristic impedance, and θ is the electrical length of transmission line. For loaded-line phase shifters better results are obtained for small phase delays. To get higher phase shifts these small netorks should be cascaded. It's simplicity, low loss and easy designing are major advantages. Also, phase shift versus frequency plot of loaded-line phase shifter is flatter than that of switched line phase shifter.

5.3.1.3 Reflection Type Phase Shifters

Couplers are one of the major components in reflection type topology and there are phase shifters using 3-dB couplers or Lange couplers. Figure 5.4 shows a reflection type phase shifter using 3-dB coupler implemented using MEMS switches. A narrow bandwidth output can be obtained from this kind of n-bit design. To obtain particular phase shift the coupler should be terminated reactively with specific reactance. Larger values of phase shift can be achieved by connecting different sections. The input RF signal will be reflected by different loads connected at the output port resulting in a differential phase shift. Implementation of couplers require larger area so it is a design constraint. As shown in the figure reflection type phase shifter can be implemented using MEMS shunt or series switch. In shunt switch implementation the phase delay

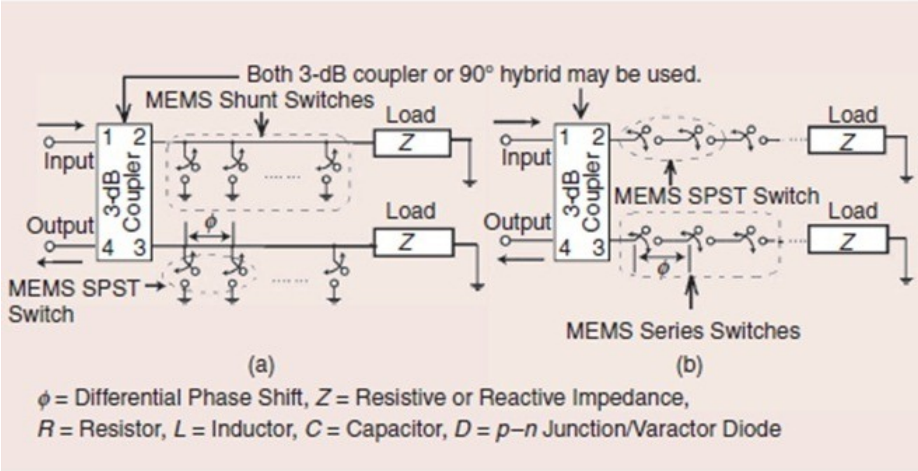

Figure 5.4: Reflection type phase shifter with (a) shunt switches and (b) series switches (Chakraborty and Gupta (2017))

offered in up state is given by,

$$\phi_{shunt} = -tan^{-1}\left(\frac{\omega C_u Z_0}{2}\right) \simeq -\left(\frac{\omega C_u Z_0}{2}\right) \qquad \left(\frac{\omega C_u Z_0}{2} \ll 1\right) \tag{5.4}$$

and in down state by,

$$\phi_{shunt} = 180^\circ + tan^{-1}\left(\frac{2}{\omega C_d Z_0}\right) \simeq \quad \pi + \left(\frac{2}{\omega C_d Z_0}\right) \qquad (\omega C_d Z_0 \gg 2) \tag{5.5}$$

The phase shift for series switch implementation in up state is given by,

$$\phi_{series} = tan^{-1}\left(\omega C_u Z_0\right) \simeq -2\omega C_u Z_0 \qquad (2\omega C_u Z_0 \ll 1) \tag{5.6}$$

In the down state position of series switch implementation the phase delay will be equal to the delay between the t-line and the beam's open ends.

5.3.1.4 Distributed MEMS Transmission Line (DMTL) Phase Shifters

Most popular, high figure of merit and low insertion loss phase shifter is the Distributed MEMS Transmission Line (DMTL) phase shifter. In this type of phase shifter the phase shift is realized by periodically loading the transmission line using switches or varactors. These switches can be MEMS shunt or series switches which are anchored at ground terminals. A periodic arrangement of switches results in a slow wave structure, which offers smaller substrate area compared to other topologies. The usage of several capacitive shunt switches reduce the reflection and improve the isolation (Muldavin and Rebeiz (2000*b*)). When the applied bias voltage is less than the pull-in voltage (V_p) of the structure loaded with MEMS bridges, it acts as a phase shifter. Figure shows a CPW transmission line periodically loaded using MEMS capacitive bridges with a spacing of $5\mu m$ and the corresponding equivalent circuit network. Each beam is modeled as a series RLC circuit with variable capacitance.

When a variable bias votage less than pull-in voltage is applied, then the height between MEMS beam and CPW center conductor varies resulting in a variable capacitance. This change in capacitance causes a variation in phase velocity and thereby introducing a phase shift.

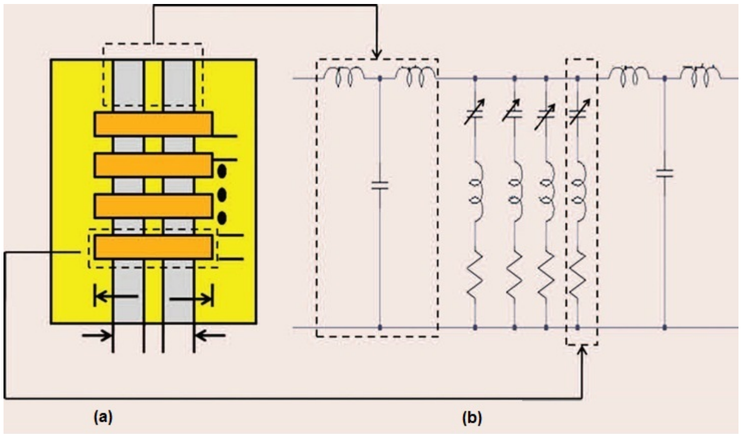

Figure 5.5: (a) DMTL phase shifter (b) Equivalent circuit network of DMTL phase shifter

5.4 Literature Review

A brief review of MEMS based phase shifters is carried out in this section. Rebeiz *et al.* (2002) and Chakraborty and Gupta (2017) lists four different topologies of phase shifters namely, switched line, loaded line, reflection and DMTL phase shifters. The simplest among them is the switched line phase shifter, which introduces the desired phase shift by switching between between unequal sections of transmission line.

Pillans *et al.* (1999) built a Ka-band phase shifter with an insertion loss of 2.25 dB and a return loss better than 13 dB using microstrip based switched line topology. It is a 4-bit device with phase error less than 13°. Hacker *et al.* (2003) implemented a true time delay switched line network having 12 metal-to-metal MEMS switches on GaAs substrate. It shows an average insertion loss of 2.2 dB in Ka-band. Tan *et al.* (2003) fabricated a 2- and 4- bit, X- to Ku- band phase shifter using SP4T switches. At 18 GHz an insertion loss of 1.1 dB was observed. Higher losses than expected occured in this design due to the increased switch resistance. A 6-bit low loss phase shifter for 1-6 GHz using 10 watt MEMS switch was reported in Lampen *et al.* (2010). Dey and Koul (2015) presents a 5-bit phase shifter fabricated by cascading a 1- and 2-bit phase shifters using SPDT and SP4T swithes. An average insertion loss of 2.65 dB in 13-18 GHz band and a return loss better than 22 dB was reported.

Bakri-Kassem *et al.* (2014) reports a 8 latching SPDT based RF MEMS phase shifter on CPW transmission lines on a high resistive silicon substrate. The design handles high power and works at 80°C. Switched line phase shifters are more complex to realize. They suffer from large substrate area utilization and the insertion loss is high compared to the length of transmission line employed.

An RF MEMS 3-bit phase shifter working at 34 GHz on silicon substrate is reported in Siegel *et al.* (2007). It uses different techniques to achieve the phase shift. A dual state microstrip line and a loaded line is used for realization of phase shift. A mean insertion loss of 2.2dB and a 13.25° phase shift is reported at 34 GHz.

Malczewski *et al.* (1999) developed a phase shifter based on reflection topology using lange couplers on silicon, which resulted in an average insertion loss of 1.4 dB with return loss greater than 11 dB. But couplers result in 60% of insertion loss. Hence, off chip couplers needed to be integrated with silicon substrate.

Barker and Rebeiz (1998) introdued the first DMTL TTD phase shifter using MEMS capacitive switches on CPW transmission lines. It was fabricated on silicon substrate resulting in 0-60 GHz phase shifter with 2 dB loss giving 118° phase shift at 60 GHz. MEMS bridges had a pull down voltage of 10-23 V. This was an analog phase shifter in which phase shift is achieved by capacitive loading. In Liu *et al.* (2000) a distributed 3-bit MEMS phase shifter was implemented using MIM capacitors and Silicon Nitrate is used as dielectric. This has an insertion loss of 1.5 dB at 26 GHz. Wave reflection occurred due to mismatch between consecutive sections and deteriorate losses leading to poor performance over 30 GHz.

Borgioli *et al.* (2000) presents a 1-bit K/Ka-band phase shifter with MEMS capacitors resulting in 180° phase shift with 1.17 dB insertion loss at 25 GHz. Hayden and Rebeiz (2000*a*) reports a 2-bit phase shifter operating in X-band, based on DMTL loaded with MEMS bridges and MIM capacitors. To achieve excellent results high Q MIM capacitors are used. Hayden and Rebeiz (2000*b*) presents a wideband DMTL phase shifter using MIM capacitors and MEMS bridges on CPW transmission line. It gives a phase shift of 180°/dB of insertion loss at 8-10 GHz and the return loss was greater than -15 dB. In Barker and Rebeiz (2000), optimization and design of MEMS phase shifters at U- and W-band is presented. U-band and W-band designs resulted in a phase shift of 70°/dB at 40 GHz and 75-110 GHz respectively. In Hayden and Rebeiz (2003), a DMTL phase shifter on quartz substrate was developed for X- and Ka-band operation. Hiqh Q MAM capacitors along with MEMS switches were used. They reported an insertion loss of 1.5 dB and reflection coefficient better than 11.5 dB. Hung *et al.* (2004) presented a 75-110 GHz 2- and 3-bit phase shifter on a glass substrate with a 93°/dB-100°/dB figure of merit over 75-110 GHz. In this paper a high Q-MAM capacitor is built between the crossover of MEMS bridge and CPW ground plane. A MIM capacitor is placed between 90° and 180° sections. In Du *et al.* (2010) a unit cell of MAM capacitor is used. This had a return loss below 20dB and insertion loss of 0.08dB at 10 GHz for the unit cell. Phase deviation of unit cell is 0.829°. A 5-bit phase shifter is obtained by cascading these unit cells, which has an overall insertion loss of 1.49 dB and average phase deviation of 1.49°.

In Nataraj and Porkumaran (2012), instead of conventional coplanar waveguide a step tapered CPW is used. The transmission line is periodically loaded with MEMS switches and an analog control voltage is applied to the center conductor. It resulted in a phase shift of 174° with an insertion loss less than -1dB at 35 GHz. Unlu *et al.* (2013) presented a frequency re-configurable phase shifter. It is based on a triple stub circuit topology which contains three stubs connected by two transmission lines. Insertion phase is controlled by varying electrical length of stubs and connecting transmission lines. it had a phase error of 1.6°, 3.7°, 4.7°, insertion loss of 3.1 dB, 5 dB and 8.2 dB and return loss of 19.3 dB, 15.8 dB and 13.7 dB at 15, 30, and 40 GHz respectively.

A novel technology using carbon nanotube was introduced in Generalov *et al.* (2015). The phase shifter is based on a high impedance structure with CNT membrane MEMS, which is integrated on to dielectric rod waveguide. It has a theoretical phase shift of 260° with 7 V bias voltage. In Ramli and Arslan (2017) a distributed CPW phase shifter for S-band is designed. Insertion loss reduction was achieved by using high resistivity silicon substrate and aluminium center conductor. Large MIM capacitor is used between two bits to separate DC actuation voltage during operation. Size of phase shifter is reduced by using 60° mitering. It reported an average insertion loss of 1.69 dB at 2.45 GHz.

Verona *et al.* (2014) presented a distributed MEMS phase shifter based on tunable shielded CPW for millimeter wave applications, which had a phase shift of 25.1° with an insertion loss of 0.7 dB at 60 GHz under 60 V bias voltage. In Bovadilla *et al.* (2017), a 3-bit phase shifter using distributed MEMS and slow-wave CPW (S-CPW) is proposed. A shielding layer is used as a distributed capacitance.

5.5 Design of MEMS Phase Shifters

5.5.1 Transmission Line Characteristics

The equivalent circuit representation of a transmission line in TEM mode is as shown in the figure 5.6. R in Ω/m represents the linear resistance offered by the conductors in transmission line. L in H/m is the linear inductance and C in F/m is the linear capacitance between the t-lines. G in S/m is the linear conductance due to the leakage through dielectric. The characteristic impedance Z_c is given by,

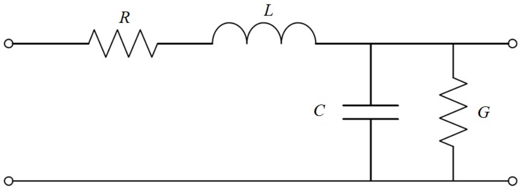

Figure 5.6: Telegraph Model

$$Z_c = \sqrt{\frac{R + j\omega L}{G + j\omega C}} \tag{5.7}$$

and the propagation constant γ can be calculated as

$$\gamma = \sqrt{(R + j\omega L)(G + j\omega C)} \tag{5.8}$$

Propagation constant is represented as

$$\gamma = \alpha + j\beta \tag{5.9}$$

were α is the attenuation constant in dB/m and β is the propagation constant in rad/m. The quality factor is

$$Q = \frac{\beta}{2\alpha} \tag{5.10}$$

Under lossless condition $R = 0$ and $G = 0$, therefore the above equations reduces to,

$$\begin{aligned} Z_c &= \sqrt{L/C} && (5.11) \\ \gamma &= j\omega\sqrt{LC} && (5.12) \end{aligned}$$

From these equations propagation constant β can be calculated as

$$\beta = \omega\sqrt{LC} = \frac{\omega}{\nu_\phi} \tag{5.13}$$

where,

$$\nu_\phi = \frac{\omega}{\beta} = \frac{1}{\sqrt{LC}} \tag{5.14}$$

is the phase velocity of the transmission line and phase $\phi = \beta l$, were l is the electrical length of t-line.

5.6 Slow Wave Coplanar Waveguide

Coplanar Waveguide (CPW) shown in figure 5.7 provides wider wavelength as the distance between signal line and ground increases. But this can not prevent the substrate losses, so a floating metallic shield is used to reduce the penetration of the electric field into the substrate as shown in figure 5.8. In this work the phase shifter is designed on an S-CPW (Slow Wave Coplanar Waveguide) transmission line, since they show higher performance in silicon technology. Here the floating shield technique is used to reduce the substrate loss.

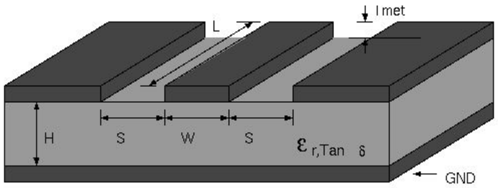

Figure 5.7: CPW transmission line

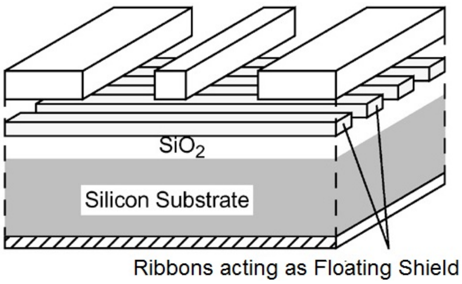

Figure 5.8: S-CPW transmission line

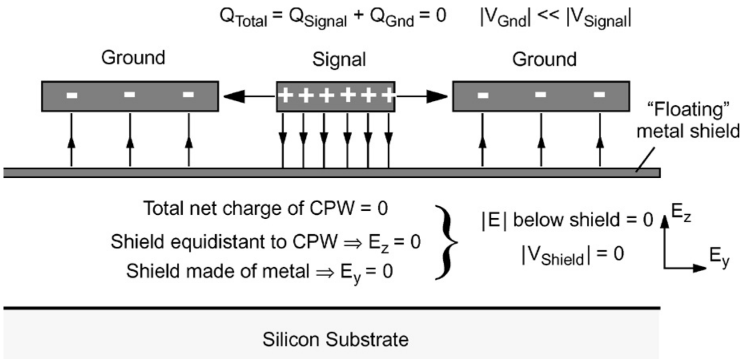

Figure 5.9: Transmission line with floating shield (Cheung and Long (2006))

.

The floating shield used is metal. Thus, with respect to the CPW, the net voltage on the shield will be zero. So it acts as a perfect shield in between CPW and substrate thereby reducing substrate losses, as shown in figure 5.9 (Cheung and Long (2006)).

The S-CPW concept was introduced for the reduction of signal speed and hence to reduce transmission line length. This can be explained in a circuit perspective, if the high and low impedance sections are shorter compared to the wavelength, then it is possible to approximate each section into a lumped L-C model, where L and C are line inductance and capacitance respectively. The high impedance section has a high inductance and low capacitance whereas low impedance section has higher capacitance and low inductance. When these are cascaded together, the series inductance will dominate high impedance section and low impedance section will be dominated by capacitance. This results in an increase in both L and C, leading to increased delay of signal and results in slow wave phenomenon.

5.7 Tuning of S-CPW

The reflections in the transmission line can be reduced by using several shunt capacitive switches instead of a single switch (Muldavin and Rebeiz (2000*b*)). Using several shunt switches the phase shifter can be tuned. The S-CPW with several floating shields can be represented by the equivalent circuit shown in figure 5.10. The floating shield strip (ribbon) is represented as the variable capacitance, as the capacitance varies with electrostatic actuation. In 5.10, C_b represents the variable capacitance offered by the bridges/ribbons, L and C are inductance and capacitance per unit length of unloaded transmission line. Considering the high inductive impedance, the trans-

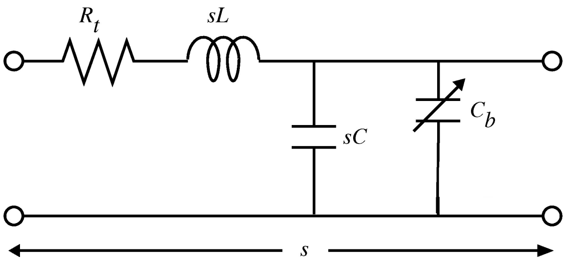

Figure 5.10: Lumped model of one section of loaded transmission line (Hayden and Rebeiz (2003))

mission line resistance can be neglected. From this model, the loaded transmission line impedance will be,

$$Z_l = \sqrt{\frac{sL}{sC + C_b}}\sqrt{1 - \left(\frac{\omega}{\omega_B}\right)^2} \tag{5.15}$$

where ω_B is the Bragg frequency

$$\omega_B = \frac{2}{\sqrt{sL(sC + C_b)}} \tag{5.16}$$

and spacing between the ribbons,

$$s = \frac{Z_u}{\pi f_B \sqrt{L(C_r L - (C_r - 1)C Z_u^2)}} \tag{5.17}$$

The phase velocity can be represented as (Barker and Rebeiz (2000))

$$\nu = \frac{s}{\sqrt{sL(sC + C_b)(1 + \frac{\omega^2}{6\omega_B^2} + ...)}} \tag{5.18}$$

C_{b0} zero bias bridge capacitance

$$C_{b0} = s(\frac{L}{Z_u^2} - C) \tag{5.19}$$

Bridge capacitance

$$C_b = C_r.C_{b0} \tag{5.20}$$

Phase shift is

$$\Delta\phi = \beta_1 - \beta_2 = \omega(\frac{1}{\upsilon_1} - \frac{1}{\upsilon_2}) \tag{5.21}$$

$$\Delta\phi = \frac{swZ_\circ\sqrt{\varepsilon}_{r,eff}}{c}\left(\frac{1}{Z_u} - \frac{1}{Z_d}\right) rad/m \tag{5.22}$$

5.8 Mechanical Modeling of Bridges

In this phase shifter the t-line is periodically loaded with MEMS capacitive shunt beams called ribbons. Figure 5.8 shows S-CPW transmission line without loading.

The mechanical modeling of ribbons can be done by studying the spring constant (k) (Rebeiz (2004)).

$$k = \frac{32Et_r^3w_r}{L_r^3} + \frac{8\sigma(1-\nu)t_rw_r}{L_r}(N/m) \tag{5.23}$$

where E is the Youngs modulus of bridge material, $L_r,\ t_r,\ w_r$ are the length, thickness and width of the ribbons (bridges) respectively, σ is the residual stress on the ribbon and ν is the Poissons ratio of the bridge material. Force on the ribbons due to applied bias votage (Barker and Rebeiz (1998)) is,

$$F = \frac{\varepsilon_\circ Ww_r}{2g^2}V_{bias}^2(N) \tag{5.24}$$

where ε_0 is the free space permittivity, W is the width of CPW center conductor, g is the bridge height and V_{bias} is the applied voltage.

Pull-in voltage is given by

$$V_p = \sqrt{\frac{8k}{27\varepsilon_0Ww_r}g_\circ^3}(V) \tag{5.25}$$

where g_0 is the zero bias bridge height.

5.9 Modeling of Phase Shifter

The cross section of the phase shifter geometry of figure 5.8 with and without the actuation of shunt membranes is shown in figure 5.11. The tunability in phase shift is obtained by the controlled capacitive loading of the transmission line by the DC actuation of various sets of metalic shunt memebranes. The proposed tunable MEMS phase shifter 3-D model, given in figure 5.12, is designed and simulated in ANSYS HFSS to assess the RF performance. The electromechanical simulation of the shunt metallic membranes is performed in FEM solver CoventorWare.

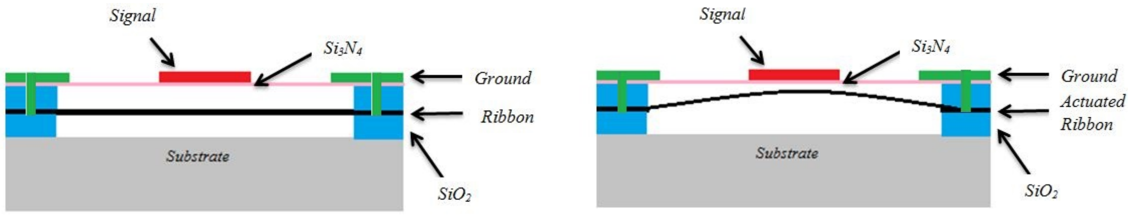

(a) Shunt ribbons unactuated

(b) Shunt ribbons actuated

Figure 5.11: S-CPW Phase shifter cross-section

In the proposed design 5-sets of metallic membranes or ribbons, each set having variable number of ribbons, are used for achieving tunability in phase shift.

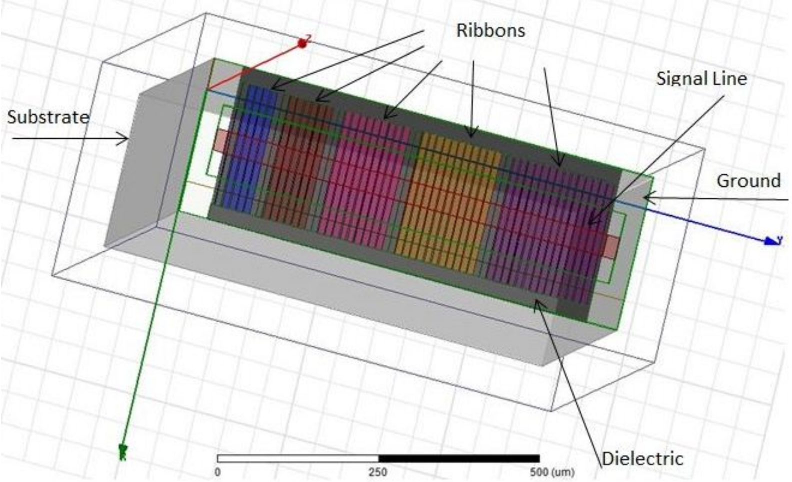

Figure 5.12: 3-D model of of S-CPW phase shifter

Set	No. of **Ribbons**
Set 1	5
Set 2	7
Set 3	10
Set 4	12
Set 5	15

Table 5.1: No. of Ribbons

Table 5.1 lists the sets of ribbons and number of ribbons in each set as shown in figure 5.12. The proposed model is built and simulated on a 500 μm silicon substrate. The CPW conductors are made of gold to reduce resistive losses. CPW dimensions for 50 Ω impedance are 39.5/35/39.5 (G/W/G) and conductor thickness is 2 μm. The dimension of each of the shunt ribbon is 200*10* 1 (μm). A thin dielectric layer (0.1 μm) of Si_3N_4 is deposited beneath signal line. The dielectric layer enables effective capacitive loading of the transmission line by the actuating membranes. This capacitance variation alters the phase velocity of the propagating wave leading to phase shift

The Distributed MEMS Transmission Line phase shifter given in figure 5.13a is loaded by variable sets of ribbons. The phase characteristics, insertion loss (S_{21}) and return loss (S_{11}) for the DMTL phase shifter are shown in figure 5.13b and 5.14

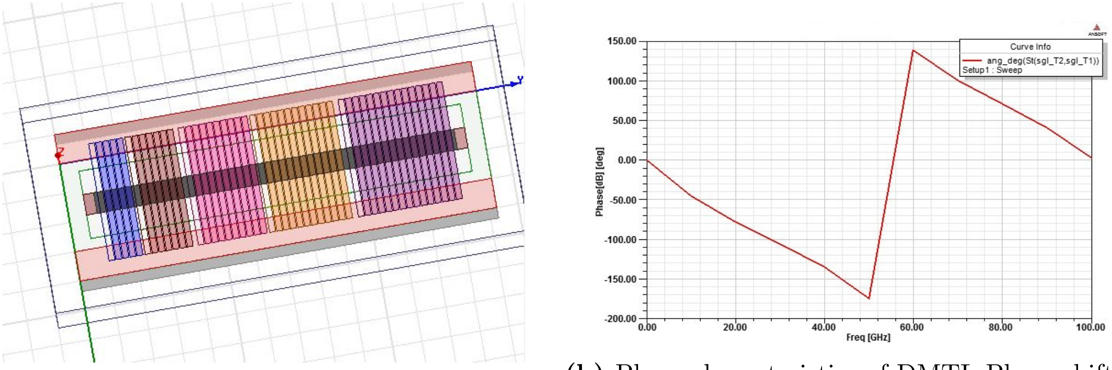

(a) DMTL Phase shifter

(b) Phase characteristics of DMTL Phase shifter

Figure 5.13: DMTL Phase shifter with variable sets of ribbons

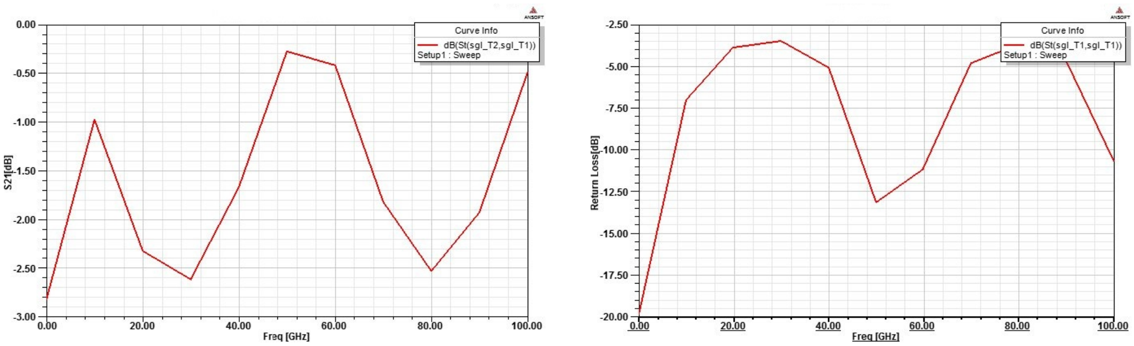

(a) Insertion Loss S_{21} of DMTL Phase shifter

(b) Return Loss S_{11} of DMTL Phase shifter

Figure 5.14: S-Parameters of DMTL Phase shifters

The slow wave coplanar waveguide (S-CPW) phase shifter with identical sets of metallic ribbons shunting the line is shown in figure 5.15a along with their phase characteristics in figure 5.15b. The S-Parameters of the phase shifter is shown in figure 5.16. Parametric analysis is performed to optimize the spacing between the individual ribbons and that between sets of ribbons to improve the RF performance. From the parametric results given in figure 5.17, it is seen that at 40 GHz the phaseshift varies with spacing between ribbons, from 60° at 1 μm to 120° at 10 μm. The corresponding insertion loss is better than 0.1 dB and return loss better than 15 dB at 40 GHz.

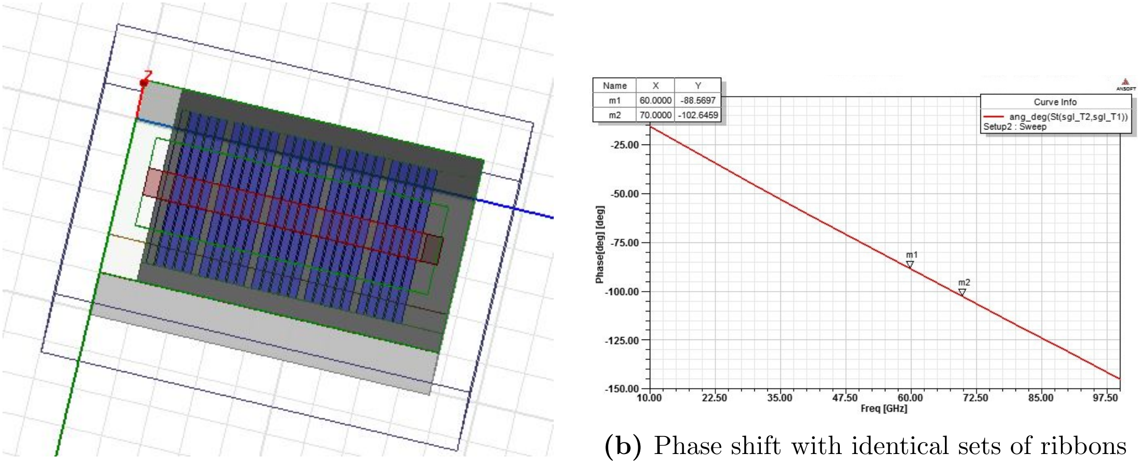

(a) S-CPW Phase Shifter with identical sets of ribbons

(b) Phase shift with identical sets of ribbons

Figure 5.15: S-CPW RF MEMS Phase shifter

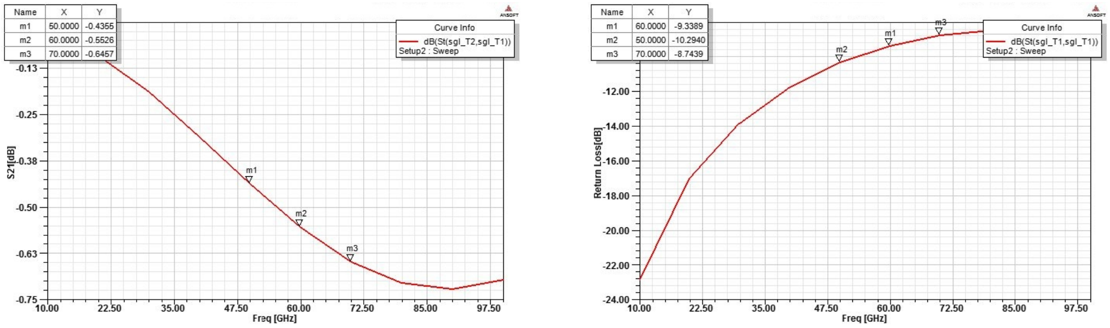

(a) Loss S_{21} with identical sets of ribbons

(b) Return loss with identical sets of ribbons

Figure 5.16: S-Parameters - S-CPW Phase Shifter

To optimize the phase characteristics and RF performance, another round of parametric analysis is conducted with spacing between sets of ribbon as parameter. With the spacing between ribbon fixed at 2 μm, the new parameter is varied from 10 to 20 μm and the results are analysed. At 40 GHz, the phase varies from 104° to 112° as the new parameter (spacing between sets of ribbons) varied from 10 to 20 μm. The new parameter is fixed at 10 μm considering the maximum phase shift of 180° at 70 GHz. Corresponding S_{21} and S_{11} are better than 0.69 dB and 8 dB respectively. It can be seen that the phase shift characterstics and S-parametrs are suitable for applications in Ku and K bands.

The electro-mechanical model of the actuating ribbons is simulated in FEM solver CoventorWare and the results are analysed to optimize the pull-in voltage and to

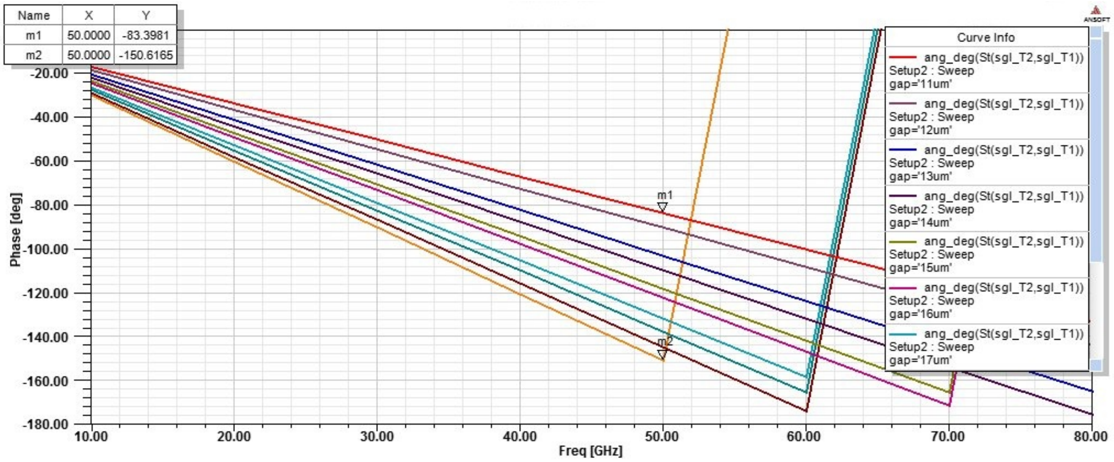

Figure 5.17: Phase at different gaps between ribbons

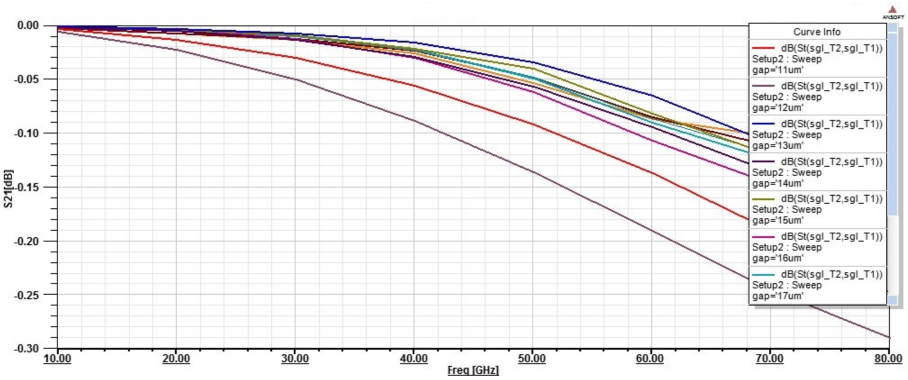

Figure 5.18: S_{21} with varying spacing between ribbons.

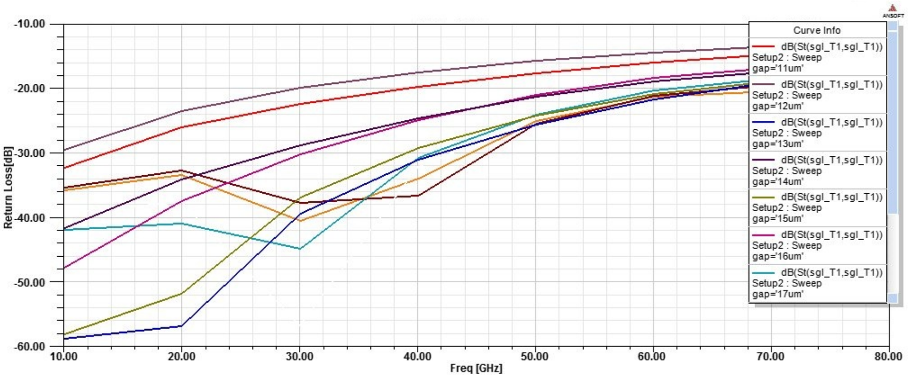

Figure 5.19: S_{11} with varying spacing between ribbons.

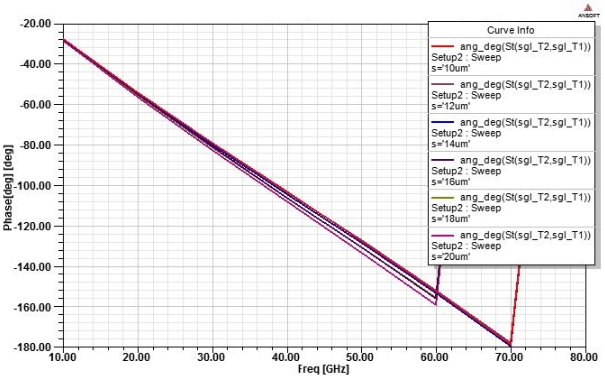

Figure 5.20: Phase at different gap between sets of ribbons.

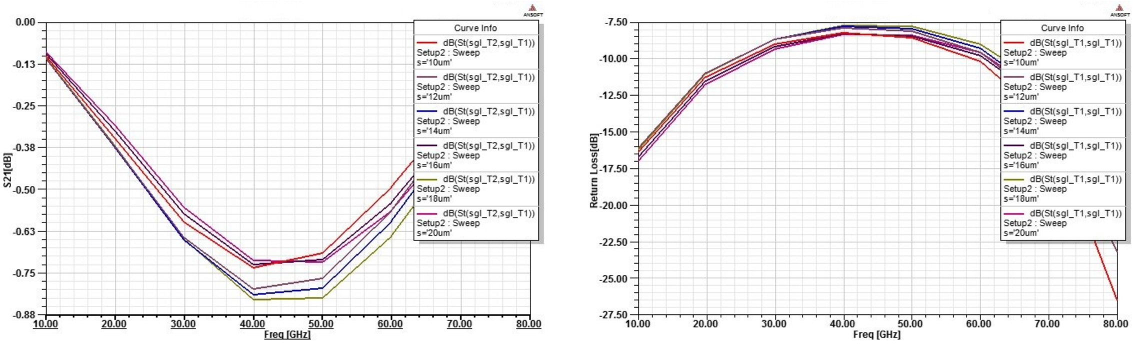

(a) Loss S_{21} with varying gaps between sets of ribbons

(b) Return loss S_{11} with varying gaps between sets of ribbons

Figure 5.21: S-CPW Phase Shifter RF characteristics

study the deformation due to stress gradient. Figure 5.22 shows the model using CoventorWare for electromechanical analysis. Sets of metallic shunting membranes can be actuated electrostatically either individually or in groups. The airgap between the standing ribbons and CPW transmission lines is 2 μm.

5.10 Results and Discussions

The Slow-Wave Distributed True-Time Delay RF MEMS based phase shifter with five sets of actuating ribbons is designed. With five sets of ribbons, the phase shifter is tunable in 2^5 modes. As already discussed, the ribbons in a set are actuated in unison electrostatically.

It is observed from simulation results that the pull-in voltage of the actuating membranes lies in the range 8.8 - 10 V and the phase shifter provides phase shifts with

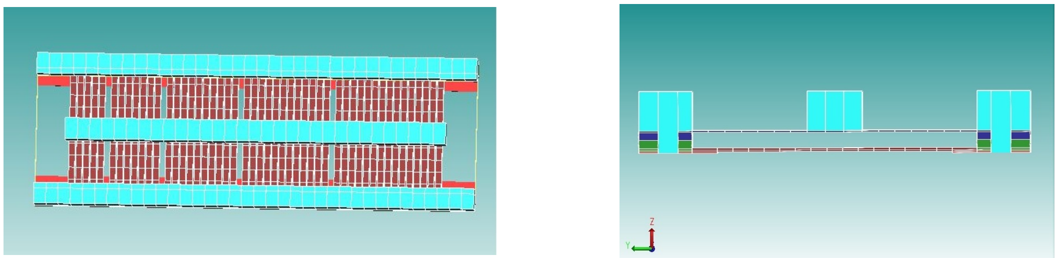

(a) Top view of the phase shifter model.

(b) Cross-sectional view of the model

Figure 5.22: Electromechanical model in CoventorWare.

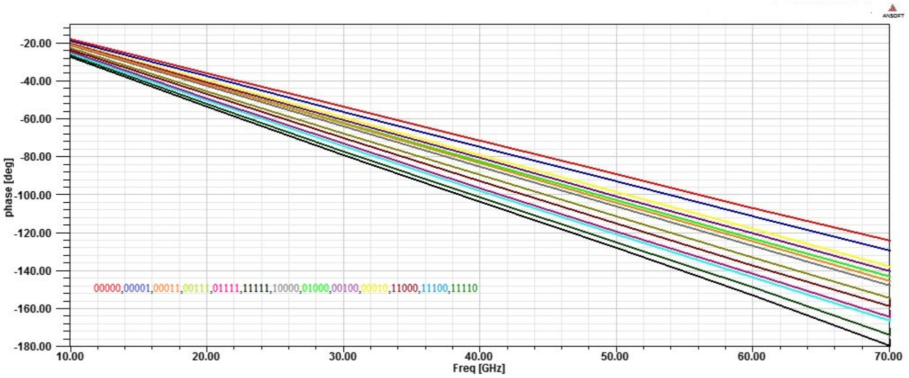

Figure 5.23: Phase plot of the phase shifter.

very low insertion loss and low return loss in certain bands of frequencies. Based on the simulation results, the following 13 combinations of actuating sets are identified, 00000, 00001, 00011, 00111, 01111, 11111, 11110, 11100, 11000, 10000, 01000, 00100, and 00010, with 0 and 1 representing unactuated and actuated sets respectively. Figures 5.23 - 5.25 shows the phase shifts and RF characteristics obtained for various actuating combinations of sets. Figure 5.24 shows the S_{21} of the proposed design. The plot contains result of 13 combinations of switches. The minimum and maximum insertion loss incurred from the design is found to be 0.24 dB and less than 0.8 dB respectively at 70 GHz.

Table 5.2 provides a brief insight into various phase shifts that can be obtained at different frequencies, associated insertion loss and return loss. In this table, phase shifts and S-parameters for only 11111 and 00000 combinations are shown.

Table 5.3 shows the comparison of phase shifter performance of the present work with those published in the literature.

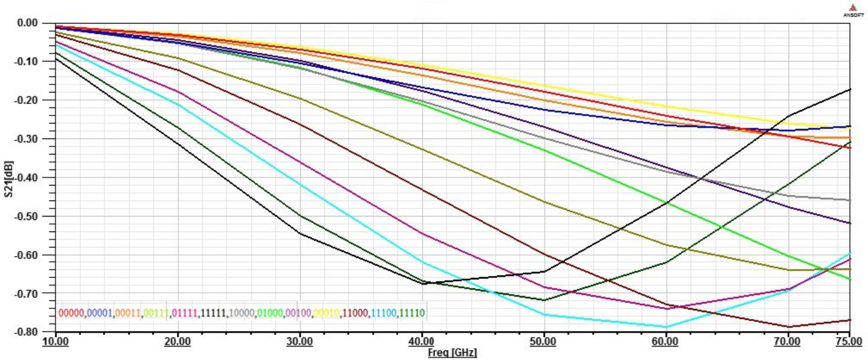

Figure 5.24: Insertion loss S_{21} of the phase shifter when different sets of ribbons are actuated.

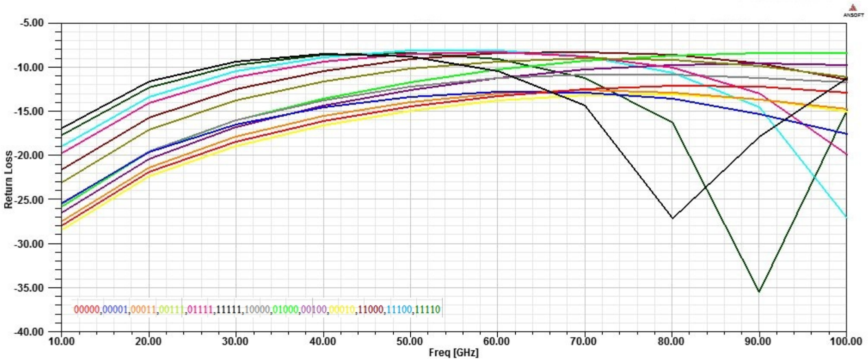

Figure 5.25: Return loss S_{11} of phase shifter when different sets of ribbons are actuated.

Table 5.2: Table showing phase shift, insertion loss and return loss at different frequencies for two combinations.

	Phase Shift		Insertion Loss		Return Loss	
Freq(GHz)	11111	00000	11111	00000	11111	00000
10	-27.1721	-17.8696	0.09185	0.00764	-16.8214	-27.8182
20	-53.5419	-35.7251	0.31385	0.03039	-11.6057	-21.8439
30	-78.8191	-53.551	0.54577	0.06746	-9.33315	-18.4172
40	-103.305	-71.3248	0.67492	0.11744	-8.5083	-16.0823
50	-127.681	-89.0171	0.6428	0.17689	-8.7959	-14.4022
60	-152.746	-106.606	0.46518	0.2388	-10.3916	-13.2171
70	-179.09	-124.109	0.2386	0.29346	-14.3269	-12.4749

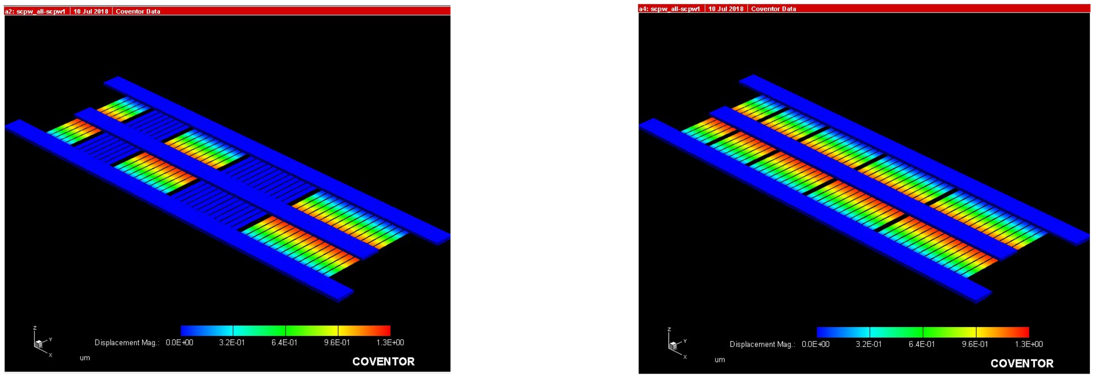

(a) Phase shifter with alternate sets (10101) actuated. **(b)** Phase shifter with all sets (11111) actuated.

Figure 5.26: S-CPW Phase Shifter model in MEMS solver CoventorWare

Table 5.3: Table showing comparison of present work with similar works from literature

Author	Frequency (GHz)	Substrate	Insertion Loss (dB)	Return Loss (dB)	Phase Shift (°)	Size (mm^2)
Kanthamani *et al.* (2017)	15	HRS	-0.5	-38	-	2*3
Pillans *et al.* (2012)	15-35	Alumina	-1.7- -2.7	-	22.5-180	-
Abdellatif *et al.* (2015)	24.5-26.5	Alumina	-0.75	-15	20	0.5*1.5
Chakraborty *et al.* (2014)	15	Silicon	-0.33	-18	15	-
Unlu *et al.* (2013)	15-25	Quartz	-3.6	-19	0-180	5.9*10.8
Ramli *et al.* (2017)	2-4	HRS	-2.95	-10	315	30*10
This work	10-70	HRS	-0.1- -0.67	-8.9- -27	28-180	0.5*5

5.11 Conclusion

Slow-wave distributed true-time delay RF MEMS based phase shifter is modelled in ANSYS HFSS. The electro-mechanical modeling of the actuating membranes is done in FEM solver CoventorWare. This is a tunable 5-bit phase shifter and the required phase can be generated by the controlled actuation of sets of ribbons through different bit combinations. The bit combinations were achieved by grouping ribbons, with each set having variable number of ribbons. The phase shifter is proposed to be fabricated on a 500 μm silicon substrate. The insertion loss of the phase shifter is reduced by adding a shielded plane below the co-planar waveguide transmission line. Desired phase is obtained by capacitively loading the transmission line by 10 μm width gold ribbons placed underneath the CPW transmission line. Slow wave structure is realized by this periodic loading of transmission line. The design resulted in a maximum phase shift of 28°, an insertion loss and isolation better than 0.1 dB and 28 dB respectively, is observed at 10 GHz. Also, 180° phase with 0.24dB insertion loss and return loss below -10dB at 70GHz. The design provided a phase shift tunability of 18° to 28° at 10 GHz and 124° to 180° at 70 GHz.

Chapter 6

CONCLUSIONS AND FUTURE SCOPE

MEMS Switches and MEMS based varactors forms the important RF components in the design of radio frequency integrated circuits. MEMS switches are the most fundamental building blocks in the design of RF devices. The distinguishing characteristic of RF MEMS switches is that their RF characteristics are reconfigurable or tunable by the mechanical movement of conducting membranes. Multifunction, miniaturization and high integration drives the use of MEMS in composite electronic products. Owing to their very low insertion loss, high isolation, miniscule power consumption and excellent linearity, RF MEMS switches finds application in tunable phase shifters and filters and reconfigurable antennas. In the proposed work, membrane structural geometry are modified by incorporating various serpentine flexures to reduce the stiffness and adding series inductance to the membrane. This results in low actuation voltage and the tuning of RF characteristics for X, Ku, K and Ka bands. Electromechanical modelling of the proposed switches are carried out in MEMS solver CoventorWare. The electromagnetic behaviour of the designed switches is analysed from the S-parameters which are extracted from the ANSYS HFSS. The switch designs are optimized for low actuation voltage and superior RF performance in the respective frequency bands. The optimized switch designs are fabricated on high resistive silicon substrate by a five mask micromachining process. DC characterization shows that X band membrane geometry is pulled down at 10 volts and that of Ku band actuates at 18.5 Volts. It is observed that the measured values of pull-in voltage is more than the simulation results by 2-3 volts. This is due to stress induced distortions leading to lateral bowing or membrane buckling. RF characterization shows that the insertion loss and isolation of the fabricated switches is better than 0.46 dB and -30 dB respectively.

A single pole four throw RF MEMS switch for X band operation is designed by employing a cascade combination of series and shunt SPST switches in the signal path to each output port. The switch geometry has separate actuation pads for independent switching of the membranes. The input RF signal gets connected to any of the four ports, depending on the ON/OFF status of the pair of SPST switches in the signal path. Parametric analyses are done to optimize device dimensions for superior RF performance. Electromechanical simulation results show that the actuation voltage of series switch is 13.75 V and that of the shunt switch is 12 V. S-parameters of the switch extracted from HFSS shows that the insertion loss and isolation are better than 0.7 dB and 51 dB respectively at 10 GHz.

Tunable RF MEMS filters provide a more compact and flexible approach for the same functionality as that of filter bank front end in multi-band circuits. MEMS based switches and varactors are used for tuning filter characteristics. The proposed bandpass filter is designed by cascading high pass and low pass filters. High pass filter functionality is realized by a series combination of series capacitor with a shunt inductor while that of the low pass filter by a series combination of series inductors and shunt capacitors. Inductors are realized by CPW transmission lines and capacitors by MEMS cantilevers and shunt varactors. FEM simulation is carried out to assess the DC performance of cantilevers and shunt membranes. Full wave electromagnetic simulation results of the bandpass filter shows that the filter characteristics are suitable for X band operation. Filter response shows that the bandwidth and centre frequency of the filter are 5.4 GHz and 11.86 GHz respectively, with a roll off rate close to that of eighth order. Tunability of the filter is achieved by selective and controlled actuation of series cantilevers and shunt membranes. Thus, tunability in bandwidth from 2.34 GHz to 5.4 GHz and that of centre frequency from 11.86 GHz to 15.76 GHz is achieved.

True time delay tunable phase shifters employing RF MEMS technology is designed for serving as true time delay networks in phased array antennas. The proposed phase shifter is designed on a slow wave coplanar waveguide transmission line. This design employs floating shield concept to reduce substrate losses. Five sets of floating metallic membranes or ribbons are used to achieve tunabilty in phase shift. With five sets of ribbons, the phase shifter is tunable in 32 modes. The dielectric layer enables effective capacitive loading of the transmission line by the actuating ribbons. This capacitive loading alters the phase velocity of the propagating signal leading to phase shift. RF results show that the insertion loss and return loss are better than 0.8 dB and 8 dB respectively at 70 GHz with the maximum phase shift of 180° at 70 GHz.

6.1 Future Scope

Most of the research on MEMS switches is confined to the centimeter band from 3 GHz to 40 GHz. However, with advancements in the field of communication technology, the demand for increased wireless bandwidth have become prominent. It can also be seen that due to overcrowding, the original communication band is unable to meet the exponential communication bandwidth requirements. This emerging scenario causes the gradual shifting of the communication system toward the millimeter wave (30-–300 GHz) and sub-millimeter-wave (300-–3000 GHz) band. Communication requirements and transmission technologies suitable for operation in these bands have emerged as the current research hotspot. Though MEMS switches have proved to exhibit excellent RF characteristics and are widely used in the centimeter band, their parasitic effect increases significantly as frequency increases. This results in drastic deterioration of the isolation characteristics. Also the skin effect of the conductor is significantly increased in the millimeter and millimeter-wave frequencies, worsening the insertion loss. In addition to this, reliability issues due to dielectric charging, contact failures, temperature instability and packaging issues are the factors that limits the use of MEMS switches at high frequencies. Future research status points to developing high performance switches in sub-millimeter bands satisfying reliability issues.

Bibliography

Abdellatif, A., **A. A. Aziz**, **R. Mansour**, and **S. Safavi-Naeini** (2015). Low-loss compact MEMS phase shifter for phased array antennas. *Electronics Letters*, **51**(15), 1142–1144.

Aigner, R., **J. Ella**, **H.-J. Timme**, **L. Elbrecht**, **W. Nessler**, and **S. Marksteiner**, Advancement of MEMS into RF-filter applications. *In Electron Devices Meeting, 2002. IEDM'02. International*. IEEE, 2002.

Bakri-Kassem, M., **R. R. Mansour**, and **S. Safavi-Naeini**, A novel latching RF MEMS phase shifter. *In Microwave Conference (EuMC), 2014 44th European*. IEEE, 2014.

Balaraman, D., **S. Bhattacharya**, **F. Ayazi**, and **J. Papapolymerou**, Low-cost low actuation voltage copper RF MEMS switches. *In IEEE MTT-S International Microwave Symposium Digest, 2002*, volume 2. IEEE, 2002.

Barker, N. S. and **G. M. Rebeiz** (2000). Optimization of distributed MEMS transmission-line phase shifters-U-band and W-band designs. *IEEE Transactions on Microwave Theory and Techniques*, **48**(11), 1957–1966.

Barker, S. and **G. M. Rebeiz** (1998). Distributed MEMS true-time delay phase shifters and wide-band switches. *IEEE Transactions on Microwave Theory and Techniques*, **46**(11), 1881–1890.

Birleanu, C., **M. Pustan**, **V. Merie**, **R. Müller**, **R. Voicu**, **A. Baracu**, and **S. Craciun**, Temperature effect on the mechanical properties of gold nano films with different thickness. *In IOP Conference Series: Materials Science and Engineering*, volume 147. IOP Publishing, 2016.

Black, W. (1965). A bandwidth-insertion-loss tradeoff. *IEEE Transactions on Circuit Theory*, **12**(4), 615–617.

Borgioli, A., **Y. Liu**, **A. S. Nagra**, and **R. A. York** (2000). Low-loss distributed MEMS phase shifter. *IEEE Microwave and Guided wave letters*, **10**(1), 7–9.

Bovadilla, R., **O. Molitor**, **A. Serrano**, and **G. Rehder**, Optimization of RF MEMS phase shifter for microwaves applications. *In Microelectronics Technology and Devices (SBMicro), 2017 32nd Symposium on*. IEEE, 2017.

Brown, A. R. and **G. M. Rebeiz** (2000). A varactor-tuned RF filter. *IEEE Transactions on Microwave Theory and Techniques*, **48**(7), 1157–1160.

Cadiou, S., **B. Potelon**, **C. Quendo**, **E. Rius**, **J.-F. Favennec**, **R. Segalen**, and **F. Mahé**, Highly-miniaturized packaged UWB 7th-order bandpass filter. *In Microwave Conference (EuMC), 2010 European*. IEEE, 2010.

Cai, M., **X.-l. Guo**, **Y. Li**, **L. Liu**, and **Z.-s. Lai**, Design and modeling of reconfigurable MEMS low pass filter. *In Solid-State and Integrated Circuit Technology, 2006. ICSICT'06. 8th International Conference on*. IEEE, 2006.

Chakraborty, A. and **B. Gupta** (2017). Paradigm phase shift: RF MEMS phase shifters: an overview. *IEEE Microwave Magazine*, **18**(1), 22–41.

Chakraborty, A., **B. Gupta**, and **B. K. Sarkar** (2014). Design, fabrication and characterization of miniature RF MEMS switched capacitor based phase shifter. *Microelectronics Journal*, **45**(8), 1093–1102.

Chan, K. Y., **R. Ramer**, **R. R. Mansour**, and **Y. J. Guo** (2014). 60 GHz to E-band switchable bandpass filter. *IEEE Microwave and Wireless Components Letters*, **24**(8), 545–547.

Chan, R., **R. Lesnick**, **D. Becher**, and **M. Feng** (2003). Low-actuation voltage RF MEMS shunt switch with cold switching lifetime of seven billion cycles. *Journal of Microelectromechanical Systems*, **12**(5), 713–719.

Cheung, T. S. D. and **J. R. Long** (2006). Shielded passive devices for silicon-based monolithic microwave and millimeter-wave integrated circuits. *IEEE Journal of Solid-state circuits*, **41**(5), 1183–1200.

Cho, I., **T. Song**, **S. Baek**, and **E. Yoon** (2005). A low-voltage and low-power RF MEMS series and shunt switches actuated by combination of electromagnetic and electrostatic forces. *IEEE Transactions on Microwave Theory and Techniques,*, **53**(7), 2450–2457.

Cusmai, G., **M. Mazzini**, **P. Rossi**, **C. Combi**, **B. Vigna**, and **F. Svelto** (2005). A simple lumped electrical model for an RF MEMS switch considering lossy substrate effects. *Sensors and Actuators A: Physical*, **123**, 515–521.

Dai, C.-L. and **J.-H. Chen** (2006). Low voltage actuated RF micromechanical switches fabricated using CMOS-MEMS technique. *Microsystem technologies*, **12**(12), 1143–1151.

Demirel, K., **E. Yazgan**, **Ş. Demir**, and **T. Akın** (2016). A new temperature-tolerant RF MEMS switch structure design and fabrication for Ka-Band applications. *Journal of Microelectromechanical Systems*, **25**(1), 60–68.

Dey, S. and **S. K. Koul** (2015). Reliability analysis of Ku-band 5-bit phase shifters using MEMS SP4T and SPDT switches. *IEEE Transactions on Microwave Theory and Techniques*, **63**(12), 3997–4012.

Dey, S., **S. K. Koul**, **A. K. Poddar**, and **U. L. Rohde** (2016). Extensive performance evaluations of RF MEMS single-pole-multi-throw (SP3T to SP14T) switches up to X-band frequency. *Journal of Micromechanics and Microengineering*, **27**(1), 014002.

Du, Y., **J. Bao**, **W. Wu**, **C. Tu**, and **P. Mu**, Modeling and design of 5-bit X-band RF MEMS distributed phase shifter. *In Microwave and Millimeter Wave Technology (ICMMT), 2010 International Conference on*. IEEE, 2010.

Dussopt, L. and **G. M. Rebeiz** (2003). Intermodulation distortion and power handling in RF MEMS switches, varactors, and tunable filters. *IEEE Transactions on Microwave Theory and Techniques*, **51**(4), 1247–1256.

Ekkels, P., **X. Rottenberg**, **R. Puers**, and **H. Tilmans** (2009). Evaluation of platinum as a structural thin film material for RF-MEMS devices. *Journal of Micromechanics and Microengineering*, **19**, 065010.

Entesari, K. and **G. M. Rebeiz** (2005). A differential 4-bit 6.5-10-GHz RF MEMS tunable filter. *IEEE transactions on microwave theory and techniques*, **53**(3), 1103–1110.

Fang, W. and **J. Wickert** (1996). Determining mean and gradient residual stresses in thin films using micromachined cantilevers. *Journal of Micromechanics and Microengineering*, **6**(3), 301.

Feng, Z., **W. M. Fathelbab**, **P. G. Lam**, **V. Haridasan**, **J.-P. Maria**, **A. I. Kingon**, and **M. B. Steer**, Narrowband barium strontium titanate (BST) tunable bandpass filters at X-band. *In Microwave Symposium Digest, 2009. MTT'09. IEEE MTT-S International*. IEEE, 2009.

Fouladi, S., **F. Huang**, **W. D. Yan**, and **R. R. Mansour** (2013). High-Q narrowband tunable combline bandpass filters using MEMS capacitor banks and piezomotors. *IEEE Transactions on Microwave Theory and Techniques*, **61**(1), 393–402.

Fouladi, S., **W. D. Yan**, and **R. R. Mansour**, Microwave tunable bandpass filter with MEMS thermal actuators. *In Microwave Conference, 2008. EuMC 2008. 38th European*. IEEE, 2008.

Generalov, A., **D. Lioubtchenko**, and **A. Räisänen**, Reconfigurable mm-wave phase shifter based on high impedance surface with carbon nanotube membrane MEMS. *In Millimeter Waves (GSMM), 2015 Global Symposium On*. IEEE, 2015.

Golaszewski, A., **M. Zukocinski**, and **A. Abramowicz**, Design of varactor tuned bandpass filter. *In Microwave Techniques (COMITE), 2015 Conference on*. IEEE, 2015.

Goldsmith, C. L., **Z. Yao**, **S. Eshelman**, and **D. Denniston** (1998). Performance of low-loss RF MEMS capacitive switches. *IEEE Microwave and guided wave letters*, **8**(8), 269–271.

Greenhouse, H. (1974). Design of planar rectangular microelectronic inductors. *IEEE Transactions on Parts, Hybrids, and Packaging,*, **10**(2), 101–109.

Guo, F., **Z. Zhu**, **Y. Long**, **W. Wang**, **S. Zhu**, **Z. Lai**, **N. Li**, **G. Yang**, and **W. Lu** (2003). Study on low voltage actuated MEMS rf capacitive switches. *Sensors and Actuators A: Physical*, **108**(1-3), 128–133.

Hacker, J. B., **R. E. Mihailovich**, **M. Kim**, and **J. F. DeNatale** (2003). A Ka-band 3-bit RF MEMS true-time-delay network. *IEEE transactions on microwave theory and techniques*, **51**(1), 305–308.

Hafez, W., **W. Snodgrass**, and **M. Feng** (2005). 12.5 nm base pseudomorphic heterojunction bipolar transistors achieving f= 710 GHz and f= 340 GHz. *Applied Physics Letters*, **87**, 252109.

Hayden, J. S. and **G. M. Rebeiz** (2000*a*). 2-bit MEMS distributed X-band phase shifters. *IEEE Microwave and guided wave letters*, **10**(12), 540–542.

Hayden, J. S. and **G. M. Rebeiz**, One and two-bit low-loss cascadable MEMS distributed X-band phase shifters. *In Microwave Symposium Digest. 2000 IEEE MTT-S International*, volume 1. IEEE, 2000*b*.

Hayden, J. S. and **G. M. Rebeiz** (2003). Very low-loss distributed X-band and Ka-band MEMS phase shifters using metal-air-metal capacitors. *IEEE Transactions on Microwave Theory and Techniques*, **51**(1), 309–314.

Hung, J.-J., **L. Dussopt**, and **G. M. Rebeiz** (2004). Distributed 2-and 3-bit W-band MEMS phase shifters on glass substrates. *IEEE Transactions on Microwave Theory and Techniques*, **52**(2), 600–606.

Hunter, I. and **J. D. Rhodes** (1982). Electronically tunable microwave bandpass filters. *IEEE Transactions on Microwave Theory and Techniques*, **30**(9), 1354–1360.

Jaimes-Vera, A., **I. Llamas-Garro**, **A. Corona-Chavez**, and **I. Zaldivar-Huerta**, Review on microwave and millimeter filters using MEMS technology. *In Electronics, Communications and Computers, 2007. CONIELECOMP'07. 17th International Conference on*. IEEE, 2007.

Jensen, B., **Z. Wang**, **L. Chow**, **K. Saitou**, **K. Kurabayashi**, and **J. Volakis** (2003). Integrated electrothermal modeling of RF MEMS switches for improved power handling capability, 10–11.

Kalkur, T., **N. Sbrockey**, **G. Tompa**, and **Alpay** (2010*a*). Design and Simulation of Tunable Ka Band Filters with Graded Barium Strontium Titanate (BST) Varactors. *Integrated Ferroelectrics*, **111**(1), 50–58.

Kalkur, T., **N. Sbrockey**, **G. Tompa**, **P. Alpay**, **J. Spanier**, **E. Galow**, and **M. Cole** (2010*b*). Low Voltage Tunable Band Pass Filters Using Barium Strontium Titanate Parallel Plate Capacitors. *Integrated Ferroelectrics*, **112**(1), 1–7.

Kang, D.-W., **H. D. Lee**, **C.-H. Kim**, and **S. Hong** (2006). Ku-band MMIC phase shifter using a parallel resonator with 0.18-/spl mu/m CMOS technology. *IEEE Transactions on Microwave Theory and Techniques*, **54**(1), 294–301.

Kanthamani, S., **N. M. Sindhuja**, and **R. Priyanka**, Analysis of DMTL phase shifter using RF MEMS power sensor. *In 2017 Conference on Emerging Devices and Smart Systems (ICEDSS)*. IEEE, 2017.

Keane, W. (1978). Narrow-band YIG filters aid wide-open receivers. *Microwaves*, **17**, 50–54.

Kim, H.-T., **J.-H. Park**, **Y.-K. Kim**, and **Y. Kwon**, Millimeter-wave micromachined tunable filters. *In Microwave Symposium Digest, 1999 IEEE MTT-S International*, volume 3. IEEE, 1999.

Lacroix, B., **A. Pothier**, **A. Crunteanu**, **C. Cibert**, **F. Dumas-Bouchiat**, **C. Champeaux**, **A. Catherinot**, and **P. Blondy** (2007). Sub-microsecond RF MEMS switched capacitors. *IEEE Transactions on Microwave Theory and Techniques,*, **55**(6), 1314–1321.

Lakshminarayanan, B. and **T. Weller**, Tunable bandpass filter using distributed MEMS transmission lines. *In Microwave Symposium Digest, 2003 IEEE MTT-S International*, volume 3. IEEE, 2003.

Lampen, J., **S. Majumder**, **C. Ji**, and **J. Maciel**, Low-loss, MEMS based, broadband phase shifters. *In Phased Array Systems and Technology (ARRAY), 2010 IEEE International Symposium on*. IEEE, 2010.

Larson, L. E., **R. H. Hackett**, **M. A. Melendes**, and **R. F. Lohr**, Micromachined microwave actuator (MIMAC) technology-a new tuning approach for microwave integrated circuits. *In Microwave and Millimeter-Wave Monolithic Circuits Symposium Digest*. 1991.

Lin, J., The ultra-wideband RF MEMS single-pole-four-throw switch. *In Antennas and Propagation (ISAP), 2016 International Symposium on*. IEEE, 2016.

Lin, T.-W., **K. K. W. Low**, **R. Gaddi**, and **G. M. Rebeiz**, High-Linearity 5.3-7.0 GHz 3-Pole Tunable Bandpass Filter Using Commercial RF MEMS Capacitors. *In 2018 48th European Microwave Conference (EuMC)*. IEEE, 2018.

Liu, Y., **A. Borgioli**, **A. S. Nagra**, and **R. A. York** (2000). K-band 3-bit low-loss distributed MEMS phase shifter. *IEEE Microwave and Guided Wave Letters*, **10**(10), 415–417.

Malczewski, A., **S. Eshelman**, **B. Pillans**, **J. Ehmke**, and **C. Goldsmith** (1999). X-band RF MEMS phase shifters for phased array applications. *IEEE Microwave and Guided Wave Letters*, **9**(12), 517–519.

Mao, S., **H. Wang**, **Y. Wu**, **J. Tang**, and **G. Ding**, A latching bistable microswitch using dual-beam electrothermal actuation. *In 5th IEEE International Conference on Nano/Micro Engineered and Molecular Systems (NEMS), 2010*. IEEE, 2010.

Maruhashi, K., **H. Mizutani**, and **K. Ohata** (2000). Design and performance of a Ka-band monolithic phase shifter utilizing nonresonant FET switches. *IEEE Transactions on Microwave Theory and Techniques*, **48**(8), 1313–1317.

Matthaei, G., **L. Young**, and **E. Jones** (1980). Microwave Filters, Impedance-Matching Networks, and Coupling Structures. *Artech House, February*.

Mercier, D., **P. Charvet**, **P. Berruyer**, **C. Zanchi**, **L. Lapierre**, **O. Vendier**, **J. Cazaux**, and **P. Blondy**, A DC to 100 GHz high performance ohmic shunt switch. *In Microwave Symposium Digest, 2004 IEEE MTT-S International*, volume 3. IEEE, 2004.

Mercier, D., **K. Van Caekenberghe**, and **G. Rebeiz**, Miniature RF MEMS switched capacitors. *In Microwave Symposium Digest, 2005 IEEE MTT-S International*. IEEE, 2005.

Milosavljevic, Z. D. (2004). RF MEMS switches. *Mikrotalasna revija*, **10**(1), 2–8.

Motoi, K., **N. Oshima**, **M. Kitsunezuka**, and **K. Kunihiro**, A band-switchable and tunable nested bandpass filter with continuous 0.4–3GHz coverage. *In 2016 11th European Microwave Integrated Circuits Conference (EuMIC)*. IEEE, 2016.

Muldavin, J. and **G. Rebeiz** (2000*a*). High-isolation CPW MEMS shunt switches. 1. Modeling. *IEEE Transactions on Microwave Theory and Techniques*, **48**(6), 1045–1052.

Muldavin, J. and **G. Rebeiz** (2000*b*). High-isolation CPW MEMS shunt switches. 2. Design. *IEEE Transactions on Microwave Theory and Techniques,*, **48**(6), 1053–1056.

Muldavin, J. and **G. Rebeiz** (2001). Inline capacitive and DC-contact MEMS shunt switches. *IEEE Microwave and Wireless Components Letters,*, **11**(8), 334–336.

Murakami, Y. and **S. Itoh**, A bandpass filter using YIG film grown by LPE. *In Microwave Symposium Digest, 1985 IEEE MTT-S International*. IEEE, 1985.

Nataraj, B. and **K. Porkumaran** (2012). Investigation of RF MEMS phase shifter using tapered coplanar waveguide. *European Journal of Scientific Research*, **69**(3), 360–369.

Pacheco, S., **L. Katehi**, and **C. Nguyen**, Design of low actuation voltage RF MEMS switch. *In IEEE MTT-S International Microwave Symposium Digest., 2000*, volume 1. IEEE, 2000.

Pacheco, S., **C. T. Nguyen**, and **L. P. Katehi**, Micromechanical electrostatic K-band switches. *In Microwave Symposium Digest, 1998 IEEE MTT-S International*, volume 3. IEEE, 1998.

Peddireddy, P., **C. Kush**, *et al.*, Micromachined wide bandpass filter. *In 2015 International Conference on Communications and Signal Processing (ICCSP)*. IEEE, 2015.

Peng, Z., **X. Yuan**, **J. Hwang**, **D. Forehand**, and **C. Goldsmith**, Dielectric charging of RF MEMS capacitive switches under bipolar control-voltage waveforms. *In IEEE/MTT-S International Microwave Symposium, 2007.*. IEEE, 2007.

Peroulis, D., **S. Pacheco**, **K. Sarabandi**, and **L. P. Katehi**, Tunable lumped components with applications to reconfigurable MEMS filters. *In Microwave Symposium Digest, 2001 IEEE MTT-S International*, volume 1. IEEE, 2001.

Peroulis, D., **S. P. Pacheco**, **K. Sarabandi**, and **L. P. Katehi** (2003). Electromechanical considerations in developing low-voltage RF MEMS switches. *IEEE Transactions on microwave theory and techniques*, **51**(1), 259–270.

Persano, A., **A. Tazzoli**, **A. Cola**, **P. Siciliano**, **G. Meneghesso**, and **F. Quaranta** (2012). Reliability Enhancement by Suitable Actuation Waveforms for Capacitive RF MEMS Switches in III–V Technology. *Journal ofMicroelectromechanical Systems,*, (99), 1–6.

Petersen, K. (1979). Micromechanical membrane switches on silicon. *IBM Journal of Research and Development*, **23**(4), 376–385.

Pillans, B., **L. Coryell**, **A. Malczewski**, **C. Moody**, **F. Morris**, and **A. Brown**, Advances in rf mems phase shifters from 15 ghz to 35 ghz. *In 2012 IEEE/MTT-S International Microwave Symposium Digest*. IEEE, 2012.

Pillans, B., **S. Eshelman**, **A. Malczewski**, **J. Ehmke**, and **C. Goldsmith** (1999). Ka-band RF MEMS phase shifters. *IEEE Microwave and Guided Wave Letters*, **9**(12), 520–522.

Pozar, D. M., *Microwave engineering*. John Wiley & Sons, 2012.

Ramli, N. A. and **T. Arslan**, Design and simulation of a 2-bit distributed S-band MEMS phase shifter. *In Thermal, Mechanical and Multi-Physics Simulation and Experiments in Microelectronics and Microsystems (EuroSimE), 2017 18th International Conference on*. IEEE, 2017.

Ramli, N. A., **T. Arslan**, and **N. Haridas**, Design and simulation of a 3-bit DMTL phase shifter for wideband applications. *In 2017 Symposium on Design, Test, Integration and Packaging of MEMS/MOEMS (DTIP)*. IEEE, 2017.

Rebeiz, G. M., *RF MEMS: Theory, Design, and Technology*. John Wiley & Sons, 2004.

Rebeiz, G. M., **G.-L. Tan**, and **J. S. Hayden** (2002). RF MEMS phase shifters: design and applications. *IEEE microwave magazine*, **3**(2), 72–81.

Roy, S. C. and **K. J. Rangra**, Design optimization of RF MEMS SP4T and SP6T switch. *In Emerging Trends in Engineering and Technology (ICETET), 2010 3rd International Conference on*. IEEE, 2010.

Saha, S. C., **U. Hanke**, **H. Sagberg**, **T. A. Fjeldly**, and **T. Saether** (2011). Tunable band-pass filter using RF MEMS capacitance and transmission line. *Progress In Electromagnetics Research*, **23**, 233–247.

Sharma, P., **S. K. Koul**, and **S. Chandra** (2007). Studies on RF MEMS shunt switch. *Indian Journal of Pure and Applied Physics*, **45**.

Shekhar, S., **K. Vinoy**, and **G. Ananthasuresh** (2011). Switching and release time analysis of electrostatically actuated capacitive RF MEMS switches. *Sensors & Transducers*, **130**(7), 77.

Shekhar, S., **K. Vinoy**, and **G. Ananthasuresh** (2017). Surface-micromachined capacitive RF switches with low actuation voltage and steady contact. *Journal of Microelectromechanical Systems*, **26**(3), 643–652.

Siegel, C., **V. Zieglerl**, **U. Prechtel**, **B. Schonlinner**, and **H. Schumacher**, A Ka-band RF-MEMS phase shifter approach based on a novel dual-state microstrip line. *In Microwave Integrated Circuit Conference, 2007. EuMIC 2007. European*. IEEE, 2007.

Simion, S., Modeling and design aspects of the MEMS switch. *In 2003 International Semiconductor Conference. CAS 2003 Proceedings (IEEE Cat. No. 03TH8676)*, volume 1. IEEE, 2003.

Spengen, W., **R. Puers**, **R. Mertens**, and **I. Wolf** (2004). A comprehensive model to predict the charging and reliability of capacitive RF MEMS switches. *Journal of Micromechanics and Microengineering*, **14**, 514.

Sumant, P., **A. Cangellaris**, and **N. Aluru** (2007). Modeling of dielectric charging in RF MEMS capacitive switches. *Microwave and Optical technology letters*, **49**(12), 3188–3192.

Takacs, A., **D. Neculoiu**, **D. Vasilache**, **A. Muller**, **P. Pons**, **H. Aubert**, and **R. Plana**, An Innovative and Versatile Topology for Tunable Bandpass Filter. *In Semiconductor Conference, 2007. CAS 2007. International*, volume 1. IEEE, 2007.

Tan, G.-L., **R. E. Mihailovich**, **J. B. Hacker**, **J. F. DeNatale**, and **G. M. Rebeiz** (2003). Low-loss 2- and 4-bit TTD MEMS phase shifters based on SP4T switches. *IEEE Transactions on Microwave Theory and Techniques*, **51**(1), 297–304.

Topalli, K., **M. Unlu**, **H. Atasoy**, **S. Demir**, **O. Aydin Civi**, and **T. Akin** (2009). Empirical formulation of bridge inductance in inductively tuned RF MEMS shunt switches. *Progress In Electromagnetics Research*, **97**, 343–356.

Ulm, M., **M. Reimann**, **T. Walter**, **R. Muller-Fiedler**, and **E. Kasper**, Capacitive rf-mems switches for the w-band. *In EUROPEAN MICROWAVE CONFERENCE*, volume 31. Nexus Media Limited; 1996, 2001.

Unlu, M., **S. Demir**, and **T. Akin** (2013). A 15–40-GHz frequency reconfigurable RF MEMS phase shifter. *IEEE Transactions on Microwave Theory and Techniques*, **61**(8), 2865–2877.

Varadan, V. K., **K. J. Vinoy**, and **K. A. Jose**, *RF MEMS and their applications*. John Wiley & Sons, 2003.

Verona, B., **G. Rehder**, **A. Serrano**, **M. Carreño**, and **P. Ferrari**, Slow-wave distributed MEMS phase shifter in CMOS for millimeter-wave applications. *In Microwave Conference (EuMC), 2014 44th European*. IEEE, 2014.

Xiaofeng, L., **L. Zewen**, **L. Zhijian**, **C. Zhongmin**, and **L. Litian**, Design of coils inductively-tuned RF MEMS shunt switches using novel modeling method. *In Proceedings. 7th International Conference on Solid-State and Integrated Circuits Technology, 2004.*, volume 3. IEEE, 2004.

Yang, H.-H., **A. Yahiaoui**, **H. Zareie**, **P. Blondy**, and **G. M. Rebeiz**, A compact high-isolation DC-50 GHz SP4T RF MEMS switch. *In Microwave Symposium (IMS), 2014 IEEE MTT-S International*. IEEE, 2014.

Yao, Z. J., **S. Chen**, **S. Eshelman**, **D. Denniston**, and **C. Goldsmith** (1999). Micromachined low-loss microwave switches. *Journal of Microelectromechanical Systems*, **8**(2), 129–134.

Yu, A., **A. Liu**, **Q. Zhang**, and **H. Hosseini** (2006). Effects of surface roughness on electromagnetic characteristics of capacitive switches. *Journal of Micromechanics and Microengineering*, **16**, 2157.

Yu, Y.-W., **J. Zhu**, **S.-X. Jia**, and **Y. Shi** (2009). A high isolation series-shunt RF MEMS switch. *Sensors*, **9**(6), 4455–4464.

Yuk, K. Y., **S. Fouladi**, **R. Ramer**, and **R. R. Mansour** (2012). RF MEMS switchable interdigital bandpass filter. *IEEE Microwave and Wireless Components Letters*, **22**(1), 44–46.

Yun, T.-Y. and **K. Chang** (2002). Piezoelectric-transducer-controlled tunable microwave circuits. *IEEE Transactions on Microwave Theory and Techniques*, **50**(5), 1303–1310.

Zareie, H. and **G. M. Rebeiz** (2014). Compact high-power SPST and SP4T RF MEMS metal-contact switches. *IEEE transactions on microwave theory and techniques*, **62**(2), 297–305.

Zhang, N., **L. Mei**, **C. Wang**, **Z. Deng**, **J. Yang**, and **Q. Guo** (2017). A Switchable Bandpass Filter Employing RF MEMS Switches and Open-Ring Resonators. *IEEE Transactions on Electron Devices*, **64**(8), 3377–3383.

Zhao, Z., **X. Wang**, **K. Choi**, **C. Lugo**, and **A. T. Hunt** (2007). Ferroelectric phase shifters at 20 and 30 GHz. *IEEE Transactions on microwave theory and techniques*, **55**(2), 430–437.

Publications based on the thesis

Refereed International Journals

1. E. S. Shajahan and M. S. Bhat (2018), “ Fabrication and characterisation of RF MEMS capacitive switches tuned for X and Ku bands”, *Int. J. Mechatronics and Automation, (Inderscience)* Vol. 6, Nos. 2/3, pp 143-149.

2. E. S. Shajahan, and M. S. Bhat (2018), “Design and Fabrication of Low Voltage Inductive Tuned RFMEMS Capacitive Switches for X and Ku bands”, *International Journal of Applied Engineering Research*, Vol. 13, No. 9, pp 6620-6627.

3. E. S. Shajahan and M. S. Bhat (2013), “Operating Analysis of DC and RF characteristics Capacitive Coupled RF MEMS Shunt Switches by Geometrical Modifications and Material selection”, *International Journal of Computer and Electrical Engineering*, Vol.5, No.5, pp 487-491.

International Conference Proceedings:

1. E. S. Shajahan and M. S. Bhat (2018), “High Isolation Single Pole Four Throw RF MEMS Switches for X band”, 8th IEEE International Symposium on Electronic System Design (ISED), December 13-15, 2018.

2. E.S.Shajahan and M.S.Bhat, “Fabrication and Characterization of RF MEMS Capacitive Switches”, Int. Conference on MEMS and Sensors (ICMEMSS 2014) IIT MADRAS, Dec.18-20, 2014.

3. E. S. Shajahan, M. S. Bhat and Chenna Reddy (2014), “Inductive Tuned High Isolation RF MEMS Capacitive Shunt Switches”, 5th IEEE International Symposium on Electronic System Design (ISED), December 15-17, 2014.

4. Chenna Reddy B, E. S. Shajahan and M. S. Bhat (2014), “Design of a Triple Band-Notched Circular Monopole Antenna for UWB Applications”, 11th IEEE International Conference on Wireless and Optical Communications Networks WOCN2014, September 11 - 13, 2014.
5. Vasudev Anand B, E. S. Shajahan and M. S. Bhat (2012), “Stub mounted loaded line phase shifter using novel RF MEMS switch”, IEEE Intl. Conference on Electron Devices and Solid State Circuits (EDSSC2012), December 3-5, 2012.
6. E. S. Shajahan and M. S. Bhat (2012), “Tuned Dual Beam Low Voltage RF MEMS Capacitive Switches for X – Band Applications”, 10th IEEE Intl. Conference on Semiconductor Electronics, Kuala Lumpur, Malaysia, September 19-21, 2012.
7. B. Vasudev Anand, E. S. Shajahan and M. S. Bhat (2013), “RF MEMS based Loaded Line Phase Shifter for X-band Applications”, 6th ISSS Conference on MEMS, Smart Materials, Structures and Systems, September 6-7, 2013.
8. Chenna Reddy B, E. S. Shajahan and M. S. Bhat (2013), “A 180-bit C-band Phase Shifter using Interdigital Low pass/High pass Filter”, 6th ISSS Conference on MEMS, Smart Materials, Structures and Systems, September 6-7, 2013.

Student Details

Name : SHAJAHAN E S
Date of Birth : 03-05-1971
Address : Green Gardens, Kalayapuram PO, Kottarakkara, Kollam
Kerala - 691560
Contact : +91-9447594170
Email : shajes2007@gmail.com
Qualification : Bachelor of Technology (B. Tech.) (1992)
Electronics & Communication Engineering
T K M College of Engineering (Govt. Aided),
University of Kerala

: Master of Technology (M.Tech.) (2003)
Digital Systems and Communication
National Institute of Technology Calicut (NITC)
Kozhikode, Kerala

: Doctor of Philosophy (Ph.D.) (2019)
National Institute of Technology Karnataka (NITK)
Surathkal, Mangalore, Karnataka